

**Studies and development of nanomaterials and polymer
nanocomposites for health, environment and industrial
applications.**

By

Nilanjali Misra

Enrolment Number: CHEM01201204005

BHABHA ATOMIC RESEARCH CENTRE

MUMBAI, INDIA



*A thesis submitted to the
Board of Studies in Chemical Sciences
In partial fulfilment of requirements*

For the Degree of

DOCTOR OF PHILOSOPHY

of

HOMI BHABHA NATIONAL INSTITUTE

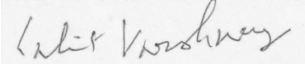
August, 2015

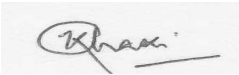
Homi Bhabha National Institute

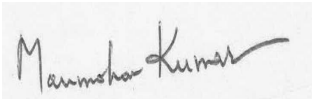
Recommendations of the Viva Voce Board

As members of the Viva Voce Board, we certify that we have read the dissertation prepared by **Nilanjal Misra** titled “**Studies and development of nanomaterials and polymer nanocomposites for health, environment and industrial applications**” and recommend that it may be accepted as fulfilling the dissertation requirement for the Degree of Doctor of Philosophy.

Chairman: **(Dr. S. Kapoor)**  Date: 07/08/2015

Guide: **(Dr. L. Varshney)**  Date: 07/08/2015

External Referee: **(Prof. T.K. Chaki)**  Date: 07/08/2015

Member 1: **(Dr. Manmohan Kumar)**  Date: 07/08/2015

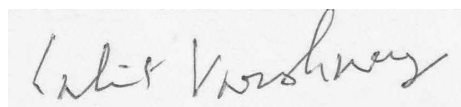
Member 2: **(Dr. Y. K. Bhardwaj)**  Date: 07/08/2015

Final approval and acceptance of this dissertation is contingent upon the candidate's submission of the final copies of the dissertation to HBNI.

I hereby certify that I have read this thesis prepared under my direction and recommend that it may be accepted as fulfilling the thesis requirement.

Date: 18/08/2015

Place: Mumbai



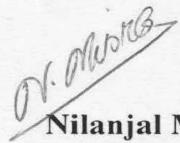
Guide

STATEMENT BY AUTHOR

This dissertation has been submitted in partial fulfillment of requirements for an advanced degree at Homi Bhabha National Institute (HBNI) and is deposited in the Library to be made available to borrowers under rules of the HBNI.

Brief quotations from this dissertation are allowable without special permission, provided that accurate acknowledgement of source is made. Requests for permission for extended quotation from or reproduction of this manuscript in whole or in part may be granted by the Competent Authority of HBNI when in his or her judgment the proposed use of the material is in the interests of scholarship. In all other instances, however, permission must be obtained from the author.

Date: 18/08/2015



Nilanjal Misra

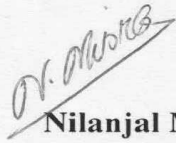
Place: Mumbai

DECLARATION

I, hereby declare that the investigations presented in the thesis have been carried out by me. The work is original and has not been submitted earlier as a whole or in part for a degree/diploma at this or any other Institution / University.

Date: 18/08/2015

Place: Mumbai



Nilanjali Misra

List of Publications arising from the thesis

Journals

1. **Nilanjali Misra**, V. Kumar, N. Goel, L. Varshney, Radiation synthesized Poly(n-vinyl-2-pyrrolidone)-stabilized-Gold nanoparticles as LSPR based optical sensor for Mercury ions estimation, *Journal of Nanoparticle Research*, 2015, 17, 1-9.
2. **Nilanjali Misra**, V. Kumar, J. Bahadur, S. Bhattacharya, S. Mazumdar, L. Borde, L. Varshney, Layered Silicate-Polymer Nanocomposite Coatings via Radiation Curing Process for Flame Retardant Applications, *Progress in Organic Coatings*, 2014, 77, 1443–1451.
3. **Nilanjali Misra**, V. Kumar, L. Borde, L. Varshney, Localized surface plasmon resonance-optical sensors based on radiolytically synthesized silver nanoparticles for estimation of uric acid, *Sensors and Actuators B*, 2013, 178, 371– 378.
4. **Nilanjali Misra**, J. Biswal, V. P. Dhamgaye, G. S. Lodha, S. Sabharwal, A comparative study of gamma, electron beam, and synchrotron X-ray irradiation method for synthesis of silver nanoparticles in PVP, *Advanced Material Letters*, 2013, 4(6), 458-463.
5. **Nilanjali Misra**, Jayashree Biswal, Alka Gupta, J. K. Sainis, S. Sabharwal, Gamma radiation induced synthesis of gold nanoparticles in aqueous polyvinyl pyrrolidone solution and its application for H₂O₂ estimation, *Radiation Physics and Chemistry*, 2012, 81, 195-200.

Conferences/Symposia

1. **Nilanjali Misra**, Virendra Kumar, Lalit Varshney, Mounika Rapolu, S. Venugopal Rao, Picosecond and Femtosecond Nonlinear Optical Studies of Silver Nanoparticles-Polymer Nanocomposites Fabricated Using Electron Beam Curing. Presented at National Laser Symposium (NLS), December 3-6, 2014, Tirupati, India.

2. **Nilanjal Misra**, Virendra Kumar, M. Joshi, Lalit Varshney, Optical limiting property of Polymer nanocomposite coatings fabricated via Electron beam curing process. Presented at Organic Devices: The Future Ahead (ODeFA), March 3-6, 2014, TSH, Mumbai
3. **Nilanjal Misra**, Virendra Kumar, Lalit Varshney, Radiation induced synthesis of Poly(n-vinyl-2-pyrrolidone) stabilized Gold nanoparticles: LSPR based estimation of Mercury ions. Presented at Asian Polymer Association (APA), February 19-21, 2014, New Delhi
4. **Nilanjal Misra**, Virendra Kumar, Manoj Joshi, Lalit Varshney, Metal nanoparticles-polymer nanocomposite coatings fabricated via Electron beam curing process: optical limiting property. Presented at Asian Workshop on Polymer Processing (AWPP), December 8-11, 2013, Goa, India.
5. **Nilanjal Misra**, V. Kumar, J. Paul, L. Varshney, Synthesis of Layered Silicate-Polymer Nanocomposite Coatings via Radiation Curing Process for Flame Retardant Applications. Presented at Advancements in Polymeric Materials (APM), March 1-3, 2013, Lucknow, India
6. **Nilanjal Misra**, V. Kumar, L. Varshney, Silver Nanoparticles Based Optical Biosensors for Estimation of Uric Acid. Presented at Interdisciplinary Symposium on Materials Chemistry (ISMC), December 11-15, 2012, Mumbai
7. **Nilanjal Misra**, Jayashree Biswal, S. Sabharwal, L. Varshney, Colorimetric Estimation of Trace Levels of Hydrogen peroxide Using Radiolytically Synthesized Gold nanoparticles. Presented at International Conference and Workshop on Nanocomposites and other Nanomaterials (ICWNCN), March 13-16, 2012, University of Delhi, New Delhi
8. **Nilanjal Misra**, Jayashree Biswal, V. P. Dhamgaye, G. S. Lodha, S. Sabharwal, Synthesis of silver nanoparticles by using synchrotron radiation from INDUS-II. Presented at ETALAN, October 20-21, 2011, Training School Hostel, BARC, Mumbai.

9. **Nilanjali Misra**, Jayashree Biswal, S. Sabharwal, Synthesis of polyvinylpyrrolidone stabilized gold nanoparticles by gamma irradiation. Presented at National symposium on radiation and photochemistry (NSRP), March 10-12, 2011, JNV Univ., Jodhpur, Rajasthan, India.



Nilanjali Misra

Dedicated to my Well wishers

ACKNOWLEDGEMENTS

I begin by expressing my sincere gratitude towards the Almighty who guided me and served as my beacon light as I ventured upon the task of compiling my work.

I humbly acknowledge the huge contribution of my mentor and guide Dr. L. Varshney, Professor, HBNI & Head, Radiation Technology Development Division, in motivating, encouraging and supporting me throughout my doctoral work. This work would not have been possible without his keen insight, foresight and his invaluable opinions, all of which contributed immensely towards uplifting the quality of the work as well as buoyed my confidence at times when I felt all at sea. His continuous efforts in the pursuit of excellence have helped me raise my bar by several notches and try and match up to his lofty expectations. I would also express my deepest sense of gratitude towards my doctoral committee Chairman Dr. S. Kapoor, and members of my doctoral committee Dr. Manmohan Kumar and Dr. Y.K. Bhardwaj for their insightful comments and constant encouragement throughout the tenure of my doctoral work and during my review meetings. Equally significant is the contribution of my friend and guide Dr. Virendra Kumar in giving shape and direction to my work. I owe my utmost gratitude to him for all the invaluable time he spent in guiding me and in actually helping me carry out my experimental work.

It is with immense gratitude that I acknowledge the help of my senior colleague Dr. Jayashree Biswal for all the support she rendered me during the initial stages of my research work. I also appreciate the support and encouragement of all the senior and fellow researchers of my division, particularly Dr. N.K. Goel and Shri. B. Dhanawade, who were always ready for any scientific and personal help throughout the period. I do thank all the non-scientific staff: Shri. S. Shejwal, Smt. Sneha, Shri. M. N. Kadu, Shri. Chauhan and Shri. Y.G. Hilati, all of whom played their parts in making this thesis possible. I also pay my

deepest gratitude to Shri Manoj Joshi, Shri. K.K. Singh, Shri. Lalit Borde from TIFR, Dr. Sahyog Jamdaar and Dr. R.K. Singhal for helping me in evaluating and characterizing the samples.

Finally, I take this opportunity to dedicate my work to all my well-wishers, foremost among them being my parents and my ever patient and supporting wife, Manjira. They have provided me with the platform to build my life upon and have always stood by me through thick and thin, thus enabling me to tide over all personal and professional trials. Without their relentless devotion and support, focusing single mindedly on my work and coming up with this thesis would have been a distant dream. Last but not the least, I thank all those whose names I might have unintentionally left out but whose contributions nevertheless have been significant in enabling the successful completion of my work.

CONTENTS

	Page No.
SYNOPSIS	XVI-XXV
LIST OF FIGURES	XXVI-XXXIV
LIST OF TABLES	XXXIV
Chapter 1: Introduction: Metal nanoparticles and polymer nanocomposites, basic principles of ionizing radiation and radiation induced synthesis	1-29
1.1 Introduction	1
1.2 Nanoparticles	
1.2.1 Basic definition and classification	2
1.2.2 Synthesis and stabilization of nanoparticles	4
1.2.3 Optical properties and applications of nanomaterials	6
1.3 Polymer nanocomposites	
1.3.1 Basic definitions and classification	9
1.3.2 Synthesis protocols	11
1.3.3 Properties and applications	13
1.4 Basic aspects of radiation chemistry	
1.4.1 Types and energy of ionizing radiation	15
1.4.2 Interaction of electromagnetic radiation with medium	16
1.4.3 Interaction of electrons with medium	19
1.4.4 Interactions of charged particles	20
1.4.5 Distribution of active species in the system – track structure	22

1.5 Radiation dosimetry: Radiation-chemical yield and Fricke Dosimeter	23
1.6 Radiation chemistry of water	
1.6.1 Primary yields	24
1.6.2 Important reducing radicals in aqueous solutions	26
1.6.3 Important oxidizing radicals in aqueous solutions	26
1.7 Synthesis of metal nanoparticles and nanocomposites by high energy radiation: advantages of radiolytic method	26
1.8 Scope of the thesis	27
Chapter 2: Experimental Methodology and characterization techniques	30-46
2.1 Introduction	30
2.2 Gamma radiation source	
2.2.1 Dosimetry of gamma chambers	31
2.3 Electron beam source	35
2.4 Synchrotron radiation source	35
2.5 Characterization Techniques	
2.5.1 UV-Visible Spectroscopy	35
2.5.2 Fourier-Transform Infra-red spectroscopy (FTIR)	36
2.5.3 Thermogravimetric Analysis (TGA)	38
2.5.4 Differential Scanning Calorimetry (DSC)	38
2.5.5 Transmission Electron Microscope (TEM)	39
2.5.6 Scanning Electron Microscope (SEM)	41
2.5.7 Atomic Force Microscope (AFM)	41

2.5.8 Particle size analyzer (PSA)	41
2.5.9 X-ray Diffraction analysis (XRD)	43
2.5.10 Zeta Potential analyzer	43
2.5.11 Nd-YAG laser system	44
2.5.12 ASTM property evaluation techniques	44
2.6 Chemical reagents	45
Chapter 3: Gamma radiolytic synthesis of Poly(n-vinyl-2-pyrrolidone) capped Au nanoparticles for sensor applications	47-70
3.1 Introduction	47
3.2 Synthesis of Au nanoparticles	
3.2.1 Formation of Au nanoparticles and their characterization	50
3.2.2 Effect of variation of Au(III) concentration	52
3.2.3 Reduction under milder condition	53
3.2.4 Role of AgNO ₃ in nanoparticle formation	54
3.2.5 Effect of variation of PVP concentration	55
3.2.6 Effect of PVP molecular weight on Au nanoparticle formation	56
3.3 Estimation of Hydrogen peroxide	
3.3.1 Detection principle	57
3.3.2 Detection limits	59
3.4 Estimation of Mercury ions	
3.4.1 Detection principle	61
3.4.2 Effect of pH	65
3.4.3 Effect of PVP concentration	66
3.4.4 Effect of PVP molecular weight	67

3.4.5 Interference study and selectivity	68
3.5 Conclusions	69
Chapter 4: A comparative study of the synthesis of Poly(n-vinyl-2-pyrrolidone) capped Ag nanoparticles by different radiation sources: application for estimation of uric acid	71-93
4.1 Introduction	71
4.2 Results and discussion	
4.2.1 Synthesis of polymer capped Ag nanoparticles by gamma, electron beam and synchrotron radiation sources and their characterization	73
4.2.2 Effect of variation of precursor ion concentration	78
4.2.3 Effect of PVP concentration	80
4.2.4 Effect of dose rate on nanoparticle formation in EB-irradiation	82
4.2.5 Estimation of uric acid	82
4.2.6 Generation of calibration curve	89
4.2.7 Estimation of uric acid in bovine and human serum samples	90
4.2.8. Effect of PVP molecular weight on sensor properties: detection principle	92
4.3 Conclusions	94
Chapter 5: Radiation induced fabrication of metal nanoparticles/inorganic fillers based polymer nanocomposite films for optical limiting and flame retardant applications	95-122
5.1 Introduction	95
5.2 Fabrication of nanocomposite films	

5.2.1 Synthesis of Ag nanoparticles/polyurethane acrylate based films	99
5.2.2 Synthesis of organophilic clay/polyurethane acrylate based films	99
5.2.3 Characterization of Ag based films	100
5.2.4 Evaluation of Optical limiting property: proposed mechanism	103
5.2.5 Characterization clay based films	106
5.2.6 Property evaluation of PCN films	115
5.3 Conclusions	122
References	123-136

SYNOPSIS

Nanomaterials are defined as materials with at least one external dimension in the size range from approximately 1-100 nanometers. Nanoparticles, in particular, are nanomaterials with all three external dimensions at the nanoscale. Two principal factors that cause the properties of nanomaterials to differ significantly from other materials and make them unique are: i) increased relative surface area, and ii) quantum effects. These factors can significantly change or enhance properties, such as reactivity, strength, optical and electrical characteristics. Hence, metal nanoparticles are currently being explored for their versatile applications as catalysts [1], chemical and bio sensors [2, 3] and drug delivery systems [4]. Noble metal nanoparticles, such as those of Gold and Silver, possess bright color in aqueous solutions [5] and are potentially useful as biosensors and for biological imaging. Spectrophotometric detection of various molecules/species, based on the optical properties of metal nanoparticles, has been widely reported [6]. Change in the spectral position, FWHM or intensity of absorption spectra of nanoparticles, due to interaction of metal nanoparticles with biological analytes, is the basis of these widely applicable and convenient colorimetric sensing techniques [7].

Metal nanoparticles, or any other fillers in the nanoscale regime, when incorporated into a polymer matrix, give rise to a new class of materials known as polymer-nanocomposites. Typically, the structure is a matrix-filler combination where the fillers like particles, fibers, or fragments surround and bind together as discrete units in the matrix. These advanced materials offer enhanced mechanical, thermal, flame retardant, barrier, electrical and chemical properties compared to their constituent elements. In recent years, nanocomposites have generated much research interest owing to remarkable enhancements in the various composite properties at very low volume fractions of nanofillers [8-10]. These polymer nanocomposite materials have found application in fields as diverse as laser safety

goggles, scratch resistant materials, aerospace, automotive sector for interior parts and under-the-hood applications, and so on.

Compared to conventional methods of fabrication, the major advantages of using high energy radiation, including electron beam and gamma irradiation, for synthesizing metal nanoparticles and nanocomposite materials, are that these are room temperature, pollution-free and high efficiency processes that can be used for rapid synthesis of uniformly dispersed metal nanoparticles [11, 12]. Similarly, in case of polymer nanocomposites, ionizing radiations have been found to impart long service life, uniform and high degree of cross-linking, and excellent thermo-mechanical properties to the materials [13, 14].

The present study is aimed at the investigation of application of ionizing radiations, viz., ^{60}Co gamma, electron beam and synchrotron radiations for fabrication of noble metal nanoparticles (Au and Ag) and novel inorganic/organic polymer nanocomposite materials. The applications of these materials in the field of sensors, optical limiters and flame retardants have also been discussed. Details of the work done and results have been reported in following five chapters.

Chapter 1: Introduction: Metal nanoparticles and polymer nanocomposites, basic principles of ionizing radiation and radiation induced synthesis

The chapter deals with fundamental aspects related to metal nanoparticles, polymer nanocomposites (PNCs) and radiation technology. These include an understanding of the basis of classification of nanoparticles and nanocomposite materials. The principles behind the stabilization of metal nanoparticles in aqueous solutions and the unique optical properties of noble metal nanoparticles, which are used in sensor applications, have been discussed. Basic aspects of radiation chemistry, such as the types and energies of ionizing radiation and

their interactions with different media have also been delved into. The radiation chemistry of aqueous solution is discussed in details, starting from the typical time scales of different radiolytic events, which finally lead to formation of primary as well as secondary radiolytic species. The chapter also deals with the conventional methods of nanoparticles and PNCs fabrication, and the advantages offered by radiation technology over these techniques. The applications of the radiation synthesized materials in the field of sensors, optical limiters and flame retardants are also mentioned.

Chapter 2: Experimental Methodology and characterization techniques

During the course of this study, a variety of methods have been employed to synthesize nanomaterials, including nanoparticles and polymer nanocomposites, and their characterizations have been carried out using numerous characterization techniques. These include steady-state irradiation facilities, such as ^{60}Co gamma chamber, Electron beam and Synchrotron irradiators for irradiation, and characterization techniques such as Transmission Electron Microscopy (TEM), Scanning Electron Microscopy (SEM), Atomic Force Microscopy (AFM), X-ray Scattering (SAXS and XRD), Fourier Transform Infrared Spectroscopy (FTIR), Thermal Analysis (TGA and DSC), UV-visible Spectroscopy, etc.. The chapter discusses the principles and methodologies involved in these studies.

Chapter 3: Gamma radiolytic synthesis of Poly(N-vinyl-2-pyrrolidone) capped Au nanoparticles for sensor applications

^{60}Co -gamma radiation was used to carry out radiolytic synthesis of Gold nanoparticles (Au-NPs) in aqueous solutions, in presence of Poly(N-vinyl-2-pyrrolidone) (PVP) as the capping and stabilizing agent. Reactive transient species generated through water radiolysis include solvated electrons (e_{aq}^-) and isopropyl radicals (generated from the reaction between

OH/H and isopropanol present in the reaction mixture), which are responsible for the reduction of the precursor Au^{3+} ions to Au atoms in the zero-valent state (Au^0). The Au^0 thus formed coalesce to form small nuclei, which grow to Au nanoparticles. The effect of variation of parameters, such as radiation dose, precursor ion concentration, stabilizer molecular weight and concentration, etc., on the particle morphology was studied. The saturation dose for complete reduction of $5.0 \times 10^{-4} \text{ mol.dm}^{-3} \text{ Au}^{3+}$ was determined spectrophotometrically to be 1.8 kGy. The reaction parameters were optimized to fabricate uniformly dispersed, spherical nanoparticles with average particle size in the range of 9-12 nm (PVP of molecular weight 360 kDa as the capping agent), as determined by TEM analysis. The Au nanoparticles thus engineered were found to exhibit typical Localized Surface Plasmon Resonance (LSPR) band at $\sim 530\text{nm}$. This optical property of the PVP-Au-NPs was exploited for employing these Au-NPs as optical biosensors.

The PVP-Au-NPs system synthesized using PVP with molecular weight 360 kDa as the capping agent was used for detection and estimation of a biologically relevant analyte hydrogen peroxide. The detection principle was based on spectrophotometrically monitoring the enzymatic reaction of H_2O_2 with o-phenylene diamine (o-PDA) in presence of enzyme Horse radish peroxidase (HRP). The reaction product has a weak absorption in the yellow region of the spectrum. Interaction of the reaction product with PVP-Au-NPs leads to an enhancement in the intensity of the LSPR absorption band of PVP-Au-NPs. The detection limit was determined to be $1.0 \times 10^{-7} \text{ mol.dm}^{-3}$ and H_2O_2 concentration could be estimated from $1.0 \times 10^{-7} \text{ mol.dm}^{-3}$ to $2.0 \times 10^{-4} \text{ mol.dm}^{-3}$ by choosing appropriate experimental parameters. Silver nanoparticles, fabricated via a similar protocol, displayed an LSPR band at $\sim 420 \text{ nm}$ which overlapped with the absorption band of the reaction product leading to interference in the detection technique. The Ag nanoparticles were, therefore, ineffective in the estimation of H_2O_2 by this method.

In another application, the same system, with some variation in the reaction parameters, was used for the detection and estimation of trace levels of Hg^{2+} ions in aqueous solutions. The detection principle was based on the preferential interaction of Hg^{2+} with PVP, a soft acid-soft base type of interaction. This leads to weakened interaction of the PVP capping agent with the Au-NPs, which gets manifested as a decrease in the LSPR band intensity of the Au-NPs. The use of low molecular weight PVP (40 kDa), as the capping agent, ensured that the Au nanoparticles were not highly stable and thereby, susceptible to changes in the external environment. This nanoparticle system was successfully used to estimate Hg^{2+} within a concentration range of 0-500nM and demonstrated high selectivity towards Hg^{2+} ions. The method was found to be independent of interference from other metal ions, such as Ca^{2+} , Cu^{2+} , Cd^{2+} and Fe^{2+} up to a concentration of 500 nM. Effect of parameters, such as pH of the medium, molecular weight and concentration of stabilizing agent on the detection efficiency were also studied in detail.

Chapter 4: A comparative study of the synthesis of Poly(N-vinyl-2-pyrrolidone) capped Ag nanoparticles by different radiation sources: application for estimation of uric acid.

In this study, Poly(N-vinyl-2-pyrrolidone) capped Ag nanoparticles (PVP-Ag-NPs) were fabricated using different radiation sources, namely ^{60}Co -gamma, electron beam and synchrotron. All three radiation sources, though ionizing in nature, vary in their energies, depths of penetration and type of interaction with materials. The λ_{max} for LSPR band of PVP-Ag-NPs was observed to be red shifted in the range of 420-430 nm with increase in Ag^+ concentration in case of X-ray and γ -irradiation method. However, λ_{max} in case of electron beam irradiation method was blue shifted within the range 420-400 nm. In all three cases, effect of the concentration of PVP and Ag^+ ions on the optical properties of PVP-Ag-NPs

was also studied. As observed from TEM analysis, the Ag nanoparticles obtained by all three methods were uniformly dispersed and spherical in nature. However, the particle sizes could be fine tuned by suitably varying the reaction parameters or by changing the radiation sources.

Ag nanoparticles synthesized via the gamma radiolytic route were used as an optical biosensor for estimation of uric acid in biological samples. The PVP-Ag-NPs were thoroughly characterized and subsequently employed as LSPR-based optical sensors for detection and estimation of uric acid concentrations in human serum and bovine serum samples. The detection principle was based on the enzymatic degradation of uric acid in presence of enzyme uricase, leading to in situ formation of H_2O_2 , which was responsible for partial oxidation/degradation of the PVP-Ag-NPs. The change was manifested as a decrease in the LSPR band intensity of the PVP-Ag-NPs. This technique was employed to successfully estimate uric acid in the concentration range of 0-50 μ M. Au nanoparticles, when employed for the same detection method, were found to display a slower response owing to their much greater noble character compared to Ag nanoparticles. Hence, the detection efficiency could be directly linked to the type of nanoparticle being utilized for the purpose.

Chapter 5: Radiation induced fabrication of metal nanoparticles/inorganic fillers based polymer nanocomposite films for optical limiting and flame retardant applications

Inorganic-Organic hybrid nanocomposite materials have received great attention from the industrial community because of their wide range of novel physico-mechanical properties. This chapter deals with the fabrication of metal nanoparticles and inorganic fillers based polymer nanocomposite films with potential optical limiting and flame retardant applications.

Nanocomposite films containing in situ generated Ag nanoparticles (Ag-NPs) dispersed in an Aliphatic urethane acrylate (AUA) matrix were synthesized using electron beam curing technique, in presence of an optimized concentration of Ag⁺ precursor ion and a diluent Trimethylolpropanetriacrylate (TMPTA). The reactive diluent not only made processing of the oligomer easier by suitably lowering its viscosity but also played the role of an effective crosslinker for AUA. The Ag-NPs-polymer nanocomposite films were thoroughly characterized by UV-visible spectroscopy, TEM and FE-SEM techniques. Both TEM and FE-SEM revealed formation of well dispersed, spherical Ag-NPs of size range 5-10 nm within the AUA-TMPTA polymer matrix. Ag-NPs doped polymer films showed an absorption peak at ~420nm whose intensity increased with increase in the Ag⁺ ion concentration. The optical limiting property of the Ag-NPs- polymer nanocomposite films was tested using a Nd-YAG Laser operated at third harmonic wavelength of 355nm. For a 25ns pulse and 10 Hz cycle, films showed good optical limiting property and the threshold fluence for optical limiting was found to be ~3.8 J/dm², for exposure duration of 10 seconds. The dynamic range was calculated to be 22.3, while transmission decreased by 82%. The presence of additional fillers, such as thiophene and modified clay cloisite 30B in addition to Ag nanoparticles, on the optical limiting characteristics was also studied.

Polymer clay nanocomposite (PCN) films were fabricated by uniformly dispersing organically modified montmorillonite clay (Cloisite 20A and Cloisite 30B) in varying concentrations of 2%, 5%, 10% and 15% (w/w), in an optimized composition of AUA-TMPTA mixture by ultra-sonication, followed by gamma radiation induced curing process. Radiation doses were optimized to obtain non-tacky, homogeneous films. The PCN films were characterized and evaluated for different properties, such as gel fraction, water uptake, solvent resistance, gloss at 60° and pendulum hardness. For PCNs with both cloisite 20A and 30B as filler, clay loadings up to 5% showed increase in gel fraction compared to the neat

polymer film, above which the gel fraction was found to decrease gradually with the increase in filler loading. Clay loading of 2% was observed to be the optimum value to achieve maximum extent of crosslinking in both cases. Gloss of the PCN films decreased while the hardness increased with increase in the clay loading in the PCN films. The flame retardant behaviour of the PCN films was evaluated in terms of their Limiting Oxygen Indices (LOI), which, in turn was determined from the % char yields of the samples determined from the thermogravimetric analyses data. The LOI values recorded were found to be higher than 21 (the threshold value for flame retardancy) for all the PCN samples, with those containing 15% of modified clay cloisite 20A and cloisite 30B showing LOI values higher than 26, suggesting their potential application as effective flame retardant materials.

Summary

Present thesis describes results from the research work carried out towards radiation engineering and characterization of polymer stabilized metal nanoparticles and polymer nanocomposite materials using ^{60}Co -gamma, Electron beam and Synchrotron radiation sources. Effect of variation of different reaction parameters on the material properties was thoroughly studied and accordingly optimized to obtain nanoparticles and polymer nanocomposites with desired properties. Radiation engineered PVP capped Au nanoparticles based optical sensors were used for detection and estimation of trace levels of hydrogen peroxide and mercury ions in aqueous solutions in micromolar and nanomolar concentrations, respectively. Similarly, a PVP-Ag nanoparticles based optical biosensor was designed for uric acid estimation in aqueous and serum samples within the concentration range of 0-50 μM . Ag nanoparticles were also generated in situ in polymer matrices via radiation curing process to develop polymer nanocomposite films with potential optical limiting applications. Radiation curing technique was also employed to fabricate organophilic clay based inorganic-

organic nanocomposite materials having good flame retardant properties. The study thus inferred that new efficient materials for targeted applications can be engineered using radiation technology; an upcoming, clean, environment friendly and high throughput technology.

References

1. R. M. Crooks, M. Zhao, L. Sun, V. Chechik, L. K. Yeung, Dendrimer-Encapsulated Metal Nanoparticles: Synthesis, Characterization, and Applications to Catalysis, 2001, *Acc. Chem. Res.* 34, 181–190.
2. J. Liu, Y. Lu, A Colorimetric Lead Biosensor Using DNAzyme-Directed Assembly of Gold Nanoparticles, 2003. *J. Am. Chem. Soc.*, 125, 6642–6643.
3. K. Kerman, M. Saito, S. Yamamura, Y. Takamura, E. Tamiya, Nanomaterial-based electrochemical biosensors for medical applications, 2008, *Trends Anal. Chem.* 27, 585-92.
4. S. D. Brown, P. Nativo, J. Smith, D. Stirling, P. R. Edwards, B. Venugopal, D. J. Flint, J. A. Plumb, D. Graham, N. J. Wheate, Gold nanoparticles for the improved anticancer drug delivery of the active component of oxaliplatin, 2010, *J. Am. Chem. Soc.* 132, 4678–84.
5. J. A. Creighton, D. G. Eadont, Ultraviolet–visible absorption spectra of the colloidal metallic elements, 1991, *J. Chem. Soc. Faraday Trans.* 87, 3881-91.
6. H. Wei, B. Li, J. Li, E. Wang, S. Dong, Simple and sensitive aptamer-based colorimetric sensing of protein using unmodified gold nanoparticle probes, 2007, *Chem. Commun.* 36, 3735–3737.
7. C. Wang, M. Luconi, A. Masi, L. Fernández, 2010, Silver nanoparticles as optical sensors, in: —Silvernanoparticles (Eds. Perez, D. P.), ISBN 978-953-307-028-5, InTech.
8. K. Yano, A. Usuki, A. Okada, Synthesis and properties of polyimide-clay hybrid films, 1997, *J. Polym. Sci., Part A: Polym. Chem.*, 35, 2289-2294.

9. M. A. Osman, V. Mittal, M. Mobridelli, U. W. Suter, Polyurethane Adhesive Nanocomposites as Gas Permeation Barrier, 2003, *Macromolecules*, 36, 9851-9858.
10. M. A. Osman, V. Mittal, M. Mobridelli, U. W. Suter, Epoxy-Layered Silicate Nanocomposites and their Gas Permeation Properties, 2004, *Macromolecules*, 37, 7250-7257.
11. S. Choi, S. Lee, Y. Hwang, K. Lee, H. Kang, Interaction between the surface of the silver nanoparticles prepared by gamma irradiation and organic molecules containing thiol group, 2003, *Rad. Phys. Chem.* 67, 517–521.
12. S. S. Gasaymeh, S. Radiman, L. Y. Heng, E. Saion, G. H. M. Saeed, Synthesis and characterization of silver/polyvinylpyrrolidone (Ag/PVP) nanoparticles using Gamma Irradiation Techniques, 2010, *Am. J. Appl. Sci.* 7, 892–901.
13. V. Kumar, Y. K. Bhardwaj, N. K. Goel, S. Francis, K. S. S. Sarma, K. A. Dubey, C. V. Chaudhari, S. Sabharwal, Coating characteristics of electron beam cured Bisphenol A diglycidyl ether diacrylate-co-aliphatic urethane diacrylate resins, 2008, *Surf. Coat. Tech.* 202, 5202–5209.
14. V. Kumar, Y. K. Bhardwaj, S. Sabharwal, Coating characteristics of electron beam cured bisphenol A diglycidyl ether diacrylate resin containing 1,6-hexanediol diacrylate on wood surface, 2006, *Prog. Org. Coat.* 55, 316-323.

S. No.	Figure Caption	P. No.
Figure 1.1	Schematic representation of nanoparticle stabilization	6
Figure 1.2	Schematic illustration of the collective oscillation of free electrons under the effect of an electromagnetic wave	8
Figure 1.3	Schematic representation of various types of interaction between filler and polymer matrix	11
Figure 1.4	Schematic representation of radiation curing technique	13
Figure 1.5	Schematic representation of mechanism of flame retardant property	14
Figure 1.6	Schematic representation of Photoelectric and Compton effects.	18
Figure 1.7	Schematic representation of interaction of electrons with medium	21
Figure 1.8	Schematic representation of distribution of active species in medium	23
Figure 2.1	Schematic diagram of a Gamma Chamber (GC-5000).	31
Figure 2.2	Schematic diagram of a Michelson Interferometer.	37
Figure 2.3	Schematic representation of TEM	40
Figure 2.4	Schematic representation of Particle Size Analyzer Laser	42
Figure 2.5	Schematic representation of ND-Yag Laser system	44
Figure 3.1	Absorption spectra of aqueous Au nanoparticle solution obtained at radiation dose (a) unirradiated reaction mixture, (b) 0.5kGy,	51

	(c) 0.9kGy, (d) 1.3kGy, (e) 1.5kGy, (f) 1.6kGy, (g) 1.8kGy	
Figure 3.2	TEM image of Au nanoparticles prepared using PVP of molecular weight 3,60,000 Da	52
Figure 3.3	Absorption spectra of aqueous Au nanoparticle solution obtained for Au ³⁺ concentration (a) 1×10 ⁻⁴ , (b) 2.5×10 ⁻⁴ , (c) 4×10 ⁻⁴ , (d) 8×10 ⁻⁴ , (e) 1×10 ⁻³ mol.dm ⁻³	53
Figure 3.4	Absorption spectra of 4×10 ⁻⁴ mol.dm ⁻³ aqueous Au nanoparticle solution (a) in presence of acetone and (b) in absence of acetone	54
Figure 3.5	Absorption spectra of aqueous Au nanoparticle solution (4×10 ⁻⁴ mol.dm ⁻³) obtained in presence of (a) 0, (b) 6×10 ⁻⁵ , (c) 1×10 ⁻⁴ , (d) 1.5×10 ⁻⁴ , (e) 2×10 ⁻⁴ , (f) 3×10 ⁻⁴ , (g) 4×10 ⁻⁴ mol.dm ⁻³ Ag ⁺ ions	55
Figure 3.6	Absorption spectra of aqueous Au nanoparticle solution obtained for PVP concentration (a) 0.1%, (b) 0.5%, (c) 1%, (d) 2%	56
Figure 3.7	Absorption spectra of aqueous Au nanoparticle solution obtained for PVP of molecular weight (M _w) (a) 40,000Da, (b) 1,60,000Da, (c) 3,60,000Da	57
Figure 3.8	Enzymatic oxidation of OPD	58
Figure 3.9	Absorption spectra of reaction medium containing OPD, HRP, H ₂ O ₂ and Au nanoparticles (in PVP, M _w = 3,60,000) in citrate buffer with varying H ₂ O ₂ concentration (higher range of H ₂ O ₂ concentration) (a) 0, (b) 2.5×10 ⁻⁶ , (c) 5×10 ⁻⁶ , (d) 1×10 ⁻⁵ , (e) 2.5×10 ⁻⁵ , (f) 5×10 ⁻⁵ , (g) 7.5×10 ⁻⁵ , (h) 1×10 ⁻⁴ , (i) 1.3×10 ⁻⁴ , (j) 1.6×10 ⁻⁴ , (k) 2×10 ⁻⁴ mol.dm ⁻³ (Inset: Linear plot of absorbance at 427nm vs H ₂ O ₂ concentration incase Au nanoparticle used was	59

in PVP of molecular weight (a) 3,60,000Da (R=0.9986), (b) 1,60,000Da (R=0.9981), (c) 40,000Da (R=0.9981): H₂O₂ concentration range= 2.5×10^{-6} to 2×10^{-4} mol.dm⁻³)

- Figure 3.10** Absorption spectra of reaction medium containing OPD, HRP, H₂O₂ and Au nanoparticles (in PVP, M_w = 3,60,000) in citrate buffer with varying H₂O₂ concentration (lower range of H₂O₂ concentration) (a) 0, (b) 1×10^{-7} , (c) 3×10^{-7} , (d) 6×10^{-7} , (e) 1.2×10^{-6} , (f) 1.8×10^{-6} , (g) 2.5×10^{-6} , (h) 3×10^{-6} , (i) 5×10^{-6} mol.dm⁻³ (Inset: Linear plot of absorbance at 427nm vs H₂O₂ concentration incase Au nanoparticle used was in PVP of M_w = 3,60,000 Da(R=0.9954): H₂O₂ concentration range= 1×10^{-7} to 3×10^{-6} mol.dm⁻³) 60
- Figure 3.11** TEM images of PVP-Au-NPs in (a) absence of Hg²⁺ ions (b) immediately after addition of 500nM Hg²⁺ (c) 5 minutes after addition of Hg²⁺ 63
- Figure 3.12** Particle size analysis of Au nps in (a) absence of Hg²⁺ ions and (b) immediately after addition of 500nM Hg²⁺ 64
- Figure 3.13** Absorption spectra of Au nanoparticle solution in presence of (a) 0 (b) 100 (c) 200 (d) 300 (e) 400 and (f) 500nM Hg²⁺ ion. (Inset: Calibration plot of Hg²⁺ ion concentration.) 65
- Figure 3.14** Absorption spectra of Au nps-500nM Hg²⁺ reaction mixture at pH (a) 3.0 (b) 6.0 (c) 8.0 (d) 10.0 and (e) 11.0 66
- Figure 3.15** Relative change (%) in OD of reaction mixture containing PVP-Au-NPs and 500nM Hg²⁺ ions as a function of PVP % (w/v) 68

(Inset: Relative change (%) in OD of reaction mixture containing PVP-Au-NPs and 500nM Hg^{2+} ions as a function of PVP molecular weight).

- Figure 3.16** Interference study: Absorption spectra of Au nps in (a) absence of metal ions (b) 500nM Ca^{2+} (c) 500nM Cu^{2+} (d) 500nM Fe^{2+} (e) 500nM Cd^{2+} and (f) mixture of ions (500nM each) 69
- Figure 4.1** Absorption spectra of aqueous Ag nanoparticles in PVP prepared by X-ray irradiation for different irradiation time: (a) 12s, (b) 23sec, (c) 41s, (d) 63s; $[\text{Ag}^+] = 2 \times 10^{-4} \text{ mol.dm}^{-3}$, $[\text{PVP}] = 0.5\%$, $[\text{Isopropanol}] = 2 \times 10^{-1} \text{ mol.dm}^{-3}$, dose rate = 113.7 kGy.h^{-1} . 76
- Figure 4.2** TEM image of Ag nanoparticles in PVP prepared by X-ray irradiation 76
- Figure 4.3** Absorption spectra of aqueous Ag nanoparticles in PVP prepared by γ -irradiation for different absorption dose: (a) 1kGy, (b) 1.3kGy, (c) 1.6kGy; $[\text{Ag}^+] = 2 \times 10^{-4} \text{ mol.dm}^{-3}$, $[\text{PVP}] = 0.5\%$, $[\text{Isopropanol}] = 2 \times 10^{-1} \text{ mol.dm}^{-3}$, dose rate = 4.0 kGy.h^{-1} 77
- Figure 4.4** TEM image of Ag nanoparticles in PVP prepared by γ -irradiation 77
- Figure 4.5** Absorption spectra of aqueous Ag nanoparticles in PVP prepared by X-ray irradiation for different Ag^+ concentration: (a) $1 \times 10^{-4} \text{ mol.dm}^{-3}$, (b) $2 \times 10^{-4} \text{ mol.dm}^{-3}$, (c) $3 \times 10^{-4} \text{ mol.dm}^{-3}$, (d) $4 \times 10^{-4} \text{ mol.dm}^{-3}$; dose = 1.0kGy, 2.0kGy, 3.0kGy, 4.0kGy respectively; $[\text{PVP}] = 0.5\%$, $[\text{Isopropanol}] = 2 \times 10^{-1} \text{ mol.dm}^{-3}$, dose rate = 113.7 kGy.h^{-1} 78

- Figure 4.6** Absorption spectra of aqueous Ag nanoparticles in PVP 79
 prepared by γ -irradiation for different Ag^+ concentration: (a) $1 \times 10^{-4} \text{ mol.dm}^{-3}$, (b) $2 \times 10^{-4} \text{ mol.dm}^{-3}$, (c) $3 \times 10^{-4} \text{ mol.dm}^{-3}$, (d) $4 \times 10^{-4} \text{ mol.dm}^{-3}$; dose=1.0kGy, 2.0kGy, 3.0kGy, 4.0kGy respectively; [PVP]= 0.5%, [Isopropanol]= $2 \times 10^{-1} \text{ mol.dm}^{-3}$, dose rate= 4.0 kGy.h^{-1}
- Figure 4.7** Absorption spectra of aqueous Ag nanoparticles in PVP 79
 prepared by EB- irradiation for different Ag^+ concentration: (a) $1 \times 10^{-4} \text{ mol.dm}^{-3}$, (b) $2 \times 10^{-4} \text{ mol.dm}^{-3}$, (c) $3 \times 10^{-4} \text{ mol.dm}^{-3}$, (d) $4 \times 10^{-4} \text{ mol.dm}^{-3}$; dose=1.0kGy, 2.0kGy, 3.0kGy, 4.0kGy respectively; [PVP]= 0.5%, [Isopropanol]= $2 \times 10^{-1} \text{ mol.dm}^{-3}$, dose rate= 2.0 kGy/pass
- Figure 4.8** Absorption spectra of aqueous Ag nanoparticles in PVP 80
 prepared by X-ray irradiation for different PVP concentration: (a) 0.1%, (b) 0.5%, (c) 1%, (d) 2% (w/v); [Ag^+]= $2 \times 10^{-4} \text{ mol.dm}^{-3}$, [Isopropanol]= $2 \times 10^{-1} \text{ mol.dm}^{-3}$, dose=2.0kGy, dose rate= 113.7 kGy.h^{-1}
- Figure 4.9** Absorption spectra of aqueous Ag nanoparticles in PVP 81
 prepared by γ -irradiation for different PVP concentration: (a) 0.1%, (b) 0.5%, (c) 1%, (d) 2% (w/v); [Ag^+]= $2 \times 10^{-4} \text{ mol.dm}^{-3}$, [Isopropanol]= $2 \times 10^{-1} \text{ mol.dm}^{-3}$, dose=2.0kGy, dose rate= 4.0 kGy.h^{-1}
- Figure 4.10** Absorption spectra of aqueous Ag nanoparticles in PVP 81
 prepared by EB-irradiation for different PVP concentration: (a) 0.1%, (b) 0.5%, (c) 1%, (d) 2% (w/v); [Ag^+]= $2 \times 10^{-4} \text{ mol.dm}^{-3}$,

[Isopropanol]= 2×10^{-1} mol.dm⁻³, dose=2.0kGy, dose rate= 2.0kGy/pass

- Figure 4.11** Absorption spectra of aqueous Ag nanoparticles in PVP prepared by EB-irradiation for different absorption dose rates: (a) 2.0kGy/pass, (b) 1.0kGy/pass; [Ag⁺]= 2×10^{-4} mol.dm⁻³, [PVP]= 0.5%, [Isopropanol]= 2×10^{-1} mol.dm⁻³ 82
- Figure 4.12** Enzymatic degradation of uric acid in presence of Uricase. 83
- Figure 4.13** Absorption spectra of 150 μM Ag nanoparticle solution in presence of 50μM uric acid after (a) 0 min, (b) 5 min, (c) 20 min, (d) 45 min, (e) 60 min. Inset: absorbance strength of Ag nanoparticles solution containing uric acid as a function of time. 84
- Figure 4.14** Absorption spectra of uric acid solution in presence of Uricase after (a) 0 min, (b) 5 min, (c) 10 min, (d) 15 min, (e) 20 min 85
- Figure 4.15** Absorption spectra of Ag nanoparticle solution (PVP, Mol wt.= 40kD) in presence of different concentration of uric acid, after 60 min: (a) 0 μM, (b) 10 μM, (c) 20 μM, (d) 30 μM, (e) 40 μM, (f) 50 μM. Inset: Linear plot of absorbance of Ag nanoparticle vs uric acid concentration ($R^2=0.9964$), uric acid concentration range= 0 to 5×10^{-5} mol.dm⁻³. 86
- Figure 4.16** TEM micrograph of Ag nanoparticles prepared using PVP of molecular weight 40kD (a) before addition of uric acid (b) after addition of uric acid 87
- Figure 4.17** AFM images of Ag nanoparticles prepared using PVP (Mol wt.= 40kD) (a) before addition of uric acid (b) after addition of uric 88

	acid	
Figure 4.18	Zeta potential of Ag nanoparticle as a function of uric acid. Inset: Zeta potential curve for Ag nanoparticle solution without uric acid.	89
Figure 4.19	Absorption spectra of Ag nanoparticle solution (PVP, Mol wt.= 160kD) in presence of different concentration of uric acid, after 60 min: (a) 0 μM , (b) 10 μM , (c) 20 μM , (d) 30 μM , (e) 40 μM , (f) 50 μM . Inset: Linear plot of absorbance of Ag nanoparticle vs uric acid concentration ($R^2=0.8826$), uric acid concentration range= 0 to 5×10^{-5} mol.dm ⁻³ .	93
Figure 4.20	Absorption spectra of Ag nanoparticle solution (PVP, Mol wt.= 160kD) in presence of different concentration of uric acid, after 8 hrs: (a) 0 μM , (b) 10 μM , (c) 20 μM , (d) 30 μM , (e) 40 μM , (f) 50 μM . Inset: Linear plot of absorbance of Ag nanoparticle vs uric acid concentration ($R^2=0.9679$), uric acid concentration range= 0 to 5×10^{-5} mol.dm ⁻³ .	93
Figure 5.1	Chemical structure of (a) Oligomer-Aliphatic urethane acrylate (AUA) (b) Reactive diluent-Trimethylolpropanetriacrylate (TMPTA) (c) Organic modifier for Cloisite 20A (where HT: hydrogenated Tallow) and (d) Organic modifier for Cloisite 30B (where T: Tallow)	100
Figure 5.2	UV-Vis spectra of PNCs containing(a) 8mM (b) 16mM and (c) 30mM Ag NPs as fillers	101
Figure 5.3	TEM image of Ag NPs embedded in AUA-TMPTA PNC film	102

Figure 5.4	FE-SEM image of Ag NPs embedded in AUA-TMPTA PNC film	102
Figure 5.5	Plot of output fluence as a function of input fluence for 10 sec exposure duration	104
Figure 5.6	Variation of optical limiting property with exposure duration [(a) 1 sec vs (b) 1sec exposure duration]	105
Figure 5.7	Optical Limiting property of (a) control film and films with (b) Ag NPs (c) Thiophene/Ag NPs and (d) Cloisite 30B/Ag NPs as nanofillers	106
Figure 5.8	UV-visible transmittance spectra of PCN films containing Cloisite 20A as nanofiller (a) 0% (b) 2% (c) 5% (d) 10%.	107
Figure 5.9	FTIR spectra of PCN films (a) without nanoclay, (b) with 10% nanoclay (cloisite 20A)	108
Figure 5.10	X-ray diffraction patterns of (a) nanoclay powder-Cloisite 20A and PCNs containing 2% and 5% Cloisite 20A, (b) nanoclay powder-Cloisite 30B and PCNs containing 2% and 5% Cloisite 30B.	110
Figure 5.11	(a) SAXS diffraction patterns of PCNs containing 5% Cloisite 20A at temperatures (i) 25°C, (ii) 150°C and (iii) 200°C and (b) In-situ isothermal scattering data at 150°C as a function of time.	110
Figure 5.12	TEM images of PCN films containing 2% nanoclay (a) Cloisite 20A and (b) Cloisite 30B	111
Figure 5.13	SEM images of PCN films containing Cloisite 20A nanoclay (a) 0% (b) 2% (c) 5% (d) 10% and (e) 15%	113
Figure 5.14	DSC profiles of PCN films (a) without nanoclay (b) with 5%	115

Cloisite 20A and (c) 5% Cloisite 30B

Figure 5.15 Pendulum hardness analysis of PCN films with different loadings of nanoclay (a) Cloisite 20A, (b) Cloisite 30B. (Inset: Gloss at 60° data for PCNs with different loadings of Cloisite 20A). 117

Figure 5.16 TGA analysis of PCN films containing (a) 0% filler (b) 2% Cloisite 20A (c) 5% Cloisite 20A (d) 2% Cloisite 30B and (e) 5% Cloisite 30B. (Inset: Differential Thermogravimetric plots for PCN films containing (a) 0% filler (b) 2% Cloisite 20A (c) 5% Cloisite 20A (d) 2% Cloisite 30B and (e) 5% Cloisite 30B.) 121

S. No.	Table Caption	P. No.
4.1	Determination of uric acid in human serum samples using proposed method and comparison method; results of one sample T-test and one way ANOVA F-test.	91
5.1	Water uptake (%), weight loss (%) in Acetone and Gel fraction of PCNs with different filler loadings	119
5.2	Limiting Oxygen Indices (LOI) of PCNs with different filler loadings	121

Chapter 1: Introduction to metal nanoparticles and polymer nanocomposites: principle of radiation induced synthesis

1.1. Introduction

"**There's Plenty of Room at the Bottom**", the historic remark Richard Feynman made during his lecture delivered on December 29, 1959, is what probably sowed the seeds for the emergence and growth of the concept of nanotechnology. Though not entirely unknown to the ancient and medieval world, the concept of nanotechnology gathered steam primarily during the 1980's as seminal work and discoveries by researchers from across the globe converged to build up a strong platform on which the future course of this field was to be based. Fundamental works in the field was soon followed by the myriad of applications which further augmented people's interest in this area and led to growing public awareness. The past decade or so has been witness to massive developments in this field and with every passing year, there has been a phenomenal growth in areas such as basic research, applications in the field of catalysis, sensors, imaging and other applications as well as in disciplines such as quantum dots, polymer nanocomposites, drug delivery systems etc. [1-10]

Nanomaterials are traditionally defined as materials with at least one external dimension in the size range from approximately 1-100 nanometers. These materials owe their uniqueness to their distinct differences from the corresponding bulk materials. The primary characteristics that describe a nanomaterial are i) increased specific surface area, and ii) quantum effects [11,12] These factors can significantly change or enhance properties, such as reactivity, strength, optical and electrical characteristics. As a particle decreases in size, a greater proportion of atoms are found at the surface compared to those inside. Thus nanomaterials have a much greater surface area per unit mass compared to larger particles

[13-16]. As growth and catalytic chemical reactions occur at surfaces, this means that a given mass of material in nanoparticulate form will be much more reactive than the same mass of material made up of larger particles. In tandem with surface-area effects, quantum effects can begin to dominate the properties of matter as size is reduced to the nanoscale [14]. These can affect the optical, electrical and magnetic behaviour of materials, particularly as the structure or particle size approaches the smaller end of the nanoscale. Materials that exploit these effects include quantum dots, and quantum well lasers for optoelectronics.

Another area that has generated tremendous interest over the years is nanocomposite materials, which basically combines the properties of a nanomaterial with those of a suitable matrix in which it is uniformly dispersed. Polymer nanocomposites ie, materials with a polymeric matrix, in particular have emerged as a highly useful class of materials [17,18]. These advanced materials offer enhanced mechanical, thermal, flame retardant, barrier, electrical and chemical properties compared to their constituent elements, which arise due to nanoscale level of mixing between the fillers and the base polymer matrix.

The growth of nanotechnology has simultaneously led to the emergence of a large number of fabrication techniques. One of the important techniques of nanosynthesis involves the use of ionizing radiation sources, such as UV, gamma, electron beam and X-rays. This technique has also shown remarkable growth over the years and has been extensively employed in the current research work.

1.2. Nanoparticles

1.2.1. Basic definition and classification

Nanoparticles are defined as nanomaterials which have all three dimensions in the nano regime i.e. within the 1-100nm range. These include colloids and quantum dots (tiny particles of semiconductor materials). Nanoparticles that are naturally occurring (e.g.,

volcanic ash, soot from forest fires) or are the incidental byproducts of combustion processes (e.g., welding, diesel engines) are usually physically and chemically heterogeneous systems and often termed ultrafine particles. Nanoparticles can be classified into five categories:

(i) Fullerenes and Carbon Nanotubes: These are crystalline forms of carbon and constitute 28 to more than 100 atoms, forming a hollow sphere. Fullerenes and carbon nanotubes (CNTs) are similar as both can be bonded with organic or inorganic groups to form various products. They find application in Solar and lithium batteries, Electronics, Storage of gases, such as methane and oxygen, Additives to rubber and plastics, treatment of various diseases, including AIDS and cancer, polymer composite, for hydrogen storage and in batteries etc. [19]

(ii) Metals: These include noble metal nanoparticles such as those of Gold, Silver and Palladium. These particles have a wide variety of applications and are extensively used in Catalysis, Electronics, Sensing, Photonics, Environmental cleanup, Imaging, Drug delivery etc

(iii) Ceramics: Ceramic are objects created from inorganic, non-metallic materials. A wide range of industries use ceramic materials, including Mining, Aerospace, Medicine, Refinery, Food and chemical industries, Packaging science, Electronics, Industrial and transmission electricity, Guided light wave transmission [20-22]

(iv) Semiconductors (Quantum dots): Quantum dots are combinations of chemical elements from Groups II and IV or Groups III and V of the periodic table. Sizes range from about 1 to 10 nm in diameter and display unique optical and electronic properties. Quantum dots may be used in semiconductors, insulators, metals, magnetic materials or metal oxides. Medical field uses include imaging, high-speed and high-resolution screening, drug vectors, diagnostic tools, solar batteries etc [23-26]

(v) **Polymeric:** Polymeric nanoparticles include dendrimers and these have potential applications as drug delivery devices, gene therapy and delivery of proteins, peptides and genes through oral route administration, imaging agents, affinity ligands etc [27-28].

1.2.2. Synthesis and stabilization of nanoparticles

The various methods of nanoparticle synthesis are broadly classified under two categories: (a) Top down approach and (b) Bottom up approach. The top down approach involves breaking down of a bulk system into its compositional sub units in the nanoscale regime. Examples of this kind of approach include the various types of lithographic techniques (such as photo-, ion beam-, electron- or X-ray- lithography) cutting, etching and grinding. The bottom up approach, on the other hand, refers to the buildup of a material from the bottom i.e. from smaller units like atoms to bigger units such as nanoclusters. A number of bottom-up approaches have been developed for producing nanoparticles, ranging from condensation of atomic vapours on surfaces to coalescence of atoms in liquids. All types of chemical synthesis, self-assembly and molecular fabrication also fall under the ambit of bottom-up approach [29-31].

Nanoparticles, owing to their extraordinarily large surface areas, are thermodynamically unstable particles and their general tendency is to coalesce and thereby minimize the surface energy to form thermodynamically stable bulk particles. Although any reducing agent, with a suitable redox potential, can ideally reduce a bulk metal to its corresponding nano form, the basic challenge of nanosynthesis lies in the stabilization of the nanoparticles formed so as to retain their unique properties. In the absence of any counteractive repulsive forces, the van der Waals forces between two metal nanoparticles would lead to aggregation. The two most common approaches adopted for nanoparticle stabilization during their fabrication are (i) Steric stabilization and (ii) Electrostatic

stabilization [32,33]. The steric stabilization approach makes use of a capping agent such as a polymer [34,35], surfactant [36], solid support [37] or a ligand [38] having suitable functional groups. These capping agents can get adsorbed onto the colloidal particles and encapsulate them to prevent their agglomeration. This mode of approach is not affected by the salt concentration in the media. These additives cover the system in such a way that long loops and tails extend out into solution. The effectiveness of steric stabilizers can be attributed to the thermodynamic penalty when one tries to confine polymeric chains to smaller volumes. Another explanation is that the hydrophilic nature of the free end of the polymeric chains ensures that they stay associated with water, rather than interact with any other surface and induce coalescence. On the other hand, electrostatic stabilization is a kinetics driven process where the attractive van der Waals forces are counterbalanced by repulsive Coulombic forces acting between the negatively charged colloidal particles. This is realized through the adsorption of negatively charged ions onto the metal nanoparticles surface, which results in the formation of an electrical double layer around the particles [fig. 1.1]. The whole process is explained by the DLVO theory [39]. The theory, in a nutshell, explains the aggregation of aqueous dispersions quantitatively and describes the force between charged surfaces interacting through a liquid medium. It combines the effects of the van der Waals attraction and the electrostatic repulsion due to the double layer of counterions. The theory expresses the overall interaction between two particles or two surfaces in a liquid by the following equation [eqn. 1.1]

$$W(D) = W(D)_A + W(D)_R \quad 1.1.$$

Where W is the net free energy per unit area, $W(D)_R$ is the repulsive interaction energy due to electric repulsion and $W(D)_A$ is the attractive interaction energy due to van der Waals interaction. The above relation holds good at smaller separations for smooth

substrates. However, at larger distances the interaction decays more quickly due to retardation effects, while surface roughness may reduce this interaction at smaller distances.

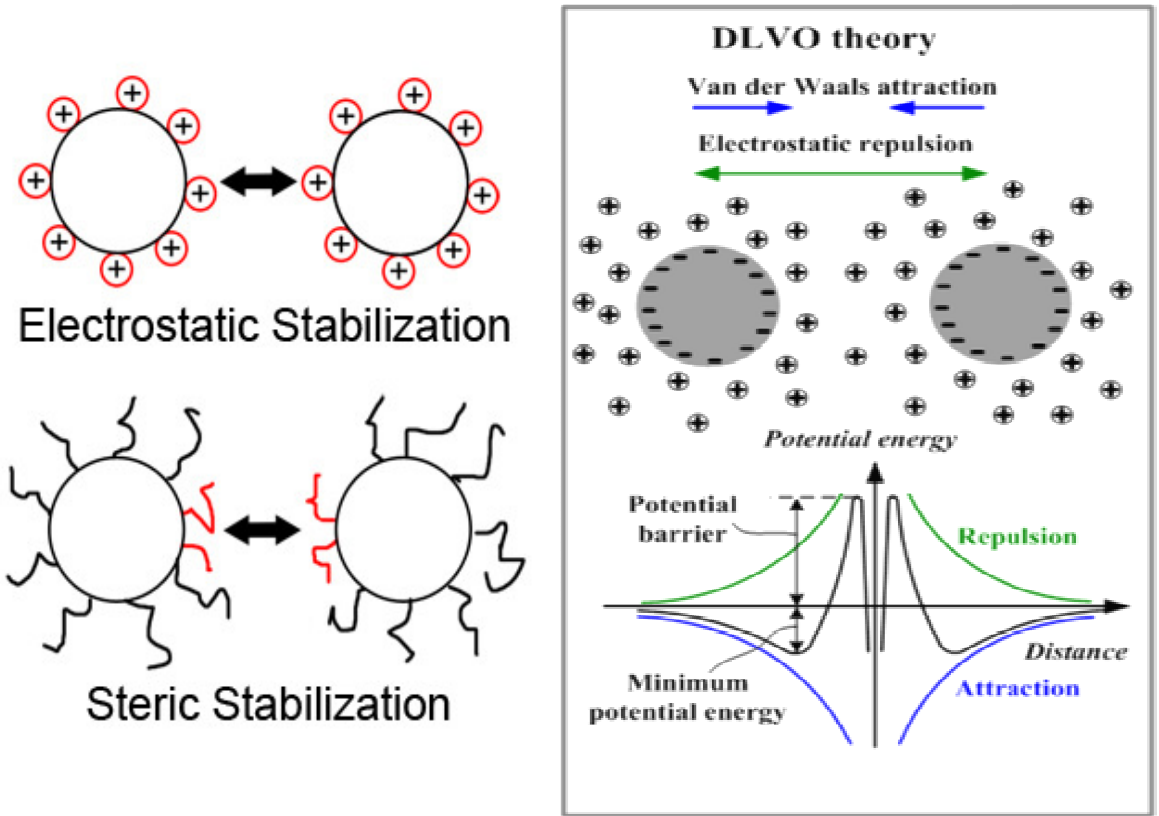


Fig. 1.1 Schematic representation of nanoparticle stabilization

1.2.3. Optical properties and applications of nanomaterials

The primary importance of nanoparticles lies in their unique optical, chemical, physical and mechanical properties, which can be exploited for a variety of applications. Optical properties, in particular, have been extensively used in the field of optical sensors. Noble metal nanoparticles, such as those of gold and silver, display distinct Localized Surface Plasmon Resonance (LSPR) bands with high extinction coefficients in the visible

region. These have therefore been the basis for the development of a large number of nanoparticles based spectrophotometric estimation techniques.

Localized surface plasmon resonance (LSPR) is an optical phenomena generated by light when it interacts with conductive nanoparticles (NPs) that are smaller than the incident wavelength. As in surface plasmon resonance, the electric field of incident light can be deposited to collectively excite electrons of a conduction band, with the result being coherent localized plasmon oscillations with a resonant frequency that strongly depends on the composition, size, geometry, dielectric environment and separation distance of NPs [40]. The electric field of the incoming light wave induces a polarization of the conduction electrons with respect to the much heavier ionic core of a metal nanoparticle. A net charge difference is felt at the nanoparticle boundaries (surface), which in turn acts as the restoring force that generates periodic dipolar oscillations of the electrons [fig 1.2]. In case of gold and silver nanoparticles, these absorptions can be easily monitored using UV-visible spectroscopy.

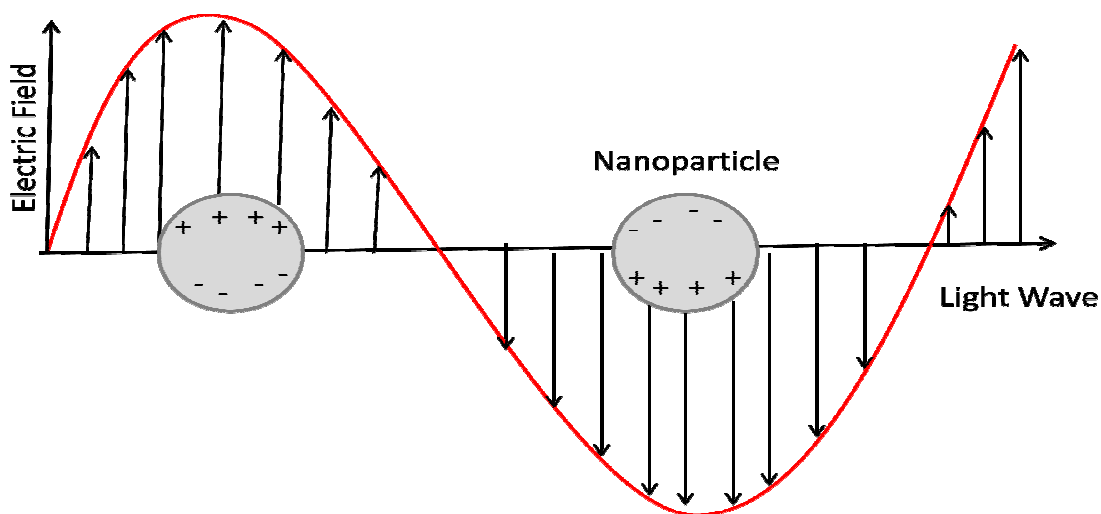


Fig. 1.2 Schematic illustration of the collective oscillation of free electrons under the effect of an electromagnetic wave

In case of dilute solutions of spherical metal nanoparticles, the factors governing the resonance conditions can be explained on the basis of the Mie solution to Maxwell's equations, also termed as the Mie theory [41-43]. The theory, developed by Gustav Mie in 1908, explains electromagnetic scattering by a homogeneous, isotropic sphere. The main assumption of Mie's theory of the optical absorption by small particles is that the particle and its surrounding medium are each homogeneous and describable by their bulk optical dielectric functions. By solving the Maxwell's equation for an electromagnetic light wave interacting with small spheres, under appropriate approximations, Mie calculated the scattering and extinction cross sections with multiple oscillations for spherical particles. However, for nanoparticles much smaller than the wavelength of light ($2r < \lambda$, or roughly $2r < \lambda_{\text{max}}/10$) only the dipole oscillation contributes significantly to the extinction cross-section [44-46]. The Mie theory then reduces to the following relationship (dipole approximation):

$$\sigma_{\text{ext}}(\omega) = 9 \frac{\omega}{c} \epsilon_m^{3/3} V \frac{\epsilon_2(\omega)}{[\epsilon_1(\omega) + 2\epsilon_m]^2} \quad 1.2$$

Where, where σ_{ext} is the extinction coefficient, V is the particle volume, ω is the angular frequency of the exciting light, c is the speed of light, and ϵ_m and $\epsilon(\omega) = \epsilon_1(\omega) + i\epsilon_2(\omega)$ are the dielectric functions of the surrounding medium and the material itself respectively. While the first is assumed to be frequency independent, the latter is complex and is a function of energy.

The exploitation of the optical properties of metal nanoparticles, particularly noble metal nanoparticles, is not only confined to their LSPR based applications but also include applications based on other optical properties such as Fluorescence, Light Scattering and Surface Enhanced Raman Spectroscopy (SERS). LSPR properties have been utilized to develop highly sensitive techniques for estimation of trace levels of biologically and environmentally relevant molecules. Several papers have been published which highlight the

application of gold nanoparticles for colorimetric estimation of DNA, proteins, pesticides, metal ions such as Mercury, Lead etc, biologically relevant molecules such as Hydrogen peroxide, dopamine etc [47-51]. Triangular shaped silver nanoparticles have been demonstrated by Haes et al to have high sensitivity towards large proteins and antibodies [52]. LSPR based absorption property has also been used in Plasmonic Photothermal Therapy for selective elimination of cancer cells [53]. Similarly, light scattering properties of gold nanoparticles have been employed by Sokolov et al for cellular imaging of cancer cells [54]. For highly scattering tissues, fluorescence based imaging techniques have been developed which provide greater sensitivity compared to scattering based techniques [55, 56]. Colloidal gold nanoparticles have also been extensively used as SERS substrates to probe components in living cells, especially to study the interaction of various antitumor drugs with their pharmacological targets [57-59].

1.3. Polymer nanocomposites

1.3.1. Basic definitions and classification

Composites, in general, are defined as materials comprising of two or more constituent materials with significantly different physical or chemical properties, which when combined, produce a material with properties different from or superior to those of the individual components. Polymer nanocomposites, in particular, are composite materials in which nanoscopic inorganic particles, with atleast one dimension in the nanoscale regime, are dispersed in a polymeric matrix in order to dramatically alter or improve the properties of the polymer. In the last 20 years, there has been a strong emphasis on the development of such polymeric nanocomposites, where at least one of the dimensions of the filler material is of the order of a nanometer. These are high performance materials that exhibit unusual property combinations and unique design possibilities. In general, nanomaterials provide reinforcing

efficiency because of their high aspect ratios [60]. The properties of a nanocomposite largely depend on the size of the filler phases and the degree of mixing between the two phases. The nature of the components used (layered silicate or nanofiber, cation exchange capacity, and polymer matrix) and the method of preparation can be tuned as per requirement to achieve significant differences in composite properties [61]. Similarly, in the case of fibrous or particle-reinforced polymer nanocomposites (PNCs), dispersion of the nanoparticle and adhesion at the particle–matrix interface are the deciding factors in determining the mechanical properties of the nanocomposite. A poor dispersion of the nanofiller can in fact lead to deterioration of the mechanical properties [62]. Additionally, the interfacial bond between the particle and the matrix can be accordingly optimized to tailor the properties of the overall composite. For instance, good adhesion at the interface will improve properties such as interlaminar shear strength, delamination resistance, fatigue, and corrosion resistance [12]. Conventional polymer matrices used include polyurethanes, aliphatic and aromatic urethane acrylates, LDPE, nylon, Poly ethylene terephthalate (PET) etc., whereas the most commonly used fillers, besides metal nanoparticles, are nanoclays (montmorillonites), nanosilica, CNTs, graphene etc.

Based on the type of nanofiller used, polymer nanocomposites can be classified as materials containing nanofillers in the form of:

- (i) particles (e.g. minerals, metal nanoparticles)
- (ii) sheets (e.g. exfoliated clay stacks)
- (iii) fibres (e.g. carbon nanotubes or electrospun fibres) [63-65].

Polymer nanocomposites containing modified organophilic clay (lamellar nanocomposites) can be further sub categorized based on the extent of mixing of clay layers with the polymer chains:

(i) **Phase separated:** These are materials where the nanofillers are not uniformly dispersed throughout the polymer matrix.

(ii) **Intercalated:** In this category, the polymer chains alternate with the inorganic layers in a fixed compositional ratio and have a well defined number of polymer layers in the intralamellar space.

(iii) **Exfoliated:** In exfoliated nanocomposites, the number of polymer chains between the layers is almost continuously variable and the layers stand $>100 \text{ \AA}$ apart.

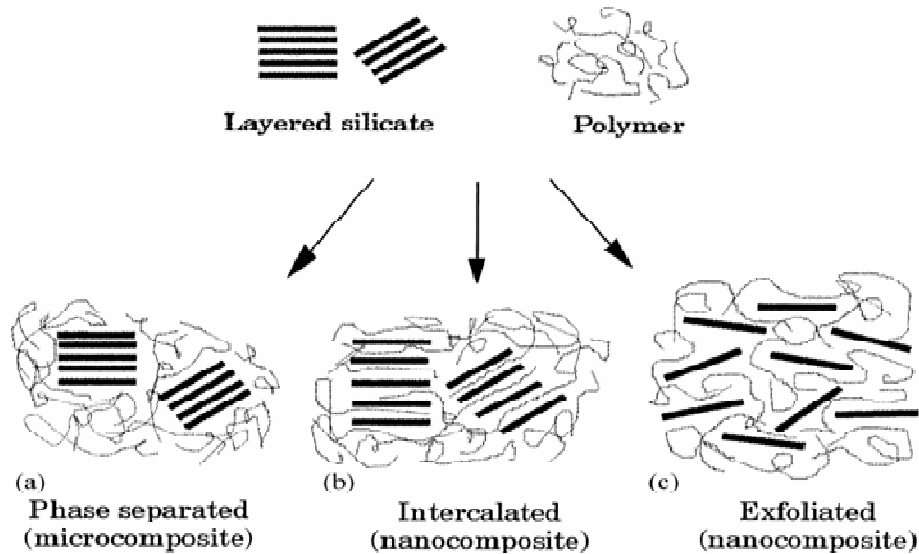


Fig. 1.3 Schematic representation of various types of interaction between filler and polymer matrix

1.3.2. Synthesis protocols

The three basic methods of polymer nanocomposite fabrication are:

(i) Solution casting (ii) Melt blending and (iii) In-situ polymerization. In solvent casting, the polymer and the nanofiller are dispersed in a suitable common solvent and thoroughly mixed by ultrasonication. The solvent is subsequently allowed to evaporate to leave behind a thin film of the polymer nanocomposite. In the case of melt blending, an extruder or an internal

mixer is used. The polymer and the nanofiller are added in the extruder and subjected to intensive mixing till a uniform, homogeneous matrix is obtained. The insitu polymerization method involves mixing of the nanoreinforcement with the monomeric or oligomeric precursor of the polymer. Once uniform dispersion is achieved, the polymerization is carried out by using a suitable agent such as a catalyst, a radical initiator or by using high energy radiation sources such as gamma and Electron beam.

Besides these conventional techniques, some of the other widely used methods for manufacturing composite parts are wet lay-up, pultrusion, resin transfer molding (RTM), vacuum assisted resin transfer molding (VARTM), autoclave processing, resin film infusion (RFI), prepreg method, filament winding, fiber placement technology, etc [66]. However, all these methods suffer from certain limitations that restrict their utility as commercially viable techniques for mass production of radiation cured products. Therefore, of late, radiation curing technique, in particular Electron beam curing, has emerged as the front runner for large scale production of economical, high quality radiation cured materials.

Radiation curing of a polymeric material involves the use of radiation to generate radicals, which subsequently result in crosslinking to generate a polymeric matrix of inter connected polymeric chains. A typical radiation curable formulation comprises of (a) a multifunctional monomer or oligomer such as urethane acrylates, (b) reactive diluents to optimize the viscosity and to serve as a crosslinking agent and (c) nanofiller. The components are chosen as per the desired properties. The thoroughly homogenized reaction mixtures are exposed to a radiation source till the formulation converts into a non-tacky, uniformly crosslinked, cured matrix, with the polymer chains held together by the multifunctional reactive diluent molecules acting as crosslinkers.

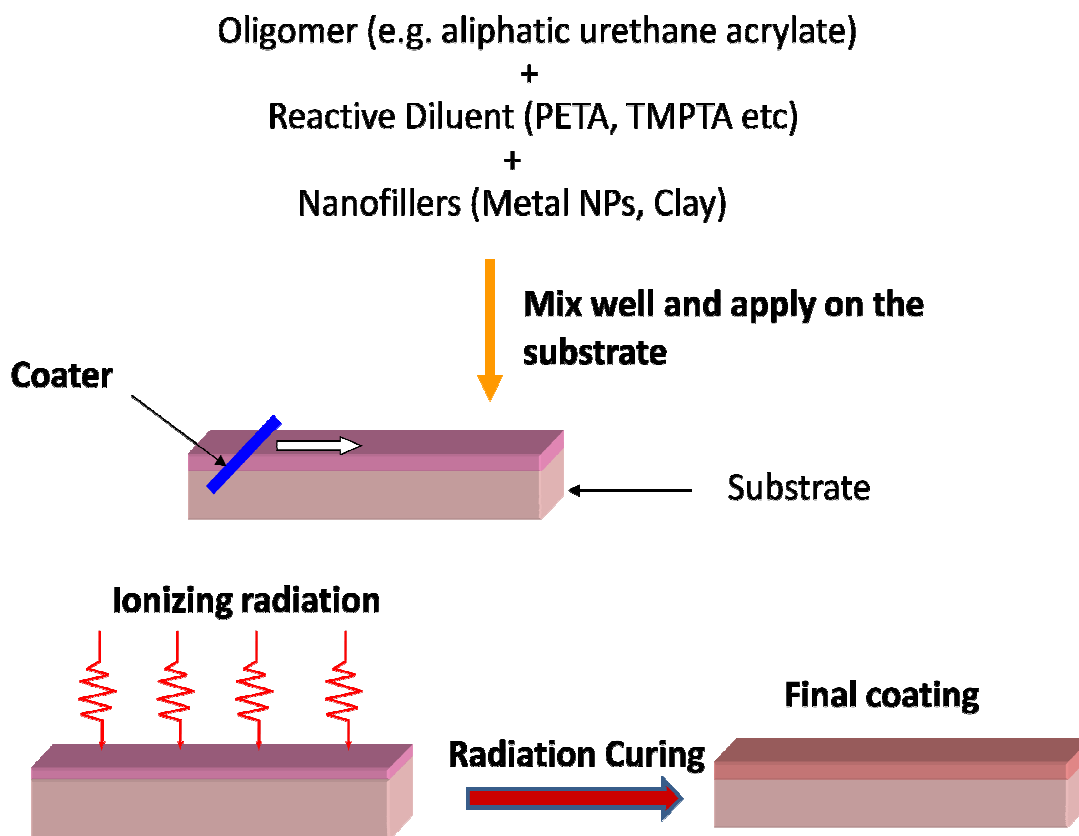


Fig. 1.4 Schematic representation of radiation curing technique

1.3.3 Properties and applications

The unique properties of polymer nanocomposites find application in a vast array of fields. Polymer nanocomposite materials possess enhanced thermal, mechanical, optical and electrical properties which are exploited in fields such as:

(i) Barrier properties and flame retardancy: Flame retardants are a key component added to potentially flammable materials, including textiles and plastics, to reduce their overall tendency to catch fire. They are widely used in electronics and electrical devices, building and construction materials, furnishings and components of aeroplanes, trains and automobiles. Polymer nanocomposites containing nanoclay as fillers have been found to be

highly efficient flame retardant materials owing to their ability to form protective oxide layers on the material surface [67]. The gas barrier properties of these materials, arising from the dispersion of the clay platelets within the polymer matrix, prevent transport of combustible gases within and out of the system [fig. 1.5]

(ii) Non linear optical properties: Optical limiters have received significant attention in the context of the protection of optical components and human eye from laser-induced damages. Polymer nanocomposite films containing metal nanoparticles as fillers have been found to be highly efficient for this application [68] owing to the high polarizability and ultra fast response provided by the metal nanoparticle fillers.

(iii) Energy storage systems and sensors: Polymer nanocomposites containing fillers such as carbon nanotubes, graphene etc. possess unique magnetic, thermal, conducting properties which have been exploited for the design of materials such as anodes in lithium-ion-batteries, supercapacitors, organic solar cells and highly sensitive devices for high end sensor applications [69-71].

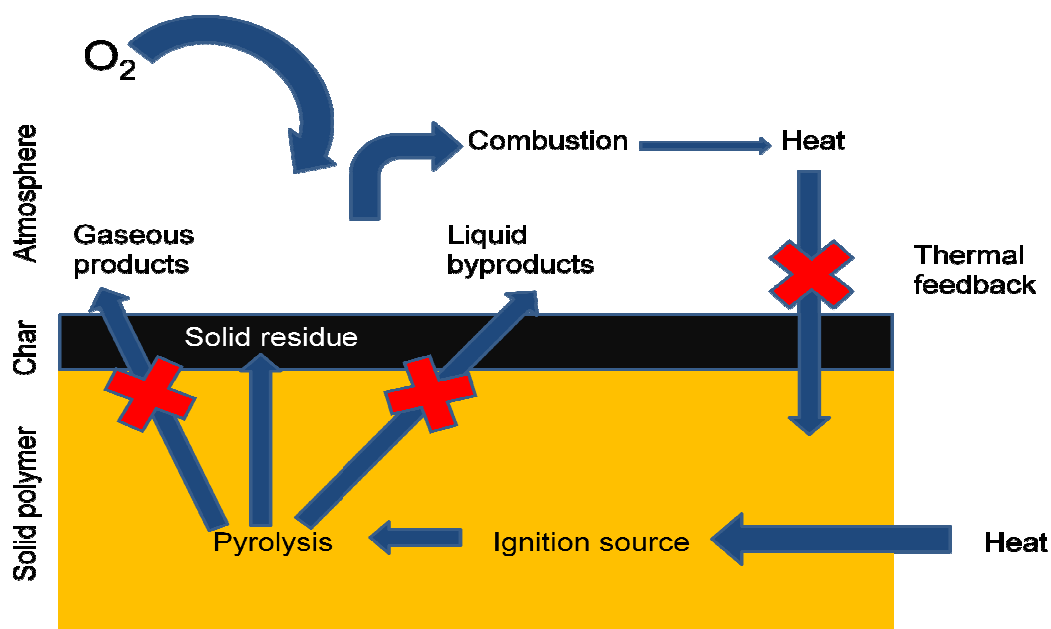


Fig. 1.5 Schematic representation of mechanism of flame retardant property

(iv) Electronics and automobile sectors: The addition of conductive nanoparticles to polymers has a strong impact on the resulting composite dielectric properties. With respect to the aspired integration of passive electronic devices, like resistors, capacitors and others, into the printed circuit board (PCB), new composite materials have been developed which provide huge functionality, compatibility to industrial PCB-fabrication, low overall costs, high reliability and extended life cycle. [72-74]. In the automobile sector, enhanced modulus and dimensional stability, improved scratch and mar resistance, superior thermal and processing properties, reduced warpage of components and enhanced impact resistance makes polymer nanocomposites an ideal replacement for traditionally used materials. The key drivers for the use of polymer nanocomposite-enabled parts in the automotive industry are reduction in vehicle's weight, improved engine efficiency (fuel saving), reduction in CO₂ emissions and superior performance (greater safety, increased comfort and better driveability) [75].

(v) Defence applications: Polymer nanocomposites have also carved out a niche for themselves in the defence sector. High performance fibres/fabrics have been developed and find wide applications in defence as electrically conductive fabrics, sensors, electromagnetic shielding, microwave absorption, electrical energy storage (capacitors), actuators, and materials for micro UAVs. There are also reports of the promising application of nanocomposites in body armour. [76]

1.4. Basic aspects of radiation chemistry

1.4.1. Types and energy of ionizing radiation

Radiation chemistry is a branch of chemistry that studies chemical transformations in materials exposed to high-energy radiations (gamma-rays, X-rays, Electron beams). It uses radiation as the initiator of chemical reactions, as a source of energy that disrupts the sensitive energy balance in stable systems. The energy of ionizing radiation, which also

includes radiation from charged particles (electrons, protons, deuterons, α -particles) or uncharged particle (neutron), lies in the range of 10^2 to 10^7 eV. Interaction of an atom or a molecule with high energy radiation can result in the formation of a wide range of reactive species such as radicals, cations, anions etc [77-79].

The important advantage of radiation chemistry lies in its ability to be used to produce, and study, almost any reactive atomic species playing a part in chemical reactions, synthesis, industrial processes, or in biological systems. The techniques are applicable to gaseous, liquids, solid, and heterogeneous systems. By combining different techniques of radiation chemistry with analytical chemistry, the reaction mechanism and kinetics of chemical reactions are studied.

1.4.2 Interaction of electromagnetic radiation with medium

Electromagnetic radiations such as X-rays (extra nuclear origin) and gamma (γ) rays (originating within the atomic nucleus) belong to the class of ionizing radiations. Gamma rays originating from radioactive isotope sources, such as those derived from ^{60}Co radioisotopes emit radiation of discrete energies (1.332 MeV and 1.173 MeV for ^{60}Co). For a narrow beam, the intensity of gamma radiation transmitted through an absorber is given by the equation:

$$I = I_0 e^{-\mu x} \quad (1.3)$$

Where, I_0 is the incident radiation intensity, x is the thickness of material through which radiation has traversed and μ is the linear attenuation coefficient.

The linear attenuation coefficient is the sum of a number of partial coefficients representing different processes that are initiated within the absorber by the impinging radiation. These include (a) photoelectric effect (b) Compton scattering (iii) pair production (iv) coherent scattering and (v) photonuclear reactions. The energy of the incoming photon and the atomic number (Z) of the absorbing material are the two factors that decide the relative

importance of each of these processes. While coherent scattering is predominant for low energy photons (<0.1 MeV), photonuclear reactions are possible with photons of energies in the range of 2 to 8 MeV for low Z materials and in the region of 7-20 MeV for high Z materials.

(i). **Photoelectric effect:** This process is the principal interaction process at low photon energies ($1 \text{ keV} < E_\gamma < 0.5 \text{ MeV}$), wherein the photon interacts with a bound electron in an atom, and ejects it from the atom by transferring its entire energy. The energy of the ejected electron (E_e) is given by the difference between the energy of the photon (E_o) and the binding energy of the electron (E_b) (Equation 1.4).

$$E_e = E_o - E_b \quad (1.4)$$

(ii) **Compton scattering:** The Compton scattering process is predominant for photons with energy typically around 1 MeV. For low Z materials, Compton scattering is the common phenomenon for photon energies between 30 keV to 20 MeV. In this process a free electron at rest is struck by a photon that scatters off at some angle to its original path. By the conservation of momentum and energy, the electron recoils in a specific direction, with a specific energy. This energy is provided by a reduction in the energy of the incoming photon (increase in its wavelength). The relation between the various parameters is given by equation (1.5). The energy of recoil electron is given by the Equation (1.6).

$$E' = \frac{E_o}{1 + \left(\frac{E_o}{m_e c^2} \right) (1 - \cos \theta)} \quad (1.5)$$

$$E' = E_o - E_e \quad (1.6)$$

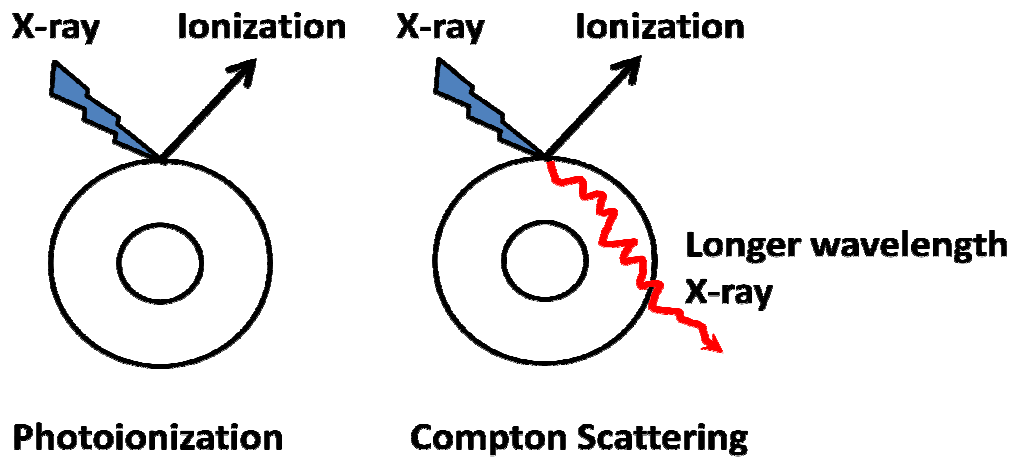


Fig.1.6 Schematic representation of Photoelectric and Compton effects.

iii) Pair production: At photon energies above 1.02 MeV another possibility becomes available when matter is struck by the photon: the creation of particle-anti-particle pairs. This process is the reverse of electron-positron annihilation phenomenon and involves the complete absorption of a photon in the vicinity of an atomic nucleus resulting in the formation of an electron and a positron. Since the rest mass of an electron or positron is 0.511 MeV, for pair production to occur, minimum photon energy must be 1.02 MeV (i.e. $2m_e c^2$)

$$E_0 = E_{e^-} + E_{e^+} + 2m_e c^2 \quad (1.7)$$

Therefore, depending on the incident photon energy, the photon gets attenuated and the total linear attenuation coefficient (μ) is given by Equation (1.8).

$$\mu = \tau + \sigma + \kappa \quad (1.8)$$

where, τ , σ and κ are the linear attenuation coefficient of photoelectric, compton and pair production process respectively.

1.4.3. Interaction of electrons with medium

When an electron hits onto a material, different interactions can occur, which can be broadly categorized as (a) inelastic collision (b) elastic collision (c) emission of

bremstrahlung radiation and (d) Cerenkov emission. The energy of the electrons as well as the nature of the absorbing material decides the relative importance of these processes.

(a) Inelastic Interactions: If energy is transferred from the incident electrons to the sample, then the energy of the electron after interaction (E_{el}) with the sample is consequently reduced compared to its initial energy E_0

$$E_{el} < E_0$$

The energy transferred to the specimen can yield different signals such as X-rays, Auger or secondary electrons, plasmons, phonons, UV quanta or cathodoluminescence. Inelastic scattering is the only process that generates excited or ionized species in the absorber material and results in significant chemical or biological change. Secondary and tertiary electrons are generated as the incident primary electrons are slowed down. The average amount of kinetic energy lost per unit length by electron through coulomb interaction with atomic electrons in a medium is defined as the specific energy loss or stopping power (S) of the medium and is defined by the Bethe's Equation (1.9).

$$S = -\frac{dE}{dx} = \frac{2\pi e^4 N_0 Z}{m_0 v^2} \left[\ln \frac{m_0 v^2 E}{2I^2(1-\beta^2)} - \left(2\sqrt{1-\beta^2} - 1 + \beta^2 \right) \ln 2 + 1 - \beta^2 + \frac{1}{\delta} \left(1 - \sqrt{1-\beta^2} \right)^2 \right] \quad (1.9)$$

Where, e and m_0 represents the charge rest mass of electron, v is the velocity of electron, N_0 is the number of atoms cm^{-3} in the medium, Z is the atomic number and I is the mean excitation potential of the electrons in the stopping material, β is the ratio of v to the speed of light c .

(b) Elastic scattering: In this case, no energy is transferred from the electron to the sample and essentially leads only to a change in the direction of motion of electrons. As a result, the electron leaving the sample still has its original energy E_0 :

$$E_{el} = E_0$$

This phenomenon is more common for electrons with low energy and target with high atomic number.

(c) Emission of bremsstrahlung radiation: Bremsstrahlung, or 'braking radiation', is emitted by high energy electrons moving in the electric field of a nucleus of an atom. The electron gets decelerated and emits energy in the form of electromagnetic radiation, at the expense of its kinetic energy. Bremsstrahlung emission is negligible below 100 KeV but increases rapidly with increasing energy, and is the dominant process at electron energy between 10 - 100 MeV.

(d) Cherenkov emission: Cherenkov radiation takes place when charged particles such as electrons move through a dielectric (i.e., electrically polarizable) medium at a phase velocity greater than the speed of light in that medium. Emission of this radiation (see Figure 1) occurs as the charged particles lose energy inelastically via electric field interactions with the transiently polarized medium. This radiative emission is the predominant process at high electron energies and for high Z materials.

1.4.4. Interactions of charged particles

When a charged particle enters into a medium, it interacts with electrons and nuclei in the medium. These interactions are called "collisions" between charged particles and the atomic electrons and nuclei and can lead to either ionization or excitation within the medium.

The four primary types of interaction of charged particles with matter are:

(a) Inelastic or soft collisions: In this type, the Coulomb force due to moving particle affects the atom as a whole, leading to excitation of the atomic electrons or ionization of the atom.

This is the main process of energy transfer for charged particle interaction with matter.

(b) Hard collisions: In this type of interaction, the charged particle exerts enough impulse to eject an electron from the atom.

(c) Inelastic collisions with a nucleus: The Coulomb force interaction here is mainly with

the nucleus and if the charged particle has enough energy, it can leave the nucleus in an excited state. The nucleus subsequently decays with the emission of nucleons or gamma rays.

(d). Elastic collisions with a nucleus: These types of interactions are known as Rutherford scattering. There is no excitation or emission of radiation in this case and the particle loses energy through recoil of the nucleus.

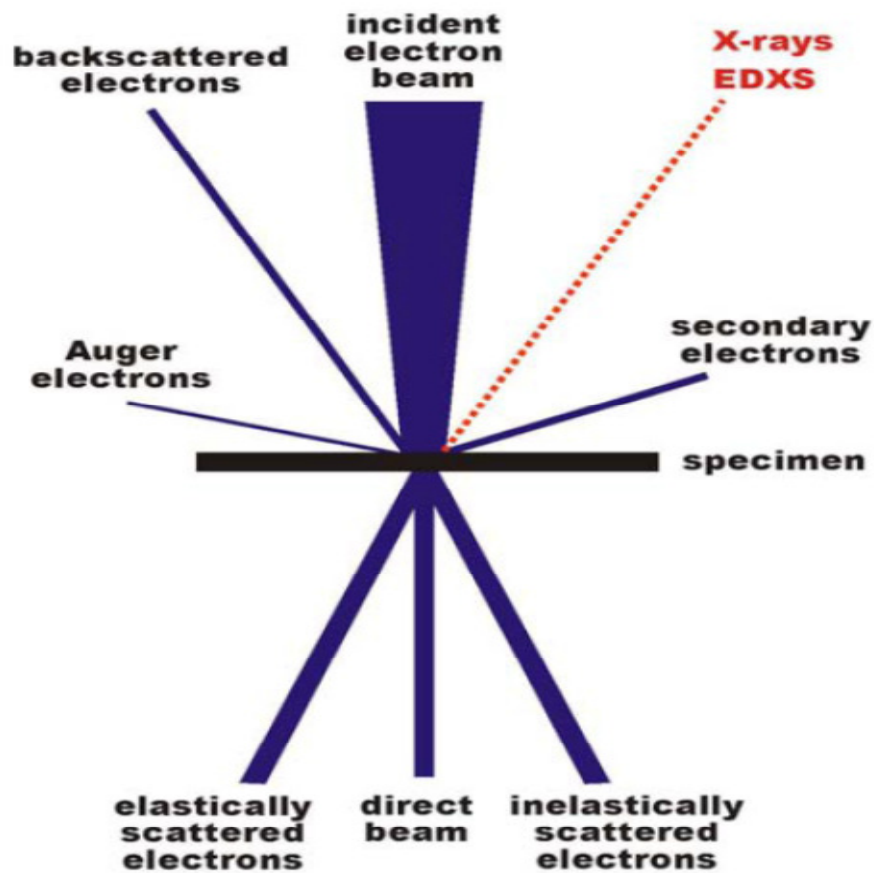


Fig. 1.7 Schematic representation of interaction of electrons with medium

1.4.5 Distribution of active species in the system – track structure

The energy lost when a high energy charged particle is slowed in a medium gives rise to a trail of ionized and excited species along the path of the particle. This trail is commonly referred to as a track [fig 1.8]. A photon imparts a large fraction of its energy to a single electron which subsequently excites and ionizes a large number of molecules along its track. The population of reactive species generated within the track depends on the energy of the impinging radiation.

The electrons liberated in the ionization process can possess a wide range of energies. If the energy of these secondary electrons is less than 100 eV, their range in solids and liquids is short and the ionizations and excitations caused by these electrons also remain restricted to a small range, leading to the formation of small spurs containing reactive species. In water, the isolated spurs contain on an average six active species for every 100eV of energy absorbed. Secondary electrons with high kinetic energy (between 100 and 500eV) deposit their energy to form dense regions of ionization, which look like large spurs. These elongated spurs are called blobs. For electrons of still higher energy (500 to 5000eV) the spurs overlap to form short tracks which are more or less cylindrical in view. In this case, the events are so close to each other that they cannot be considered as isolated. [79]. The typical energy distribution for a 440 keV Compton electron in water is spurs (64%), short tracks (25%) and blobs (11%).

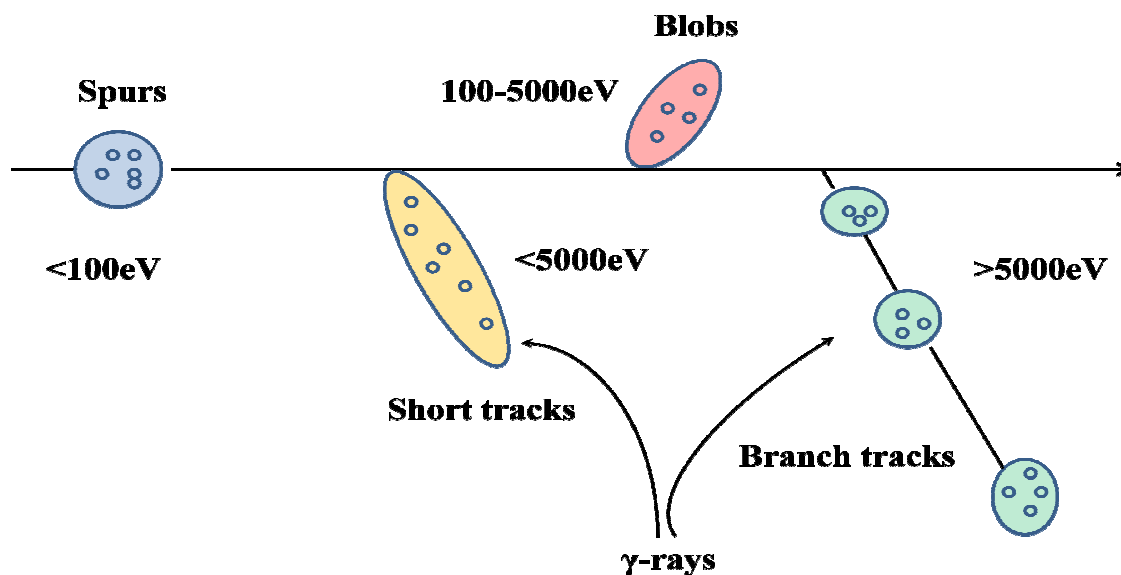


Fig. 1.8 Schematic representation of distribution of active species in medium

1.5. Radiation dosimetry: Radiation-chemical yield and Fricke Dosimeter

When any material is exposed to ionizing radiation, the amount of energy deposited in unit mass of the material is termed as the absorbed dose. It expressed in terms of joules per kilogram (SI units) and its special name is gray (Gy). Another important parameter associated with the absorption of radiation dose by a material is the radiation chemical yield. Radiation chemical yield of any material is the number of molecules transformed per 100eV of energy absorbed. It is defined in terms of its G value. In the SI system, the unit of G is expressed as mol/Joule. G values reported in terms of number of species formed per 100 eV can be converted to SI units using the following relationship (1.10).

$$G (\text{mol } J^{-1}) = G (\text{number per } 100\text{eV}) \times 1.036 \times 10^{-7}$$

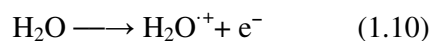
Dosimetry refers to the process of determining the amount of dose delivered by any radiation source to a particular system. The Fricke dosimetry system provides a reliable means for measurement of absorbed dose to water, based on a process of oxidation of ferrous ions to ferric ions in acidic aqueous solution by ionizing radiation. In situations not requiring

traceability to national standards, this system can be used for absolute determination of absorbed dose without calibration, as the radiation chemical yield of ferric ions is well characterized. The dosimeter is an air-saturated solution of ferrous sulfate or ferrous ammonium sulfate that indicates absorbed dose by an increase in optical absorbance at a specified wavelength. A temperature-controlled calibrated spectrophotometer is used to measure the absorbance.

1.6. Radiation chemistry of water

1.6.1 Primary yields

The radiation chemistry of water is of significance since water is the basic component in most biological and chemical systems. [80]. Ionizing radiation produces abundant secondary electrons that rapidly slow down (thermalize) to energies below 7.4 eV, the threshold to produce electronic transitions in liquid water. For both the primary charged particle and the secondary electrons, this slowing down process is accomplished by transfer of energy to the medium in a sequence of discrete events. Depending on the amount of energy transferred to the electron, the molecule can undergo (a) Ionization (b) excitation or (c) thermal transfer. The initial event is the transfer of energy sufficient to cause (multiple) ionizations or excitations in water molecules, resulting in the formation of spurs [79]. Direct ionization of water produces a radical ion and a free subexcitation electron ($E < 7.4$ eV).



Energy transfer can produce a water molecule in an excited state.



The time scale for the creation of these species is on the order of 10^{-16} seconds. In the next step, the three initial species begin to diffuse and react with each other or other molecules in the medium. Energetically unstable positively charged ions (H_2O^+) undergo ion

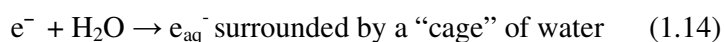
molecule reaction in 10^{-14} seconds producing $\cdot\text{OH}$ radicals [81]. The radical ion of water can dissociate to produce a hydroxyl radical and a hydrogen ion.



The excited water molecule can dissipate excess energy by bond breakage to produce hydroxyl and hydrogen radicals.



Subsequently, the electron released during ionization gradually loses its energy to fall below the ionization threshold of water and finally gets localized in a potential energy well long enough to get captured by water through dipolar interactions to generate a solvated electron: [82]. The entire process is completed in about 10^{-12} seconds.



After $\sim 10^{-12}$ sec, the chemically reactive species viz. $\text{HO}\cdot$, $\text{H}\cdot$, e_{aq}^- are still located in the vicinity of the original H_2O^* , $\text{H}_2\text{O}^{\cdot+}$ and e_{aq}^- species that caused their creation. These species now begin to migrate randomly about their initial positions. As this diffusion proceeds, individual pairs may come close enough together to react with each other.

A variety of reactions are possible in the track of the charged particle.



Most of these reactions remove chemically reactive species from the system. With time ($\sim 10^6$ sec) all of the reactive species diffuse sufficiently far so that further reactions become unlikely.

The chemical development of the track is over by 10^{-6} sec. The species formed can subsequently react with solutes present in the system. In water, 10^{-7} seconds is the lifetime of the radicals reacting at a diffusion-controlled rate with a solute whose concentration is 10^{-3} mol.dm⁻³ [79,80,82].

1.6.2 Important reducing radicals in aqueous solutions

The primary radicals viz. hydrated electron (e_{aq}^-) and the hydrogen atom ($H\cdot$) are reducing in nature. The high redox-potential of e_{aq}^- ($E^\circ = -2.9$ V vs NHE) makes it a powerful reducing agent capable of reducing a range a metal ions to their zero valent states (Table 1.2). Its reactions with solutes are best understood in terms of availability of a suitable vacant orbital in the solute molecule for the electron to get localized [65,72].

1.6.3 Important oxidizing radicals in aqueous solutions

The primary oxidizing radical generated during water radiolysis is Hydroxyl radical ($\cdot OH$) ($E_0 = 2.8$ V vs NHE). In strongly basic solution ($pH > 11.9$), it is deprotonated to give O^- .

1.7 Synthesis of metal nanoparticles and nanocomposites by high energy radiation: advantages of radiolytic method

As previously discussed, numerous techniques have been developed and demonstrated over the years for fabrication of metal nanoparticles and polymer nanocomposite coatings. However, with growing environmental concern and greater emphasis being laid on green chemistry, most of these techniques, which involve harsh reaction conditions or use of harmful chemical reagents have been found to be inadequate to meet the stringent regulatory

requirements. Therefore, of late, the focus has shifted to the application of radiation technology for fabrication of materials in large scale. The numerous benefits of using radiation technology can be summarized as follows:

- (a) Unlike chemical methods, the radiolytic route of synthesis does not require the use of harmful chemical reducing agents or initiators to carry out the reactions. Radicals generated in situ during radiolysis are sufficient to carry out the reactions. Thus materials prepared via radiolytic route are cleaner since they are devoid of chemical impurities.
- (b) Compared to conventional methods, radiolytic reduction/ curing techniques ensure more uniform and complete reaction to produce materials with superior properties.
- (c) Radiation sources can initiate reactions at room temperature and therefore do not require the use of high temperature.
- (d) Radiation sources such as Electron beam provide high throughput and fast processing and are therefore commercially viable options to achieve bulk production of processed materials.

1.8. Scope of the thesis

Noble metal nanoparticles and polymer nanocomposite materials are being explored for their applications in diverse fields ranging from sensing to materials with superior mechanical and thermal properties. Radiation technology presents itself as an attractive tool for fabrication of these materials owing to the multitude of advantages it offers vis a vis conventional methods of synthesis. Radiation induced synthesis of metal nanoparticles as well as radiation induced curing of polymer nanocomposite films are environment benign techniques with minimal carbon footprint, and can rightly be highlighted as the technology of the future. Moreover, the technique provides materials with superior properties and offers better control over reaction parameters. In this work, radiation sources such as ^{60}Co gamma, Electron beam and Synchrotron radiation source have been exploited to engineer nanomaterials for sensing

applications and polymer nanocomposite films for various optical, tribological and thermal applications. The materials designed have been studied and thoroughly characterized using numerous techniques such as UV-visible spectroscopy, TEM, SEM, AFM, Thermal analysis etc. Brief descriptions of the chapters in this thesis are presented below.

Chapter 2 describes the materials, instrumentation and methods employed during the course of the doctoral work

Chapter 3 highlights the gamma radiation synthesis and characterization of uniformly dispersed Gold nanoparticles stabilized by a biocompatible polymer Poly(N-vinyl-2-pyrrolidone) (PVP). The sensing property of the PVP stabilized Au nanoparticles was also investigated for estimation of trace levels of hydrogen peroxide and mercury ions in aqueous solutions.

Chapter 4 presents a comparative study of the synthesis and structural characterization of PVP stabilized Silver nps fabricated using ^{60}Co gamma, Electron beam and Synchrotron radiation techniques. Silver nanoparticles synthesized via gamma radiolytic route were also demonstrated to have good sensing property by highlighting their application as a LSPR based optical sensor for estimation of trace levels of uric acid in human and bovine serum samples.

Chapter 5 describes the application of gamma and electron beam irradiation techniques for synthesis of polymer nanocomposite films for various targeted applications. Aliphatic urethane acrylate based films containing in situ metal nanoparticles and other nanofillers were designed using Electron beam irradiation technique. Non tacky, homogeneous, thin films obtained by this technique were characterized by techniques such UV-visible spectroscopy, TEM and FE-SEM analysis, and subsequently studied for their optical limiting applications. Similar films containing organophilic modified montmorillonite clay as nanofillers were also fabricated via gamma radiation curing technique and their mechanical

and thermal properties thoroughly studied. The films were also demonstrated to have flame retardant properties, thus making them potential candidates for flame retardant materials.

Chapter 2: Experimental Methodology and characterization techniques

2.1. Introduction

The present work involved the use of a three primary radiation sources for the radiation engineering of new materials and a multitude of instruments for the characterization of these materials. These include steady-state irradiation facilities like ^{60}Co gamma irradiation chamber, Electron beam and Synchrotron irradiators for irradiation, and characterization techniques such as Transmission Electron Microscopy (TEM), Scanning Electron Microscopy (SEM), Atomic Force Microscopy (AFM), X-ray Scattering (SAXS and XRD), Fourier Transform Infrared Spectroscopy (FTIR), Elemental Analysis (EA), Thermal Analysis (TGA and DSC), UV-visible Spectroscopy, Zeta Potentiometers, Nd-YAG Laser, Gloss at 60 degrees and Pendulum hardness testers for characterization of the radiation synthesized materials. The chapter discusses the principles and methodologies involved in these studies.

2.2. Gamma radiation source

A Gamma irradiation source, Gamma Chamber- 5000, supplied by the Board of Radiation & Isotope Technology (BRIT), Mumbai, INDIA was employed for irradiation of reaction mixture solutions. Figure 2.1 depicts the layout of gamma chamber used in these studies. Gamma chambers mainly consist of a set of stationary Cobalt-60 (^{60}Co) source placed in a cylindrical cage surrounded by a lead shield. The shield is provided around the source to keep external radiation field well within the permissible limits. The material for irradiation is placed in an irradiation chamber located in the vertical drawer inside the lead flask. The drawer can be moved up and down with the help of a system of motorized drive, which enables precise positioning of the irradiation chamber at the center of the radiation field. ^{60}Co radioisotope emits two γ rays of energy 1.33 and 1.17 MeV.

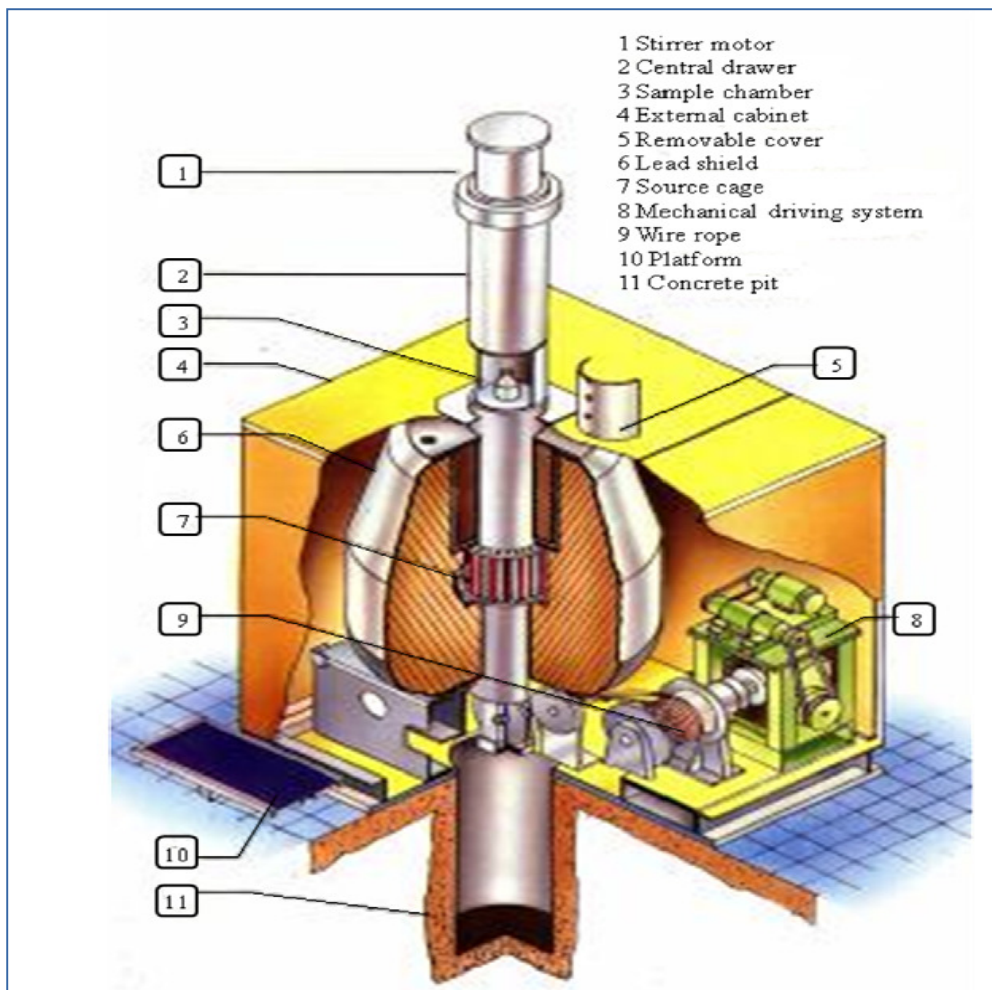


Fig. 2.1 Schematic diagram of a Gamma Chamber (GC-5000).

2.2.1. Dosimetry of gamma chambers

Knowledge about the amount of energy absorbed per unit mass and distribution of the absorbed energy in any absorbing material is essential in order to quantify the physical, chemical or biological changes induced by exposure of the said material to the ionizing radiation. Radiation dosimetry is the term applied to describe the process of quantification of radiation effects of a given radiation source. Any device or process employed to carry out dosimetry is known as a radiation dosimeter. Some of the important terms associated with the process are:

(i). **Absorbed dose:** It is defined as the amount of energy absorbed per unit mass of the irradiated material. The SI unit for the absorbed dose is Joules/kilogram (J.kg^{-1}), termed as gray (Gy) [83]. The older unit is Rad ($1 \text{ rad} = 0.01 \text{ Gy}$) [84].

(ii). **Absorbed dose rate:** The dose absorbed per unit time is termed as the absorbed dose rate. The unit used for absorbed dose is Gy.s^{-1} .

Dosimetry conditions and classifications:

The absorbed dose measured by the dosimeter will represent the dose absorbed by the sample only when the following conditions are satisfied: (a) the dosimeter as well as the sample are both homogeneous, (b) both have similar size, density and atomic composition, and (c) both are irradiated under identical conditions. The simple and convenient method to achieve these conditions is to use equal volumes of dilute solutions of both sample and dosimeter, and irradiate them in turn under identical conditions. However, since exact duplication of reaction conditions is very often not attainable, certain approximations and relations are used to determine the absorbed dose for a given sample. For electromagnetic radiation like ^{60}Co gamma-rays, the absorbed dose in the dosimeter (D_d) and sample (D_s) are related by the equation (2.1).

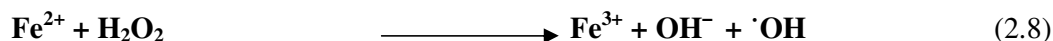
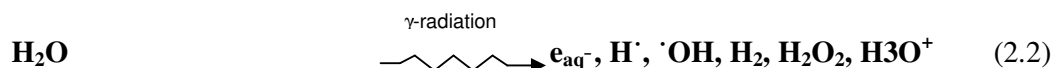
$$D_s = \frac{D_d \times \left(\frac{Z}{A}\right)_s}{\left(\frac{Z}{A}\right)_d} \quad (2.1)$$

Where, Z/A is the ratio of the atomic number (Z) to the atomic weight (A) for an element and the ratio of the sum of the atomic numbers of the element present to the molecular weight for a compound.

Dosimeters can be classified into two categories viz. primary dosimeters and secondary dosimeters. Primary dosimeters involve physical measurement of any parameter

such as temperature rise in a calorimeter, ionization produced in a gas or the charge carried by a beam of charged particles of known energy [85]. If the dosimeter response to radiation needs to be calibrated against a primary dosimeter, it is termed as a secondary dosimeter. This includes Fricke dosimeter, nylon film dosimeter, solutions of various dyes, perspex dosimeters etc [86]. The state of the system, dose range to be monitored and nature of radiation are the primary parameters that need to be taken into account while deciding upon the type of dosimeter to be used.

The dose rate of gamma chamber GC-5000 was measured by Fricke dosimetry prior to carrying out any experiment. The basic principle underlying the mode of operation of a Fricke dosimeter is the radiation induced oxidation of ferrous ions to ferric ions in acidic aqueous solutions in the presence of oxygen [87-90]. The standard Fricke dosimeter comprises of an aerated solution of $1.0 \times 10^{-3} \text{ mol.dm}^{-3}$ ferrous ammonium sulphate, $1.0 \times 10^{-3} \text{ mol.dm}^{-3}$ NaCl and 0.4 mol.dm^{-3} sulphuric acid (pH= 0.46). The reactions involved in the Fricke dosimeter are summarized under reactions (2.2) – (2.8).



The yield of ferric ion is related to the primary radical and molecular yields by equation (2.9)

$$G_{(Fe^{2+})} = 2G_{(H_2O_2)} + 3[G_{(e_{aq}^-)} + G_{(H^+)}] + G_{(OH)} \quad (2.9)$$

As evident from eqns. 2.8 and 2.5, each molecule of hydrogen peroxide is responsible for the oxidation of two ferrous ions. The reducing radicals i.e. e_{aq}^- and $H\cdot$ each oxidizes three ferrous ions via a sequence of reactions involving $HO_2\cdot$, H_2O_2 and $\cdot OH$ respectively. The number of moles of Fe^{3+} ions (M) produced upon irradiation is determined by monitoring the UV- visible absorption spectra of Fe^{3+} , which absorbs at 304 nm with an extinction coefficient of $2205 \pm 3 \text{ dm}^3 \cdot \text{mol}^{-1} \cdot \text{cm}^{-1}$. The accepted $G(Fe^{3+})$ value for a Fricke dosimeter solution of density $1.024 \text{ gm. ml}^{-1}$ and for electron and photon radiation in the range of 1 to 30 MeV is 15.5 i.e. $1.606 \times 10^{-6} \text{ mol.dm}^{-3} \cdot \text{J}^{-1}$ at 25°C . The absorbed dose (D) is derived in terms of Gray using the expression

$$D_d = 2.77 \frac{\Delta D}{I} \quad (2.10)$$

Where ΔD is the change in absorption of the solution at 304nm I is the path length in metres.

The Fricke dosimeter can be used to accurately determine dose only up to 400 Gy., since the gradual depletion of oxygen within the system with increasing radiation dose leads to inconsistencies in the $G(Fe^{3+})$ value. The Fricke dosimeter is independent of dose rate between 0.2 and $2.0 \times 10^6 \text{ Gy.s}^{-1}$. A modified version of Fricke dosimeter, also known as super Fricke dosimeter, has also been designed and is independent of dose rate upto absorbed dose rates of the order of 10^8 Gy.s^{-1} . The upper limit of absorbed dose that can be measured using a super Fricke dosimeter is 2.0 kGy. The system comprises of $10^{-2} \text{ mol.dm}^{-3}$ ferrous ions under oxygenated condition but in the absence of sodium chloride.

2.3. Electron beam source

The electron beam processing was carried out in 2 MeV, 20 kW industrial electron beam (EB) accelerator at BARC, Mumbai, India. The industrial electron beam accelerator is ILU-6 type, pulse linear accelerator. The machine is designed to deliver a dose (average) of ~2.0 kGy/pass at the centre. The beam is uniformly scanned over a length, thus constituting an irradiation area of 1000 cm². The machine is housed in a shielded cell having a labyrinth with separate entry and exit ports where power roller conveyor system has been installed for the material transport in & out of the irradiation zone.

2.4 Synchrotron radiation source

X-ray irradiations were carried out using BL- 7 (white beam, storage ring energy = 2.5 GeV, maximum current= 300 mA), INDUS-2 synchrotron facility at RRCAT, Indore, India. The X-ray beam energy was 1.5-20keV and the beam size approximately (80×10) mm². The X-ray irradiation of samples was carried out in polypropylene press-fit cap storage vials.

2.5 Characterization techniques

2.5.1. UV-visible spectrophotometer

The absorption spectra of aqueous metal nanoparticles absorption were recorded on a Thermoelectron - Evolution 300 uv-visible spectrophotometer in the wavelength region of 250-1000 nm. UV-visible absorption spectroscopy is a useful technique for characterization of noble metal nanoparticles [91], which exhibit distinct Localized Surface Plasmon Resonance bands in the UV-visible range. The high extinction coefficient and highly sensitive surface plasmon property of metal nanoparticles, which is strongly dependant on the size, shape and environment of the particles, makes UV-visible spectroscopy a highly

efficient tool for gathering qualitative information about the particle morphology and to exploit their optical properties for sensor applications.

The absorbance behaviour of any material can be explained in terms of the Beer Lambert's Law. The absorbance value (A) depends on nanoparticle concentration (c), path length (l) of measuring cell and extinction coefficient of nanoparticles (ϵ) (Equation 2.11).

$$A = \epsilon cl \quad (2.11)$$

The surface plasmon band characteristics are dependent on a number of factors such as particle size, shape, nature of stabilising agent and temperature, extent of aggregation, presence of any adsorbate on the surface of nanoparticles, nature of the surrounding medium etc. [92-94]. The plasmon bandwidth increases with decreasing size of the nanoparticles in the intrinsic size region i.e. when the particle size is less than 25 nm, and increases with increasing size in the extrinsic size region (mean diameter larger than 25 nm) [95]. The increase in size is manifested as a red shift in the surface plasmon band [96] whereas a decrease in size is normally accompanied by a blue shift in the peak position.

2.5.2 FTIR spectrophotometer

The FTIR spectra of samples were recorded in ATR mode using diamond single reflectance ATR assembly in FTIR spectrometer (Affinity-1, Shimadzu, Japan) using resolution of 4cm^{-1} and with data acquisition run of 25 scans for each sample. FTIR gives information regarding the structure and functional groups of a given molecule. More importantly, FTIR analysis is useful for conducting analysis of polymer composition and molecular structure.

The primary component of an FTIR comprises of a Michelson Interferometer, which, in turn, consists of:

- A broad-band light source which emits light covering the mid-IR range,
- A beamsplitter made of KBr or CsI,
- Two front surface coated mirrors – one moving and one fixed, and
- A detector.

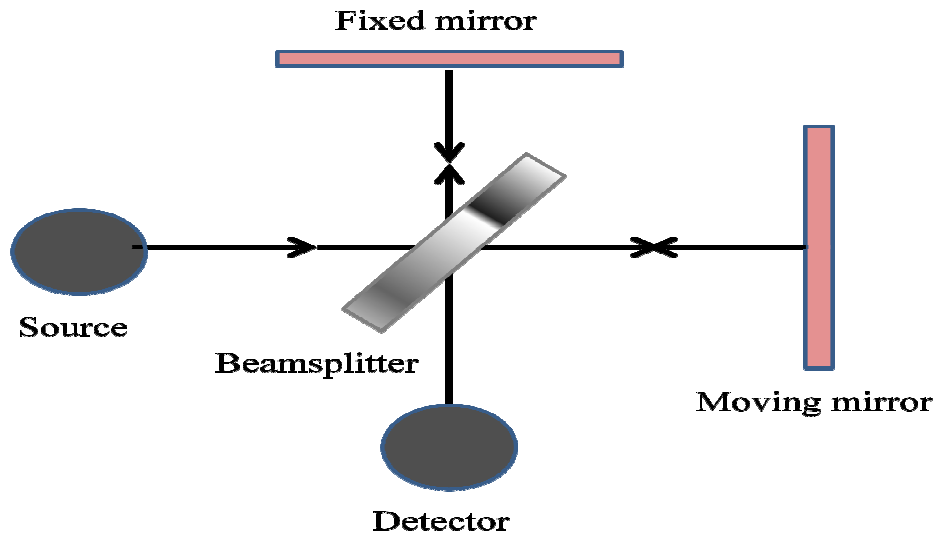


Fig. 2.2 Schematic diagram of a Michelson Interferometer.

The working principle of Michelson Interferometer involves light from the source being split into two parts by the 50/50 beamsplitter and reflected from the two mirrors (fixed and moving) to again reach the beamsplitter. The two beams reaching the detector have an optical path difference determined by the positions of the two mirrors, i.e. they have a fixed phase difference. Therefore the two beams interfere either constructively or destructively for a particular frequency depending on the position of the moving mirror. The resultant sinusoidal signal generated is termed as Interferogram and the corresponding spectrum – frequency against intensity plot, is computed using Fourier transform.

2.5.3 Thermogravimetric analysis (TGA)

The non-isothermal thermogravimetric measurements were carried out with TGA/DSC1 system with gas controller system (GC100) from Mettler Toledo, Switzerland, to determine the thermal degradation behavior of Gamma radiation cured PCN films. For TG experiments ~10 mg of the powder sample was taken in alumina crucible and heated in temperature range of 35 to 850°C at heating rate of 10°C.min⁻¹ under inert dynamic high purity nitrogen atmosphere at a flow rate of 50ml min⁻¹.

TGA gives important information regarding the thermal degradation behaviour of polymers and composite materials [97]. Any changes in the thermal behavior of a material on incorporation of a filler can be detected using this technique. The residual weight observed in case of certain polymer nanocomposite materials can also be indirectly used for predicting the flame retardant behavior of the material.

The basic instrumental requirements for TGA are a precision balance with a pan loaded with the sample, and a programmable furnace. The furnace can be programmed either for a constant heating rate, or for heating to acquire a constant mass loss with time. The TGA instrument continuously weighs a sample as it is heated. As the temperature increases, various components of the sample are decomposed and the weight percentage of each resulting mass change can be measured. Results are plotted with temperature on the X-axis and mass loss on the Y-axis.

2.5.4. Differential scanning calorimetry (DSC)

Glass transition temperature (T_g) of the samples was determined by a differential scanning calorimetry (DSC) using DSC 823e system from Mettler-Toledo, Switzerland. For all experiments ~10 mg of the sample was taken in standard aluminum pan and heated to 250°C at heating rate of 20°C.min⁻¹ followed by cooling to -50°C at cooling rate of 20°C.min⁻¹

¹, and then again heated to 250°C at heating rate of 20°C.min⁻¹. All the cooling and heating cycles were carried out under inert dynamic high purity nitrogen atmosphere at a flow rate of 50ml min⁻¹. The T_g values of PCN samples were estimated from the second heating cycle.

DSC is an extremely sensitive thermoanalytical technique that can be employed to determine the minute physical transformations that a sample can undergo at different temperatures [97,98]. The underlying principle of the technique is to maintain both the sample and the reference material at the same temperature by regulating the amount of heat flowing into or out of the sample.

2.5.5. TEM

Transmission electron microscopy (TEM) of metal nanoparticles in solution was performed on an Energy filtering transmission electron microscope (EF-TEM, LIBRA 120, Carl Zeiss) with an accelerating voltage of 120 kV. For the measurement of TEM a drop of dilute metal nanoparticle solution was placed on a carbon coated copper grid and dried in a Laminar flow hood before it was observed under the microscope. In case of solid samples, TEM images of the samples were carried out using a bench top Transmission Electron Microscope (LVEM5, Cordouan Technologies, France) operated at 5kV in electron scattering mode for higher contrast. Prior to analysis, samples were sliced into ultrathin sections of 30nm thickness using an ultramicrotome and collected on to 400 mesh Cu grids.

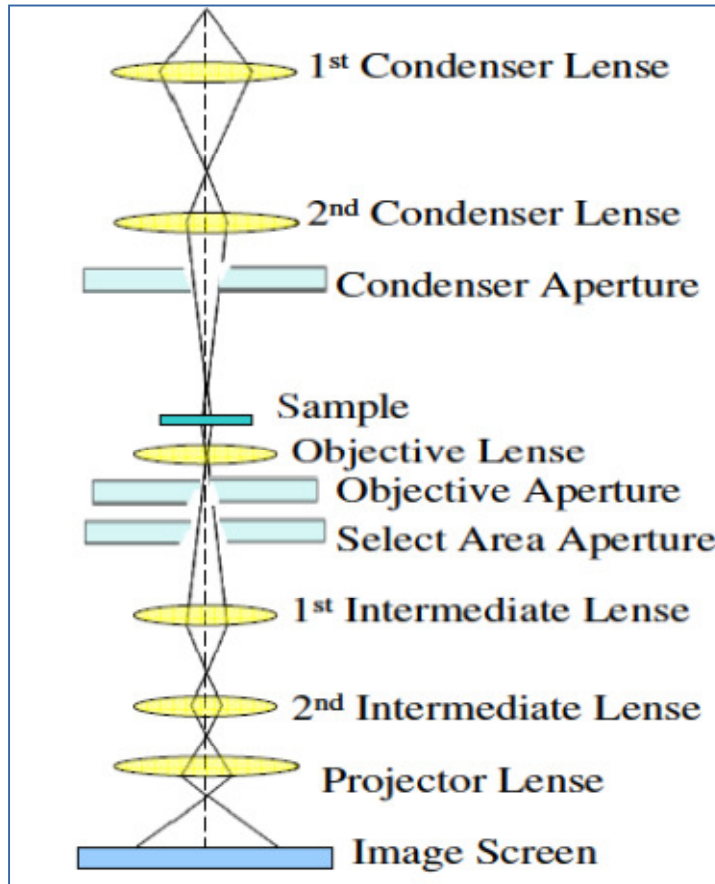


Fig. 2.3 Schematic representation of TEM

Transmission electron microscope (TEM) is the most widely used technique to characterize metal nanoparticles. The short wavelength electron beam used as the source ensures extremely high resolutions that are not attainable using an ordinary light beam as a source. The final image is projected onto a phosphor screen by the beam transmitted through the sample. TEM machines equipped with additional accessories can provide information regarding topography, morphology, dispersity, composition and crystallography of the sample. HRTEM (high resolution TEM) can achieve magnifications as high as $\sim 10,00,000\times$ with a resolution of $\sim 1 \text{ \AA}$ [99].

2.5.6. Scanning electron microscopy (SEM)

The surface morphologies of samples were investigated by SEM analysis using VEGA MV2300T/40 (TS 5130 MM) microscope (TESCAN) at acceleration voltage of 5kV. SEM images of the cross-section of the nanocomposite coatings were taken at 10kx magnification, after the gold coated fractured coating films were fixed vertically on to a conducting steel stub surface using conducting carbon paste.

SEM involves the scanning of the sample surface with an electron beam of accelerating voltage < 50kV. The secondary or backscattered electrons collected by the detector are analyzed for obtaining the final image. SEM provides information about the topography and morphology of the sample and it can attain upto 1,00,000x magnification with a resolution of ~1.5 nm [100].

2.5.7. Atomic Force Microscope (AFM)

AFM is a powerful analytical tool which provides information regarding the surface morphology and phase through the production of a 3D map of the sample surface. AFM measurements were performed using an NT-MDT solver model P47 instrument (Russia) with 50 μ m scanner head and silicon nitride tip in contact mode. The sample for AFM measurement was prepared by depositing a dilute solution of silver nanoparticles on a glass slide and allowing it to dry in a Laminar flow hood.

2.5.8. Particle size analyzer (PSA)

The hydrodynamic diameter of Ag nanoparticles was measured using Particle Size Analyzer (VASCO 3, Cordouan, France). For the analysis, 0.5 ml of dilute silver nanoparticle solution was placed on the glass base, the laser count rate adjusted to approximately 2000 counts per second and the acquisition was performed for 4 minutes in the continuous mode at

25⁰C. The measurement was replicated three times per sample to ensure reproducibility of obtained results.

VASCO uses the thermal motions of particles in suspension (Brownian Motion) to determine their size. Here the sample suspension is irradiated by a laser and the light scattered in a certain direction detected with high time resolution. From the fluctuation of the intensity of the scattered light, the mobility of the particles can be calculated and then again via the Stokes-Einstein formula, their size can be calculated.

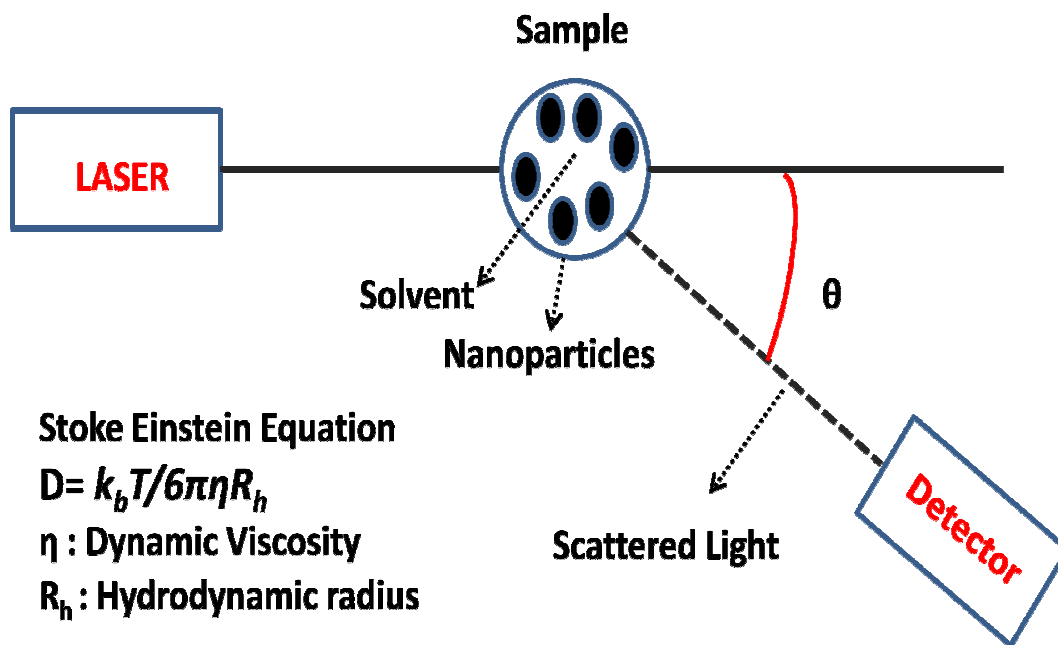


Fig. 2.4 Schematic representation of Particle Size Analyzer Laser

2.5.9. X-ray Diffraction analysis (XRD): Small angle X-ray scattering (SAXS) and X-ray diffraction (XRD)

SAXS measurements were performed using a laboratory based SAXS facility using CuK α source. The diameter of the incident photon beam on the sample was 0.4 mm. The SAXS detector was mounted at a sample-to-detector distance of 1.07 m, corresponding to a 2θ range of 0.1–3.5 degrees. The magnitude of the scattering wave vector, $s=2\sin\theta/\lambda=q/2\pi$, where 2θ is the scattering angle and the used wavelength $\lambda=0.154\text{nm}$. In order to access further higher scattering angles above 3.5 degrees, X-ray diffraction (XRD) experiments were performed using a diffractometer using CuK α source in θ - θ geometry with 2 deg/min scanning speed.

XRD is a tool used for identifying the atomic and molecular structures, as well as for determining the interlayer spacings in case of samples having layered structures. It operates on the basis of the Bragg's Equation:

$$n\lambda = 2d \sin \theta \quad 2.12$$

where n is an interger (1, 2, 3,, n), λ the wavelength, d the distance between atomic planes, and θ the angle of incidence of the x-ray beam and the atomic planes.

2.5.10 Zeta Potential analyzer

Zeta potential of the samples was determined using a Malvern Zetasizer nano ZS. 1.5 ml of the sample was taken in the transparent cell for carrying out the zeta potential measurements at pH 7.4. Zeta potential is a measure of the magnitude of the electrostatic or charge repulsion/attraction between particles, and is one of the fundamental parameters known to affect stability. Its measurement brings detailed insight into the causes of dispersion, aggregation or flocculation, and can be applied to improve the formulation of dispersions, emulsions and suspensions.

2.5.11. Nd-YAG laser system

The optical-limiting behaviors of the composites with different Ag NPs concentrations were measured using Nd:YAG laser with 25 ns pulse duration and 355 nm wavelength. The experiment set-up is shown in Fig. 2.5 The sample was mounted on a metal frame and the laser beam focused on the sample surface with a spot size of 1.0 mm diameter. The incident and transmitted energy were detected simultaneously by two power meters (P1, P2).

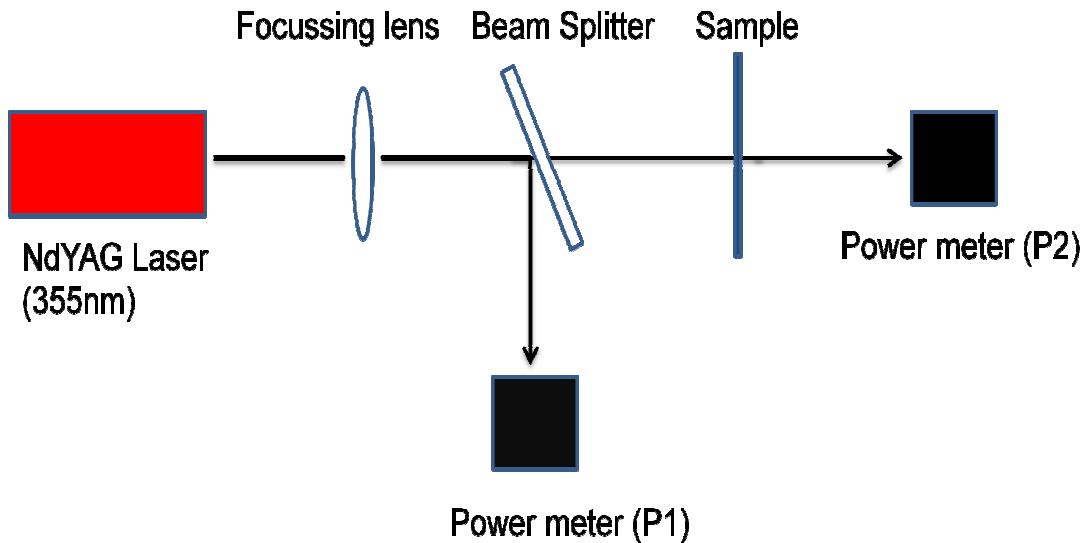


Fig. 2.5 Schematic representation of ND-Yag Laser system

2.5.12. ASTM property evaluation techniques

The gamma radiation cured coatings were tested for different end performance properties, as per guidelines of standard test methods, viz. Pendulum Hardness (ASTM: D 4366) and Gloss at 60⁰ angle (ASTM: D 523-99).

Pendulum Hardness (ASTM: D 4366): The instrument consists of a pendulum which is free to swing on two balls resting on a coated test panel. The pendulum hardness test is based on the principle that the amplitude of the pendulum's oscillation will decrease more rapidly when

supported on a softer surface. The hardness of any given coating is given by the number of oscillations made by the pendulum within the specified limits of amplitude determined by accurately positioned photo sensors. An electronic counter records the number of swings made by the pendulum

Gloss at 60⁰ angle (ASTM: D 523-99): Gloss is associated with the capacity of a surface to reflect more light in directions close to the specular than in others. Measurements by this test method correlate with visual observations of surface shininess made at roughly the corresponding angles, commonly 60⁰. The factors that affect gloss are the refractive index of the material, the angle of incident light and the surface topography.

2.6. Chemical reagents

All aqueous solutions were prepared in ultra pure water with resistivity=18MΩ.cm produced in water purification system 'Ultraclear TWF UV' (SG Wasseraufbereitung & Regenerierstation GmbH, Germany). Prior to use, glassware was cleaned with aquaregia (volume ratio HNO₃/HCl = 1: 3). Hydrogen tetrachloroaurate trihydrate (99.99%) from MV laboratories, India, Silver Nitrate (99.9%), 2-propanol, acetone, citric acid and sodium citrate from S. D. Fine Chemicals Ltd., India, modified montmorillonite clay (Cloisite 20A, Cloisite 30B) and aliphatic urethane acrylate (AUA, Cognis) from Southern Clay Ltd., USA were used as received. For preparation of buffer solutions, Disodium hydrogen phosphate and potassium dihydrogen phosphate, were purchased from Thomas and Baker chemicals, India. Glycine (S.D. Fine, India) and MES (Sigma Aldrich) were used to prepare buffer solutions of pH 3.0 and 6.0, respectively, while Tris.HCl (Sigma Alrich) was used to prepare buffer solutions of pH 8.0, 10.0 and 11.0. Capping agents poly(N-vinyl-2-pyrrolidone)s (PVPs) (molecular weights 40,000; 1,60,000 and 3,60,000Da), o-phenylenediamine (o-PDA), Horseradish peroxidase (HRP) (300 units/mg), Hydrogen peroxide (30 wt % in water),

Mercury(II)nitrate($>98\%$), Uric acid ($\geq 99\%$), Uricase and Trimethylolpropanetriacrylate (TMPTA) were all purchased from Sigma Aldrich.

Chapter 3: Gamma radiolytic synthesis of Poly(N-vinyl-2-pyrrolidone) capped Au nanoparticles for sensor applications

3.1. Introduction

Metal nanoparticles find application in a wide array of fields including catalysis [101], chemical and bio sensors [102,103], antibacterial substances [104] and drug delivery systems [105]. Noble metal nanoparticles, in particular, such as those of Au and Ag show intense Localized Surface Plasmon Resonance (LSPR) absorption in the visible region [106] and have potential applications as optical biosensors [107,108] or catalytic systems [109,110] for initiating a variety of organic reactions. The high surface area provided by these nanoparticles make them extremely efficient as catalytic materials to carry out reactions that are otherwise difficult to initiate [111]

Although literature provides numerous chemical methods for fabrication of noble metal nanoparticles, most of these methods involve the use of toxic chemical reducing agents or harsh reaction conditions. Therefore, in recent years, radiolytic reduction route for generation of metal nanoparticles has emerged as an attractive alternative technique to these chemical reduction methods. Irradiation by gamma radiation, such as ^{60}Co gamma irradiation, involves not only more convenient and simpler control parameters for engineering nanoparticles of desired morphology but also presents itself as a clean, environment friendly, room temperature technique that does not involve the use of any external reducing agents [112-115]. The reactive species generated through radiolysis can easily reduce metal ions down to zero valent state. Furthermore, because of the ability to fine-tune the radiation dose, dose rate and to selectively generate the required transient reactive radicals, radiation technology offers better control over the size and the size distribution. Thus, nanoparticles fabricated by radiation technology can be employed as highly efficient catalytic or sensing

materials. The choice of capping agent/ stabilizer during synthesis of metal nanoparticles is also crucial since it decides the overall stability and morphology of the particles generated, which in turn decides the long term utility of the system as a facile catalytic or sensor system.

One of the most promising and widely used capping agents for metal nanoparticle stabilization is Poly (N-vinyl-2-pyrrolidone) (PVP) (Pimpang et al, 2011; Wang et al, 2005; Borodko et al, 2006). PVP possesses functional groups, such as $>C=O$ and $>N-$ and a long polymer chain. These functional groups contain lone pairs of electrons which help in stabilization of metal nanoparticles at their surface through covalent interaction, while the polymer chain restricts aggregation of metal nanoparticles by steric hindrance. Apart from this, PVP is a biocompatible polymer. Hence nanoparticles synthesized in PVP can have potential biological applications.

The estimation of biologically relevant molecules such as Hydrogen peroxide is one of the primary applications that has been targeted using PVP stabilized metal nanoparticles. Hydrogen peroxide is widely used as an oxidant, a disinfectant and a bleaching agent in various industries, such as textile, paper and pulp, pharmaceutical industries [116]. It causes irritation to eye, skin and mucous membrane when present in the environment. Hydrogen peroxide is also produced in stoichiometric amounts during oxidation of biological analytes (e.g. glucose) by dissolved oxygen in the presence of corresponding oxidase. Hence micro and trace level determination of hydrogen peroxide is considerably important in clinical chemistry, analytical biochemistry and environmental science. Existing methods for the determination of hydrogen peroxide include titrimetry [117], spectrophotometry [118], kinetic flow-injection method [119], fluorescence [120], enzymatic method [121], chromatographic techniques [122] and electrochemical methods [123]. However most of these methods suffer from limitations in terms of specificity, selectivity, kinetically instability or incompatibility with aqueous environments. Recently a new method for determination of

hydrogen peroxide based on a peroxidase-catalyzed reaction and using Au nanoparticles has been reported [124].

Similarly, the unique optical properties of metal nanoparticles can also be exploited for the estimation of trace levels of Mercury in the environment. Mercury is a widespread pollutant with distinct toxicological profiles, and it exists in a variety of different forms such as metallic, ionic, and as part of organic and inorganic salts and complexes. The quantification of mercury in aquatic ecosystems in particular is of considerable interest since exposure to high levels of Hg^{2+} is detrimental to physical health and can cause brain damage and other chronic diseases [125-127]. At the same time routine estimation of Hg^{2+} is essential for evaluating the safety of aquatically derived food supplies [128]. As per World Health Organization guidelines, the permissible limit of inorganic mercury in drinking water is $6\mu\text{g/L}$, while the total body burden of mercury for adult humans should not exceed 20-30mg. The methods currently used for the determination of Hg^{2+} include atomic absorption spectrometry [129], inductively coupled plasma-mass spectrometry [130], selective cold vapor atomic fluorescence spectrometry [131], organic fluorophores/chromophores [132-135], semiconductor nanocrystals [136,137], cyclic voltammetry [138,139], etc., all of which are rather complicated, time-consuming, and costly as well as inappropriate for point-of-use applications. To overcome these drawbacks, several techniques have been developed for the simple, rapid detection of Hg^{2+} in aqueous solutions. Colorimetric methods, in particular, are extremely attractive because they normally involve visible changes which can be seen with the naked eye.

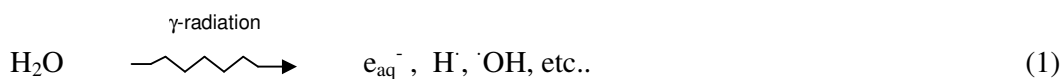
The present chapter reports a facile method for synthesis of gold nanoparticles (Au NPs) in PVP using high energy gamma radiation. Various experimental parameters such as Au^{3+} precursor ion concentration, PVP concentration, molecular weight of PVP have been optimized to obtain Au NPs of desired size and size distribution. H_2O_2 concentration in

aqueous solution was determined by monitoring the oxidation of o-phenylene diamine (o-PDA) by H₂O₂ in presence of enzyme, horse radish peroxidase (HRP). Radiolytically synthesized PVP-Au-NPs have also been employed as a LSPR based optical sensor for the estimation of trace levels of Hg ions in aqueous environments. The estimation of Hg²⁺ is based on the selective interaction of the metal ion with PVP, which gets manifested as a change in the LSPR band of PVP-Au NPs.

3.2. Synthesis of Au nanoparticles

3.2.1. Formation of Au nanoparticles and their characterization

The radiolytic reduction has been proven to be a powerful tool for producing uniform and highly dispersed metallic clusters. When a N₂ purged aqueous solution containing Au³⁺ precursor ions, PVP and 2-propyl alcohol is subjected to gamma irradiation, radiolysis of water takes place, generating reactive transient species, such as e_{aq}⁻, H[·], [·]OH (Eq. 1). Radiolytic species e_{aq}⁻ and H[·] are reducing in nature, whereas [·]OH acts as an oxidizing agent. Therefore, 2-propyl alcohol is used to transform the entire reaction medium in to a reducing one; 2-propyl alcohol reacts with H[·] and [·]OH to generate 2-propyl radical (Eq. 2), which is a mild reducing agent capable of reducing Au³⁺ to metal in zero valent state, i.e., Au³⁺ to Au⁰ (Eq. 3). The overall reduction in the medium is therefore carried out by the two reducing species, namely (CH₃)₂C[·]-OH and e_{aq}⁻ (Eq. 4)



The formation of Au⁰ is followed by coalescence step leading to formation of Au clusters in presence of PVP as a capping and stabilizing agent. PVP contains functional groups like >C=O and >N [140], which facilitate anchorage of metal nanoparticles and help in regulating the size of the Au-nanoparticles. These PVP-Au NPs show characteristic surface plasmon band at around 522nm. Figure 3.1 shows that the yield of PVP-Au NPs increases with increase in absorbed radiation dose till all precursor Au³⁺ ions are exhausted. The saturation dose for reduction of 5×10⁻⁴ mol.dm⁻³ Au³⁺ was determined to be 1.8 kGy. The TEM image (Figure 3.2) reveals PVP-Au NPs fabricated using PVP of molecular weight 3,60,000 Da as the stabilizer are spherical in nature with average particle size ranging between 6-13nm.

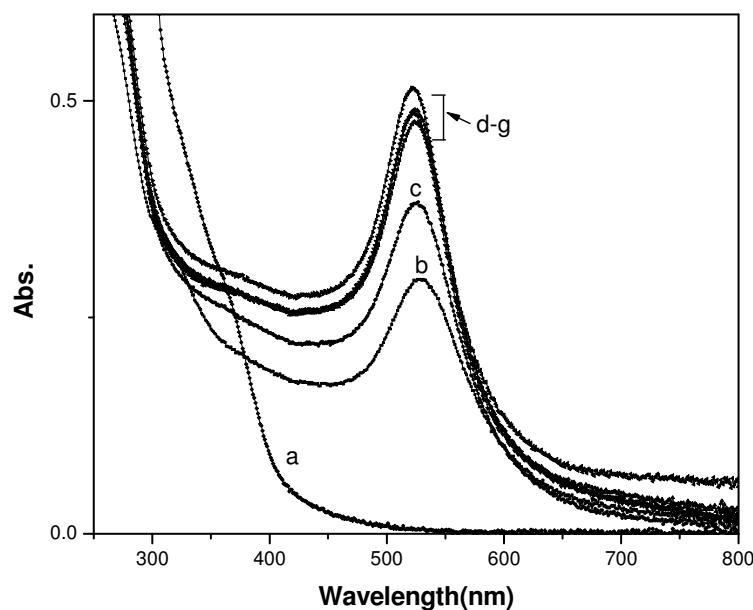


Fig. 3.1 Absorption spectra of aqueous Au nanoparticle solution obtained at radiation dose (a) unirradiated reaction mixture, (b) 0.5kGy, (c) 0.9kGy, (d) 1.3kGy, (e) 1.5kGy, (f) 1.6kGy, (g) 1.8kGy

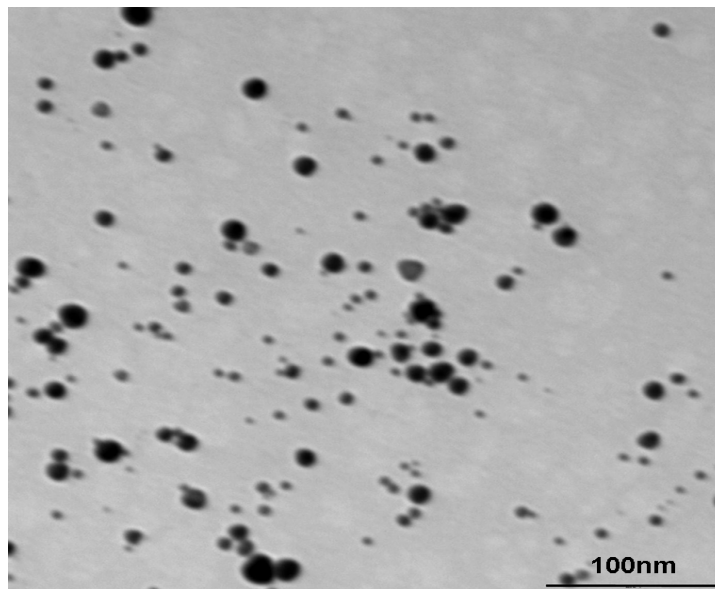


Fig. 3.2 TEM image of Au nanoparticles prepared using PVP of molecular weight 3,60 kDa

3.2.2. Effect of variation of Au^{3+} concentration

Figure 3.3 presents the UV-visible spectra of PVP-Au NPs as a function of radiation dose. It was observed that as the Au^{3+} concentration increased from $1 \times 10^{-4} \text{ mol dm}^{-3}$ to $1 \times 10^{-3} \text{ mol dm}^{-3}$ the intensity of the LSPR band also increased indicating increase in yield of PVP-Au NPs. An initial red shift of 27nm was recorded as the precursor ion concentration increased from $1 \times 10^{-4} \text{ mol dm}^{-3}$ to $4 \times 10^{-4} \text{ mol dm}^{-3}$. This can be attributed to the fact that at lower precursor concentrations smaller nuclei are generated because of lower local concentration and beyond a certain size the growth is arrested with the exhaustion of Au^{3+} ions, leading to formation of smaller particles, which absorb at lower wavelength. Beyond $4 \times 10^{-4} \text{ mol dm}^{-3}$ of Au^{3+} concentration, there was not much shift in spectral peak as well as FWHM of the spectra.

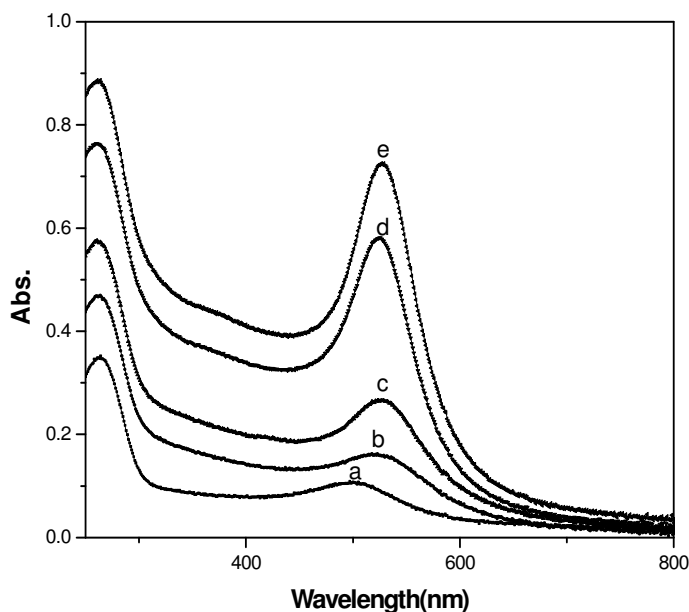


Fig. 3.3 Absorption spectra of aqueous Au nanoparticle solution obtained for Au³⁺ concentration (a) 1×10^{-4} , (b) 2.5×10^{-4} , (c) 4×10^{-4} , (d) 8×10^{-4} , (e) 1×10^{-3} mol.dm⁻³

3.2.3. Reduction under milder condition

The presence of acetone was observed to affect the spectral behaviour of PVP-Au NPs (figure 3.4). In the absence of acetone, the two prominent reducing species are e_{aq}^- and 2-propyl radical. e_{aq}^- ($E^0 = -2.9$ V_{NHE}) is a stronger reducing agent than 2-propyl radical. Acetone scavenges the aqueous electrons generated via radiolysis to produce 2-propyl radical ($E^0 = -1.8$ V_{NHE}) (Eqⁿ 2), which are relatively weak reducing agents. Therefore, in presence of acetone and 2-propyl alcohol, the only reducing agent in the system is 2-propyl radical [141], thereby resulting in slower reduction rate of the precursor ions. The slower reduction rate, in turn, yields a narrower particle size distribution, which gets manifested as a narrower LSPR band for the PVP-Au NPs.

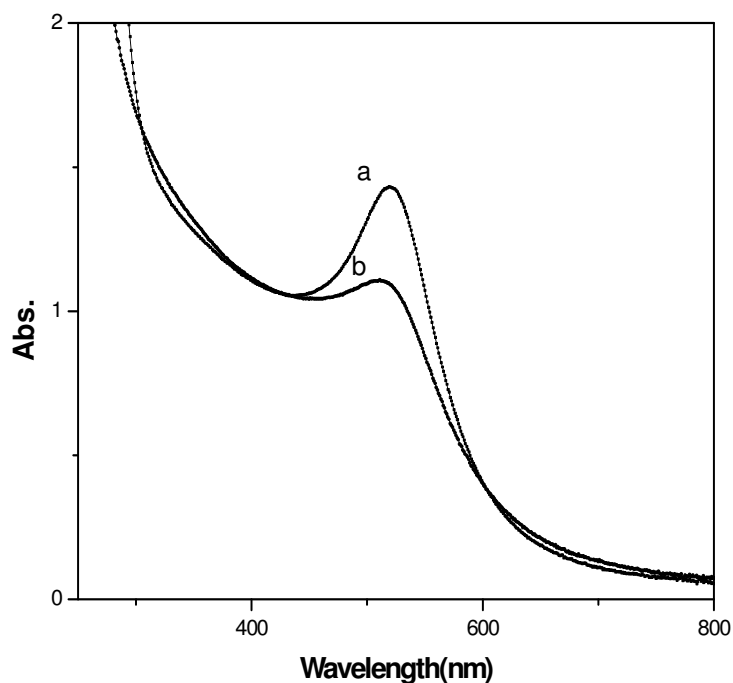


Fig. 3.4 Absorption spectra of $4 \times 10^{-4} \text{ mol.dm}^{-3}$ aqueous Au nanoparticle solution (a) in presence of acetone and (b) in absence of acetone

3.2.4. Role of AgNO_3 in nanoparticle formation

The role of addition of trace quantities of Ag^+ ions during Au NPs formation was also investigated. It was observed that the spectrum was narrower in presence of Ag^+ ions (figure 3.5), indicating more uniform size distribution. Ag^+ in minute concentrations ($6 \times 10^{-5} \text{ mol.dm}^{-3}$) is known to adsorb upon certain faces of the Au crystal, leading to controlled growth. However, there is not much change in the spectral pattern of the PVP-Au NPs for Ag^+ in the concentration range of $6 \times 10^{-5} \text{ mol dm}^{-3}$ to $1.5 \times 10^{-4} \text{ mol dm}^{-3}$. Beyond this concentration, a blue shift was observed in the spectra, which can be attributed to the formation of an Au-Ag alloy nanostructure [142]

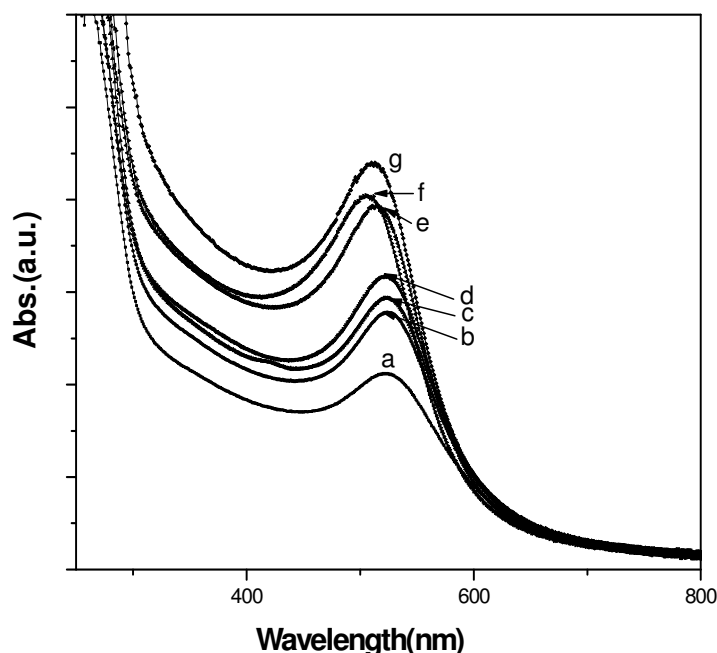


Fig. 3.5 Absorption spectra of aqueous Au nanoparticle solution ($4 \times 10^{-4} \text{ mol.dm}^{-3}$) obtained in presence of (a) 0, (b) 6×10^{-5} , (c) 1×10^{-4} , (d) 1.5×10^{-4} , (e) 2×10^{-4} , (f) 3×10^{-4} , (g) $4 \times 10^{-4} \text{ mol.dm}^{-3} \text{ Ag}^+$ ions

3.2.5. Effect of variation of PVP concentration

The effect of variation of PVP concentration on Au nanoparticle formation was also monitored. Figure 3.6 shows the absorption spectra for $4 \times 10^{-4} \text{ mol dm}^{-3}$ Au nanoparticle solution at various concentrations of PVP ($M_w = 3,60,000\text{Da}$). With increase in concentration of PVP from 0.1% to 2% (w/v) irregular spectral broadening was observed. This result is contrary to results that were previously observed for other capping agents [143]. With increase in PVP concentration from 0.1% (w/v) to 0.5% (w/v), the intensity of the LSPR band also increased. But further increase in PVP concentration to 1% and 2% resulted in a decrease in intensity of the LSPR band. Hence an optimum concentration of PVP is essential to achieve maximum concentration of stable Au nanoparticles.

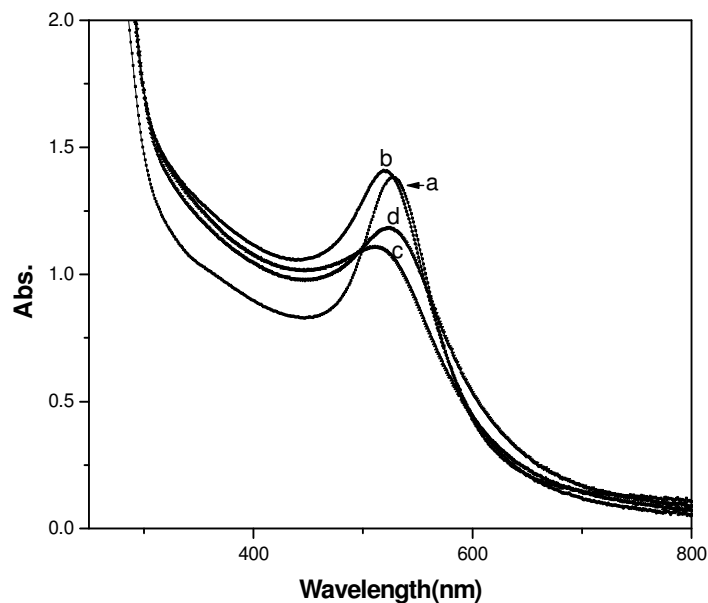


Fig. 3.6 Absorption spectra of 4×10^{-4} mol.dm⁻³ aqueous Au nanoparticle solution obtained for PVP concentrations (a) 0.1%, (b) 0.5%, (c) 1% and (d) 2% (w/v)

3.2.6. Effect of PVP molecular weight on Au nanoparticle formation

The molecular weight of PVP plays a very important role in controlling the shape and size of Au nanoparticles (figure 3.7). Au nanoparticles stabilized by PVP having molecular weight 40,000 Da show a single intense peak at 533nm and PVP having molecular weight 1,60,000 Da and 3,60,000 Da show similar broad peaks at 513nm and 520nm respectively. For higher molecular weight PVP, only spherical Au NPs with a little variation in size were generated, as confirmed from the TEM analysis. This observation can be explained on the basis of the fact that higher molecular weight PVP has longer polymeric chains which stabilize the metal colloids in a more efficient manner, thereby restricting anisotropic growth of the particles and confining them to spherical dimensions.

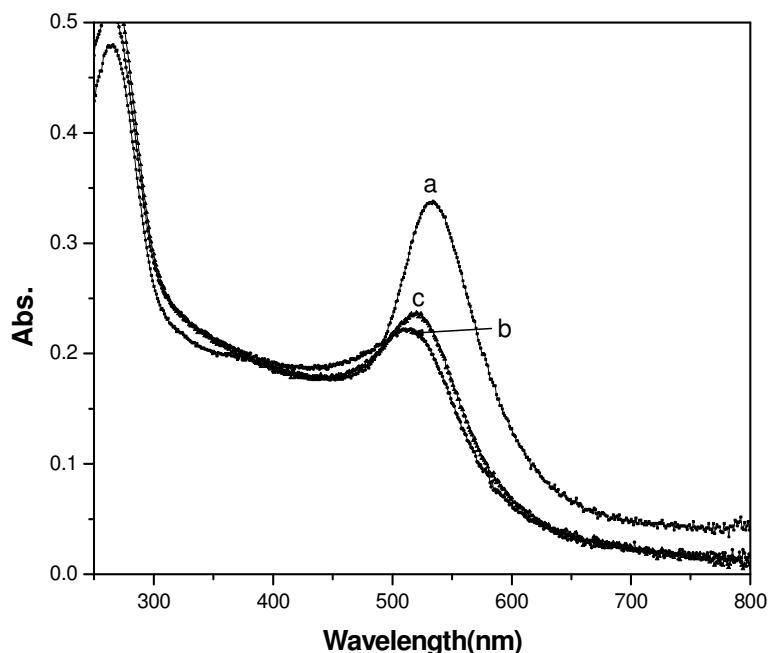


Fig. 3.7 Absorption spectra of aqueous Au nanoparticle solution obtained for PVP of molecular weight (M_w) (a) 40,000Da, (b) 1,60,000Da, (c) 3,60,000Da

3.3. Estimation of Hydrogen Peroxide (H_2O_2)

3.3.1. Detection principle

The estimation of hydrogen peroxide using PVP-Au NPs is based on the enzymatic oxidation of o-PDA by H_2O_2 in presence of enzyme Horse radish peroxidase (HRP) [124]. In aqueous solutions 2,3-diaminophenazine (DAP) is the main product [fig. 3.8]. DAP has two Ns forming part of the central ring and two NH_2 groups. The lone pairs of these Ns interact with the Au NPs, thereby leading to a change in the external environment which gets manifested as a change in the intensity of DAP, which absorbs at $\sim 427nm$.

Briefly, for H_2O_2 estimation in the concentration range of $2.5 \times 10^{-6} \text{ mol.dm}^{-3}$ to $2 \times 10^{-4} \text{ mol.dm}^{-3}$, a reaction mixture comprising of $1 \times 10^{-4} \text{ mol.dm}^{-3}$ o-PDA, 125 ml of 0.125mg/10 ml of HRP and a pre determined concentration of H_2O_2 was diluted to 20mL

using 0.01mL citrate buffer solution and incubated at room temperature for 30 min to allow the completion of the enzymatic oxidation of o-PDA. To this reaction mixture was added 5ml of $5 \times 10^{-4} \text{ mol dm}^{-3}$ PVP-Au NPs solution. The resulting solution was allowed to stand for another 30 min and subsequently the absorption spectra were recorded in the wavelength range of 250–800nm. For estimation of H_2O_2 at lower concentration range, the concentration of the substrate i.e. o-PDA was decreased to $5 \times 10^{-5} \text{ mol dm}^{-3}$. The concentration of all the other reagents was kept unchanged and an identical protocol was adopted.

The oxidation products of o-PDA have a weak absorption peak at 427nm. The PVP-Au NPs were observed to significantly enhance the intensity of this weak absorption peak. With varying concentration of H_2O_2 there is a systematic change in the absorption peak at 427nm, as highlighted in figure 3.9. The detection efficiency of the PVP-Au NPs system was found to be independent of the molecular weight of the stabilizing agent i.e. PVP, and displayed similar results when PVPs of molecular weights 40kDa and 160kDa were used as stabilizing agents in addition to PVP of molecular weight 360kDa.(Figure 3.9 inset).

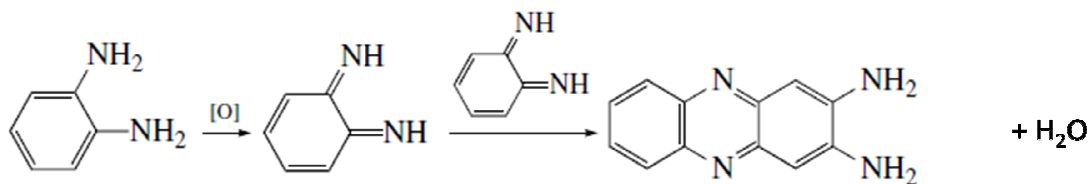


Fig. 3.8 Enzymatic oxidation of OPD

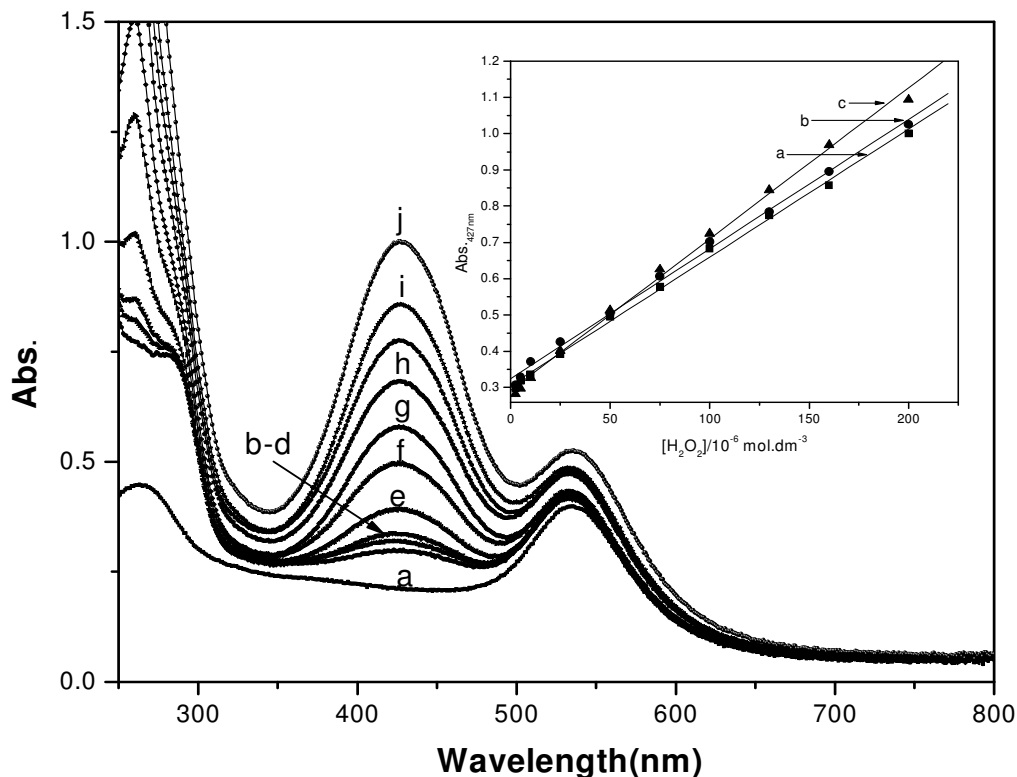


Fig. 3.9 Absorption spectra of reaction medium containing OPD, HRP, H_2O_2 and Au nanoparticles (in PVP, $M_w = 3,60,000$) in citrate buffer with varying H_2O_2 concentration (higher range of H_2O_2 concentration) (a) 0, (b) 2.5×10^{-6} , (c) 5×10^{-6} , (d) 1×10^{-5} , (e) 2.5×10^{-5} , (f) 5×10^{-5} , (g) 7.5×10^{-5} , (h) 1×10^{-4} , (i) 1.3×10^{-4} , (j) 1.6×10^{-4} , (k) $2 \times 10^{-4} \text{ mol.dm}^{-3}$ (Inset: Linear plot of absorbance at 427nm vs H_2O_2 concentration incase Au nanoparticle used was in PVP of molecular weight (a) 3,60,000Da ($R=0.9986$), (b) 1,60,000Da ($R=0.9981$), (c) 40,000Da ($R=0.9981$): H_2O_2 concentration range= 2.5×10^{-6} to $2 \times 10^{-4} \text{ mol.dm}^{-3}$)

3.3.2. Detection limits

The response of the PVP-Au NPs based detection system was observed to be linear in the H_2O_2 concentration range of $2.5 \times 10^{-6} \text{ mol dm}^{-3}$ to $2 \times 10^{-4} \text{ mol dm}^{-3}$ with correlation factor $R > 0.998$ irrespective of PVP molecular weight. To estimate lower concentrations of H_2O_2 , $5 \times 10^{-5} \text{ mol dm}^{-3}$ o-PDA was taken and all other reagents and experimental procedure kept same as above. The spectral change with change in concentration of H_2O_2 is shown in

figure 3.9. The response was found to be linear in the range of 1×10^{-7} mol. dm^{-3} to 3×10^{-6} mol dm^{-3} H_2O_2 concentration with correlation factor $R = 0.995$ (figure 3.9 inset). The detection limit in this case was observed to be 1×10^{-7} mol. dm^{-3} . The proposed method therefore can be used for estimation of H_2O_2 over a wide concentration range of 1×10^{-7} mol dm^{-3} to 2×10^{-4} mol dm^{-3} by tuning a single reaction parameter as per requirement.

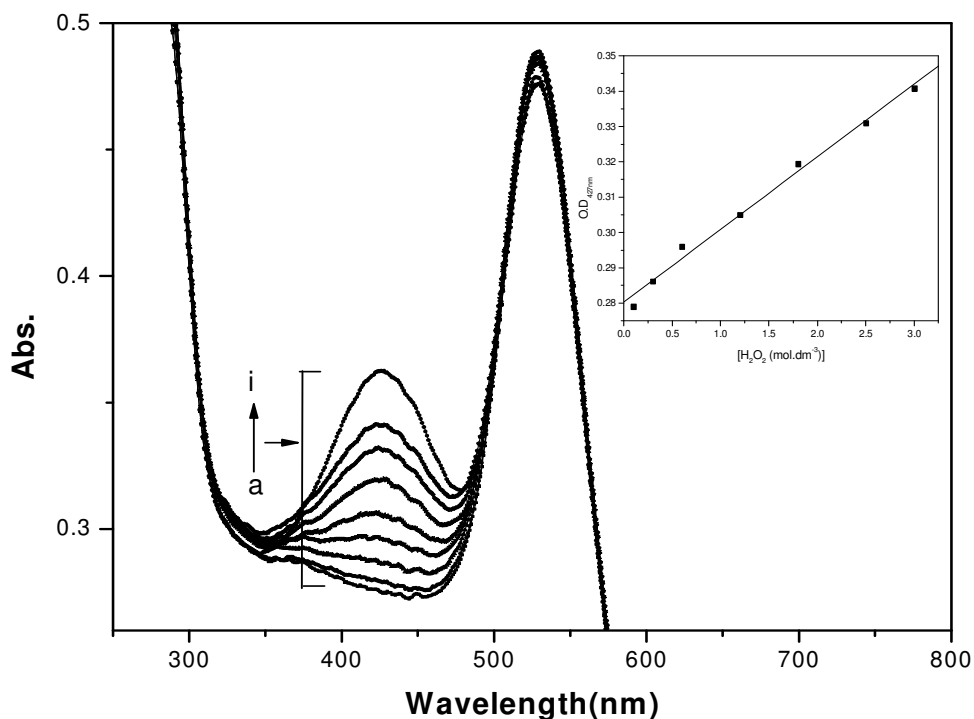


Fig. 3.10 Absorption spectra of reaction medium containing OPD, HRP, H_2O_2 and Au nanoparticles (in PVP, $M_w = 3,60,000$) in citrate buffer with varying H_2O_2 concentration (lower range of H_2O_2 concentration) (a) 0, (b) 1×10^{-7} , (c) 3×10^{-7} , (d) 6×10^{-7} , (e) 1.2×10^{-6} , (f) 1.8×10^{-6} , (g) 2.5×10^{-6} , (h) 3×10^{-6} , (i) 5×10^{-6} mol. dm^{-3} (Inset: Linear plot of absorbance at 427nm vs H_2O_2 concentration incase Au nanoparticle used was in PVP of $M_w = 3,60,000$ Da($R=0.9954$): H_2O_2 concentration range= 1×10^{-7} to 3×10^{-6} mol. dm^{-3})

3.4 Estimation of Mercury ions

3.4.1 Detection principle

The presence of Mercury ions in water as a toxic pollutant necessitates the detection of these ions upto extremely low concentrations. The estimation of Hg^{2+} ions in aqueous media by PVP-capped Au nanoparticles is based on the selective complexation of Hg^{2+} ions with PVP. [144,145]. Guner et al [145] reported that compared to anions, cations such as Hg^{2+} , Cd^{2+} , Co^{2+} etc. exhibit high degree of intramolecular complexation with PVP. The complexation occurs between one cation and two or more carbonyl groups of the lactam rings. The process of covalent complexation can be best explained in terms of the HSAB (Hard Soft Acid Base) principle. Since Hg^{2+} is a soft acid owing to its large ionic radius and high polarizability, the probability of its complexation with the carbonyl groups (soft base with large radius) is maximum compared to the relatively harder metal ions. This results in the selective interaction of Hg^{2+} with PVP, which culminates in the shifting of the SPR band of PVP-capped Au NPs.

In this method, a 50 μM (final concentration) of PVP capped Au NPs system was used for estimation of Hg^{2+} ions in aqueous medium. Different volumes of a 2 μM stock solution of Hg^{2+} ions prepared in TRIS buffer of pH 10.0 were added to a fixed volume of PVP-Au NPs solution also maintained at pH=10.0. Addition of the metal ion resulted in an instantaneous color change from blight yellow to near colourless. The UV-visible spectra of the reaction mixtures were taken and the λ_{max} plotted as a function of Hg^{2+} concentration. A linear relation was obtained for Hg^{2+} concentrations from 0 to 500nM with $R^2=0.991$ and a minimum detection limit of 40nM

The effect of addition of Hg^{2+} on the morphology of PVP-Au NPs was monitored by TEM. As evident from fig. 3.11a, control Au NPs are uniformly dispersed spherical particles with an average diameter of 6.4 nm. However, addition of 500nM Hg^{2+} induces rapid change

in the morphology of the PVP-Au-NPs from spherical to larger (mean diameter of 8.3 nm), irregular sized particles (Fig 3.11b) with broader size dispersion compared to the control sample. This can be explained on the basis of preferential interaction of Hg^{2+} with capping/stabilizer molecules (PVP), which leads to reduced interaction of the PVP molecules with Au atoms. This subsequently results in decrease in the stabilization of Au clusters and enhances their tendency to agglomerate. Fig.3.11c depicts the TEM image of the PVP-Au-NPs system five minutes after addition of Hg^{2+} ions. The process of agglomeration of smaller clusters undergoes near completion within the short time span to give rise to bigger Au agglomerates (with the particle size ranging between 19 and 40 nm).

The hydrodynamic diameter of the PVP-Au-NPs was determined using a particle size analyzer. Particle size analysis also revealed the particles obtained by radiolytic process to be of uniform size distribution with average hydrodynamic diameter of around 52.16 nm. (fig. 3.12a). Addition of Hg^{2+} ion solution to the PVP-Au NPs system resulted in an increase in the particle size distribution accompanied by an increase in the average particle size (fig.3.12b). This further corroborates the results obtained through TEM analysis.

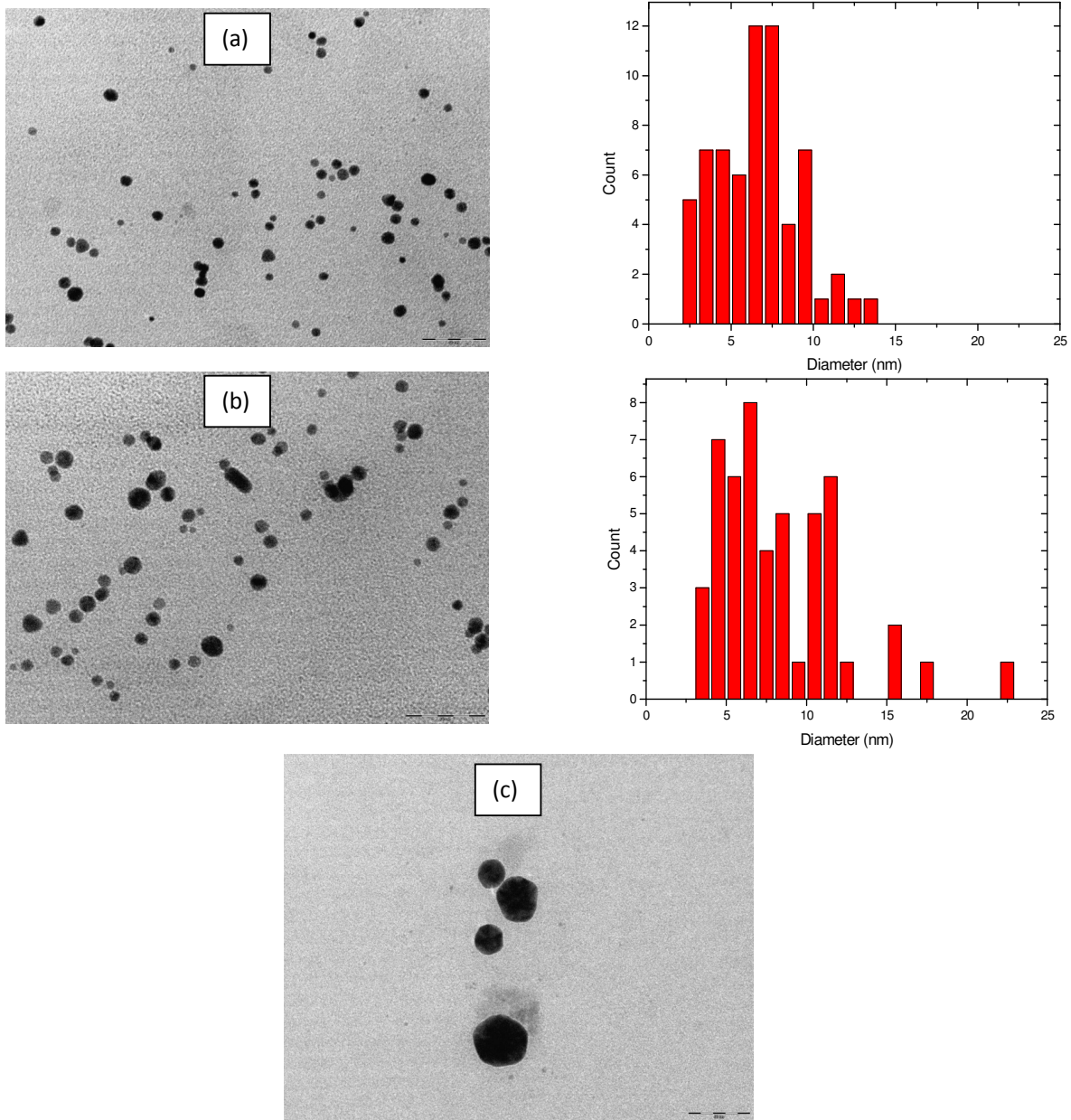


Fig. 3.11 TEM images of PVP-Au-NPs in (a) absence of Hg^{2+} ions (b) immediately after addition of 500nM Hg^{2+} (c) 5 minutes after addition of Hg^{2+}

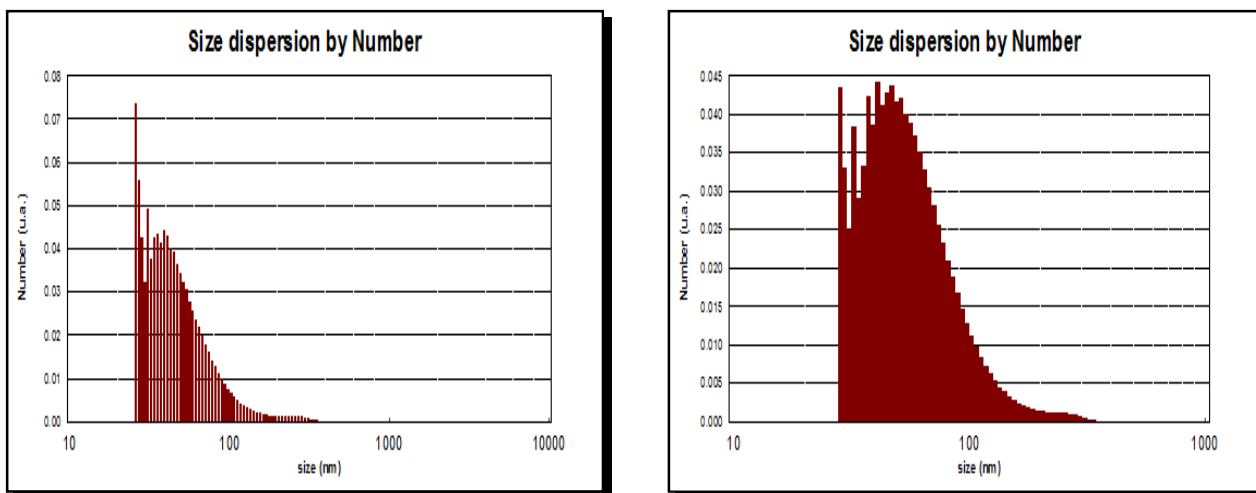


Fig. 3.12 Particle size analysis of Au nps in (a) absence of Hg^{2+} ions and (b) immediately after addition of 500nM Hg^{2+}

The change in particle morphology on addition of Hg^{2+} can also be deduced from the changes observed in the LSPR band of PVP-Au NPs (fig. 3.13). Control PVP-Au NPs yielded a single, narrow peak at $\sim 530\text{nm}$, indicative of uniform sized particles. On the other hand, addition of Hg^{2+} resulted not only in a decrease in the SPR band intensity but also in a slight red shift in the peak at 530nm. Simultaneously, for Hg^{2+} concentrations of 300nm and beyond, a prominent second broad peak appeared at $\sim 740\text{nm}$, indicative of the agglomeration and loss of structure of the PVP-Au NPs caused by addition of Hg^{2+} ions.

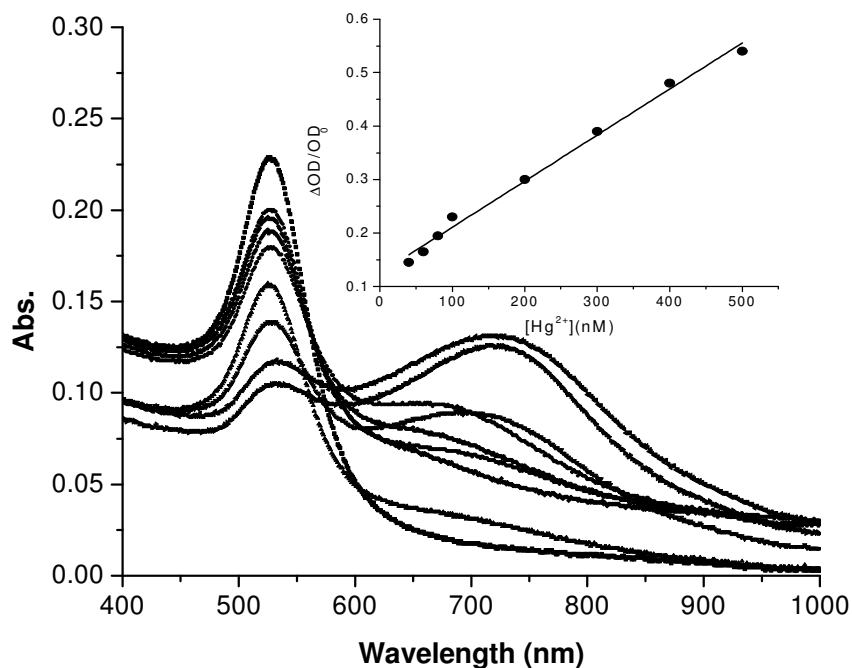


Figure 3.13 Absorption spectra of Au nanoparticle solution in presence of (a) 0 (b) 100 (c) 200 (d) 300 (e) 400 and (f) 500nM Hg^{2+} ion. (Inset: Calibration plot of Hg^{2+} ion concentration.)

3.4.2 Effect of pH

The pH of the reaction medium was found to significantly influence the detection efficiency of the system. In order to determine the effect of pH variation, the reaction was carried out under different pH values- 3.0, 4.5, 6.0, 8.0, 10.0 and 11.0. It was observed that while acidic pH (3.0, 4.5 and 6.0) and pH 8.0 did not induce any change in the SPR band of Au NPs, alkaline pH (10.0 and 11.0) were found to produce significant decrease in the SPR band intensity on addition of Hg^{2+} ions while keeping all other reaction conditions same. This is probably because highly alkaline conditions favor displacement of the PVP molecules from the surface of Au NPs. In the process, carbonyl groups of the lactam rings of PVP, that were earlier interacting with the Au metal atoms, get exposed and instead bind with the Hg^{2+}

ions present in the solution. This results in a drastic change in the external environment of the NPs, which gets manifested as a decrease in the band intensity (fig. 3.14)

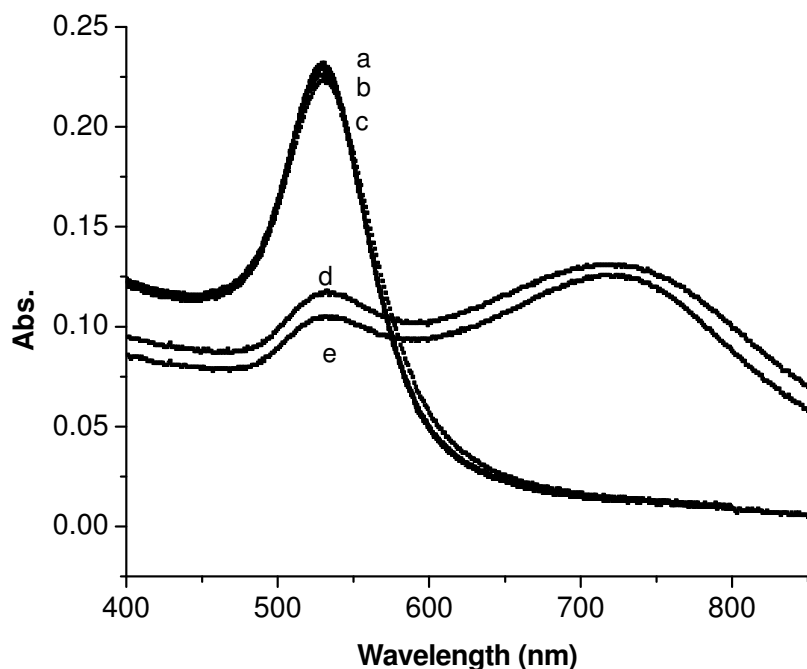


Figure 3.14 Absorption spectra of Au nps-500nM Hg²⁺ reaction mixture at pH (a) 3.0 (b) 6.0 (c) 8.0 (d) 10.0 and (e) 11.0

3.4.3. Effect of PVP concentration

The effect of stabilizer concentration on the detection efficiency of the sensor system was also investigated. It was observed that high concentrations of PVP reduced the sensitivity of the Au NPs towards Hg ions, which was manifested in a marginal change in LSPR band intensity on addition of Hg ions to the Au NPs [fig 3.15]. High concentrations of PVP probably led to complete encapsulation of the Au NPs within the polymer shell, thereby inhibiting any changes in the LSPR of nanoparticles that might be induced in presence of Hg ions. The selective interaction of PVP molecules with Hg ions, which is responsible for inducing the LSPR changes in Au NPs, is rendered insignificant under very high

concentrations of the stabilizer. Hence, PVP concentration was optimized at 0.05% (w/v), which was sufficient not only to provide stability to the Au NPs but also induced maximum shifts in LSPR band intensity of Au NPs on addition of the analyte.

3.4.4. Effect of PVP molecular weight

The stabilizer molecular weight was also found to play a crucial role in determining the sensor efficiency. Au NPs synthesized in higher molecular weight PVPs (160kDa and 360kDa) as stabilizers were observed to have a lower sensitivity towards the same analyte concentration as compared to Au NPs synthesized using PVP of molecular weight 40kDa as the stabilizer [fig. 3.15 inset]. This can be attributed to the fact that higher molecular weight PVPs have longer polymeric chains which wrap around the Au NPs in a more effective manner and thereby make the local environment of the nanoparticles less susceptible to any changes in LSPR characteristics that might be induced in presence of Hg^{2+} ions. Hence, for all our estimation purposes, PVP of molecular weight 40kDa was used as the stabilizer since it was found to least interfere in the detection process, while at the same time provide sufficient stability to the nanoparticle system.

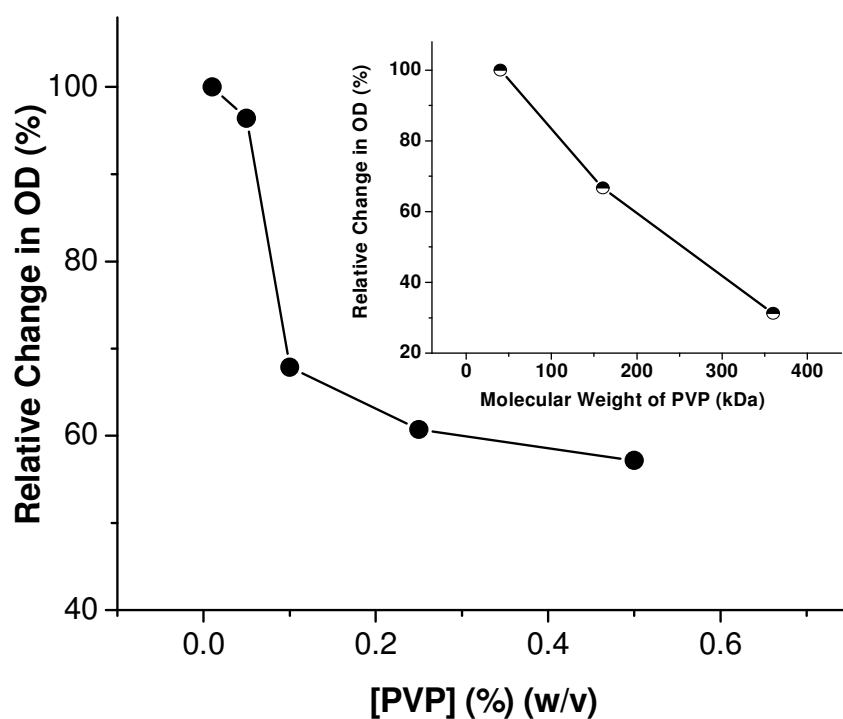


Figure 3.15 Relative change (%) in OD of reaction mixture containing PVP-Au-NPs and 500nM Hg^{2+} ions as a function of PVP % (w/v) (Inset: Relative change (%) in OD of reaction mixture containing PVP-Au-NPs and 500nM Hg^{2+} ions as a function of PVP molecular weight).

3.4.5. Interference study and selectivity

One of the primary factors deciding the efficiency of any sensor system is its selectivity and the extent to which it remains free from interference due to the presence of additional species in the analyte mixture. We checked for the interference of other metal ions in the detection system by subjecting different metal ions such as Ca^{2+} , Cu^{2+} , Cd^{2+} and Fe^{2+} to the same estimation protocol individually as well as in combination. 500nM solutions of each of the metal ions were prepared and added to the PVP-Au NP system. While Ca^{2+} , Cu^{2+} and Fe^{2+} showed no change in the LSPR band of Au NPs, addition of Cd^{2+} resulted in a slight decrease in intensity, but no shift in peak position or change in colour was observed. Addition

of a mixture of all the ions (final concentration of each being 500nM) to the Au NP system yielded a similar negligible decrease in band intensity (fig. 3.17). This can be explained based on the fact that Cd^{2+} is a relatively soft base compared to the other metal ions, though comparatively harder than Hg^{2+} , and therefore can complex to some extent with PVP resulting in a minute decrease in LSPR band intensity. However, the effect is visible only at Cd^{2+} concentration as high as 500nM, which is the upper detection limit of our AuPVP based estimation technique.

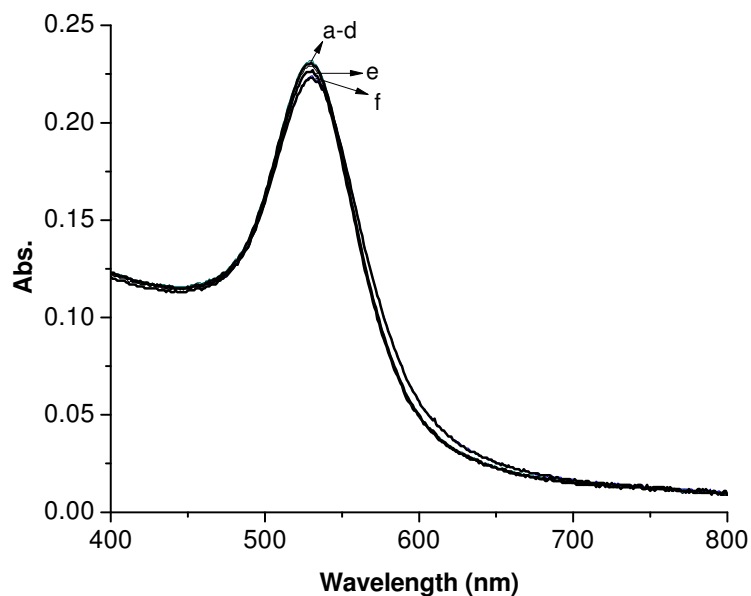


Figure 3.16 Interference study: Absorption spectra of Au nps in (a) absence of metal ions (b) 500nM Ca^{2+} (c) 500nM Cu^{2+} (d) 500nM Fe^{2+} (e) 500nM Cd^{2+} and (f) mixture of ions (500nM each)

3.5. Conclusions

The chapter describes the green synthesis of PVP capped Au nanoparticles via a clean, environment friendly gamma radiolytic route. The fabricated PVP-Au NPs were characterized by uv-visible spectroscopy and TEM techniques. Various experimental parameters were optimized to obtain Au NPs of desired morphology. The sensing properties

of the PVP-Au NPs were investigated for two biologically relevant species, namely hydrogen peroxide and Hg^{2+} in aqueous solutions. A colorimetric method based on interaction of the oxidation product of o-PDA with radiolytically synthesized Au nanoparticles was developed for estimation of H_2O_2 . H_2O_2 in the concentration range of $1 \times 10^{-7} \text{ mol dm}^{-3}$ to $2 \times 10^{-4} \text{ mol dm}^{-3}$ can be estimated by this method by suitably tuning the reaction parameters. The detection limit for the proposed method was determined to be $1 \times 10^{-7} \text{ mol. dm}^{-3}$. The estimation of H_2O_2 using this particular system was found to be independent of the molecular weight of PVP. The PVP-Au-NPs system was also successfully employed as a highly sensitive and selective LSPR based optical sensor for estimation of nanomolar concentrations of Hg^{2+} ions in aqueous solutions. Parameters, such as pH of solution, molecular weight and concentration of stabilizer were found to influence the detection efficiency of the system. The system showed optimum efficiency under the reaction conditions: $\text{pH} > 10.0$ and 0.1% PVP (40kDa) as the stabilizer for Au-NPs. The presence of different metal ions, such as Ca^{2+} , Cu^{2+} , Cd^{2+} and Fe^{2+} did not interfere with the detection efficiency of the system within its detection range of 0-500nM Hg^{2+} ion concentration. The LSPR based optical sensor system offers an easy, convenient and sensitive technique for estimation of Hg^{2+} ions in aqueous solutions, which has potential environmental applications.

Chapter 4: A comparative study of the synthesis of Poly(n-vinyl-2-pyrrolidone) capped Ag nanoparticles by different radiation sources: application for estimation of uric acid

4.1. Introduction

The formation of metallic nanoparticles in solution initiated by γ -ray [146,147], electron beam [148,149] and X-ray [150-157] irradiation has been proved to be an alternative route for obtaining dispersed nanoparticles. Though irradiation using high energy radiation sources like gamma and electron beam is a well established technique, synchrotron radiation X-rays as an ionizing radiation source have been little explored for fabrication of metal nanoparticles. The possibility of synchrotron X-ray source for the direct reduction of gold precursor solutions was first explored by Rosenberg and co-workers [158]. The high flux and high energy of synchrotron X-rays can be utilized for reduction of metal ion precursor to generate metal nanoparticles in solution. The interaction of X-rays with aqueous medium is similar to that of γ -rays. The primary radicals generated via radiolysis of water by X-rays are e_{aq}^- , $H\cdot$ and $\cdot OH$. The first two are reducing in nature while $\cdot OH$ is an oxidizing radical. X-ray irradiation method too offers the advantages of being a clean reaction system devoid of chemical reducing agents, better control over reaction parameters, rapid synthesis and high reduction yields due to the high X-ray flux.

In recent years, the use of metal nanoparticles as analytical and bioanalytical sensors has been receiving significant attention because of their unusual optical, electronic, and chemical properties [159-161]. Large numbers of methods have been developed for the fabrication of metal nanoparticles. However, the major disadvantages in most of the methods include use of toxic reducing chemicals, poor nanoparticle size distribution, and the poor dispersion of the nanoparticles in the polymer host [162]. Radiolytic methods, thus, have

emerged as an efficient alternative technique for fast and one step synthesis of uniformly dispersed metal nanoparticles [112-114]. The reducing radicals generated in-situ during radiolysis of water, such as e_{aq}^- and $H\cdot$, are utilized to reduce metal ion precursors to metal in zero valent state. These metal atoms coalesce to form metal nanoparticles in presence of a capping agent. These nanoparticles can therefore be effectively employed as biosensors with minimum probability of interference from external additives. The use of a biocompatible polymer like Poly (N-vinyl-2-pyrrolidone) (PVP) as the capping agent [163,164] further enhances their viability to detect biologically relevant molecules without disturbing the natural environment of the biological samples in which the estimation is usually done.

Localized surface Plasmon Resonance (LSPR)-based optical chemical sensors and biosensors are an appropriate, simplified, cheap and rapid alternative to more sophisticated detection techniques. The LSPR wavelength is extremely sensitive to the local environment around the nanoparticles, which facilitates their use as sensing devices [165]. In particular, this property can be utilized for highly sensitive detection of target molecules in medical applications. One such important application of nanoparticles has been made for the estimation of a biologically relevant molecule Uric acid. Uric acid represents the major catabolite of purine breakdown in humans. The normal concentration of uric acid in blood samples is reported to be in the range 150–420 μ M [166]. High levels of uric acid in the blood (hyperuricemia or Lesch-Nyhan syndrome) are linked with gout and other conditions including increased alcohol consumption, obesity, diabetes, high cholesterol, high blood pressure, kidney disease, and heart disease [167,168]. On the other hand, abnormally low uric acid levels are symptoms of diseases, such as multiple sclerosis [166]. Hence estimation of uric acid in blood can be used as a diagnostic tool for monitoring a large number of diseases. Furthermore, uric acid is an antioxidant in human adult plasma and is involved in various pathological changes [169]. In view of this, numerous techniques have been developed over

the years for detection and estimation of uric acid levels, which include enzymatic methods [170], spectrophotometry [171,172] electroanalysis [173], high performance liquid chromatography [174], fluorimetry [175,176] and chemiluminescence [177]. However, most of these methods suffer from limitations in terms of detection limits, temperature constraints or requirement of additional reagents. Radiolytically synthesized metal nanoparticles based sensors offer a simple, attractive and low cost alternative to these conventional estimation techniques.

The chapter highlights the synthesis of silver nanoparticles (Ag NPs) using high energy radiation sources, namely synchrotron X-ray, γ - ray and electron beam (EB) in presence of PVP as a stabilizing agent. The silver nanoparticles formed were characterized by UV-visible spectroscopy and TEM analysis. Effect of various reaction parameters, such as radiation dose, dose rate, concentration and molecular weight of the stabilizer and precursor ion concentration, on the morphology of the nanoparticles was also investigated. Ag NPs fabricated via gamma irradiation technique were subsequently employed as a LSPR based optical sensor system for estimation of uric acid. The technique is based on the catalytic oxidation of silver nanoparticles by hydrogen peroxide, which is generated in-situ during enzymatic degradation of uric acid in presence of enzyme uricase [178-182]. The method was successfully employed for estimation of uric acid concentration in bovine and human serum samples.

4.2. Results and discussion

4.2.1. Synthesis of polymer capped Ag nanoparticles by gamma, electron beam and synchrotron radiation sources and their characterization

The interaction of ionizing radiation, such as γ -ray, X-ray and accelerated electron beam with aqueous solution is fully understood and well established. Water, being the major

component of an aqueous solution, absorbs most of the radiation energy and undergoes radiolysis. The radiolytic transient species formed, namely hydrated electron (e_{aq}^-), hydrogen atom radical (H^\cdot) and hydroxyl radical ($\cdot OH$) are highly reactive in nature. e_{aq}^- and H^\cdot possess high reduction potentials and can reduce metal ions to lower valences or to atoms in the zero valent state. These metal atoms subsequently coalesce to form metal nanoparticles in presence of a capping agent, such as polymers, ligands, surfactants etc. The $\cdot OH$ radical, being oxidizing in nature can oxidize the metal atoms back to ions. Therefore, isopropyl alcohol is added to the system to scavenge the $\cdot OH$ radicals. Isopropyl alcohol reacts with $\cdot OH$ radical to generate isopropyl radical, which is mildly reducing in nature and capable of reducing Ag^+ as well. Thus, the overall atmosphere is turned into a reducing one by the addition of isopropyl alcohol to the system.

Briefly, an aqueous solution containing $2 \times 10^{-4} \text{ mol.dm}^{-3} Ag^+$, 0.5% PVP (w/v) ($M_w = 40,000 \text{ Da}$), $2 \times 10^{-1} \text{ mol.dm}^{-3}$ isopropanol was irradiated by exposing the solution to X-ray beam for an absorbed dose of 2 kGy (time of irradiation=63s). The formation of Ag NPs was indicated by development of yellow color in the solution. The Ag NPs formed were characterized by measuring their UV-visible spectra after appropriate dilution. Fig. 4.1 presents the evolution of the LSPR band of Ag NPs with increasing duration of irradiation. The yield of Ag NPs formed increased with the increase in radiation dose, manifested by an increase in intensity of the LSPR band. The absorption maxima (γ_{max}) was centred at $\sim 411 \text{ nm}$ and the saturation dose required to achieve near complete reduction of $2 \times 10^{-4} \text{ mol.dm}^{-3} Ag^+$ in aqueous PVP solution was estimated to be 2kGy (irradiation time=63s).

The Ag NPs formed were further characterized by TEM analysis. Fig.4.2 highlights the TEM image of Ag NPs prepared by X-ray irradiation. The particles were observed to have a broad size distribution with average size in the range 10-15nm.

The precursor solutions for γ and EB-irradiations were maintained at the same concentration; however, prior to γ -radiation, the precursor solution was deaerated by N_2 purging. The UV-visible spectra of Ag NPs fabricated via gamma irradiation under similar experimental conditions are presented in Fig. 4.3. The saturation dose was determined to be 1.7 kGy, which is close to that obtained in X-ray irradiation method. The yield of the Ag NPs, manifested by the intensity of characteristic LSPR band of Ag NPs, increased with increase in absorbed radiation dose till all precursor Ag^I ions were exhausted. However, the LSPR peak in this case was observed to be narrower with γ_{max} at ~ 401 nm. This indicated formation of smaller sized particles with narrow size distribution in case of γ -radiolysis, compared to those obtained by X-ray radiolysis. This observation was further substantiated by the TEM analysis of Ag NPs synthesized by γ -irradiation. Fig. 4.4 shows the TEM image of the freshly prepared PVP-capped-Ag nanoparticles. Ag NPs formed in PVP are mainly spherical in nature and exhibit narrow size distribution with average particle size in the range of 8-10 nm. Particle size analysis also revealed the particles obtained by radiolytic process to be of uniform size distribution with average hydrodynamic diameter of around 11nm. Fig. 4.16a represents the AFM image of the PVP-capped-Ag nanoparticles, which also verifies the spherical nature of the nanoparticles generated. The results obtained in case of EB irradiation method were observed to be similar to those obtained in the case of γ -irradiation.

The smaller size of Ag NPs obtained via gamma irradiation method can be attributed to the isotropic irradiation offered by the cylindrical design of the gamma chamber, which leads to uniform irradiation of the precursor solution. This results in the formation of a large number of seeds at any given instant, thereby limiting the precursor ion supply and subsequently restricting the growth of the nuclei to yield small, uniform sized particles. A similar trend is observed in case of EB irradiation technique. However, in the case of X-ray irradiation, the linear geometry of the beam and its restricted size leads to non homogeneous

energy deposition along the beam-solution interception. This culminates in an inhomogeneous rate of precursor ion reduction along the beam. Thus, the quantity of seeds formed in this irradiation method is substantially lower, resulting in the formation of larger sized particles

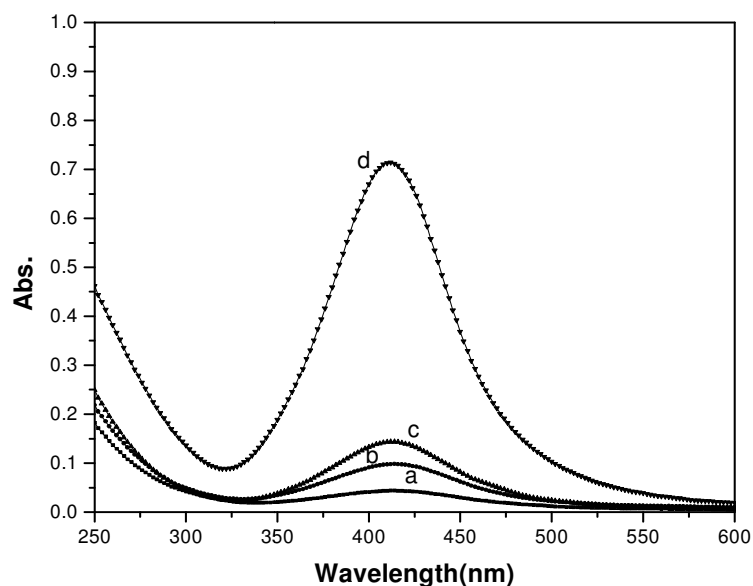


Fig. 4.1 Absorption spectra of aqueous Ag nanoparticles in PVP prepared by X-ray irradiation for different irradiation time: (a) 12s, (b) 23sec, (c) 41s, (d) 63s; $[Ag^+]=2 \times 10^{-4} \text{ mol.dm}^{-3}$, $[PVP]=0.5\%$, $[Isopropanol]=2 \times 10^{-1} \text{ mol.dm}^{-3}$, dose rate= 113.7 kGy.h^{-1} .

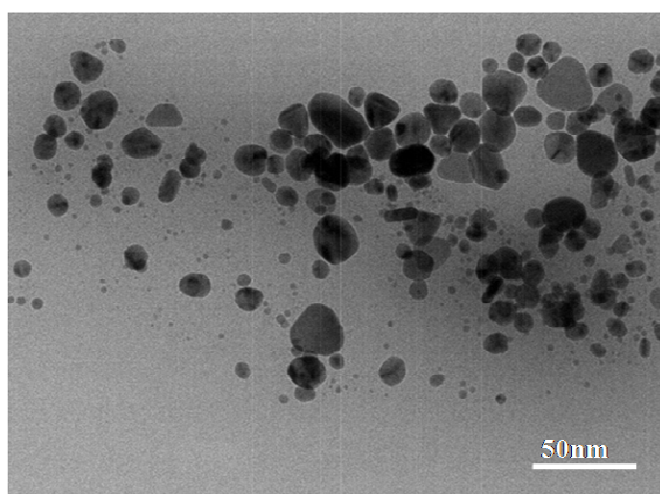


Fig. 4.2 TEM image of Ag nanoparticles in PVP prepared by X-ray irradiation

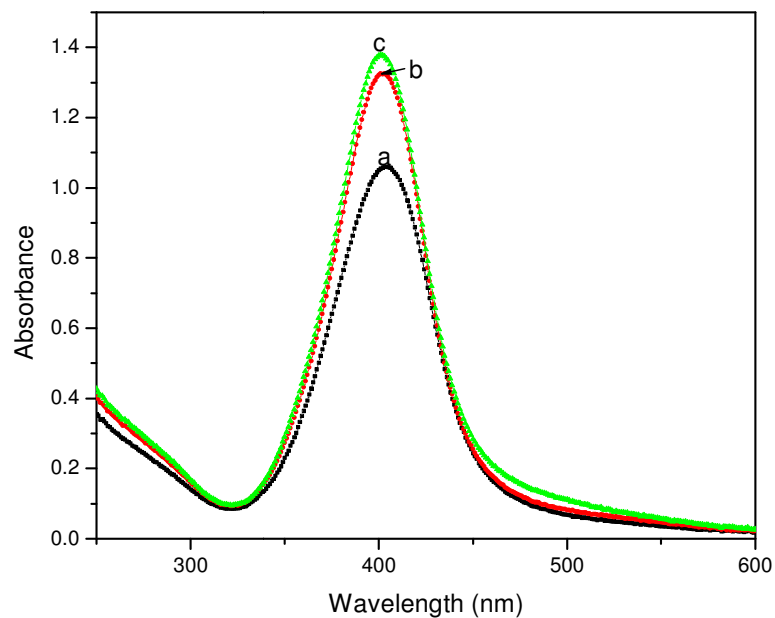


Fig. 4.3 Absorption spectra of aqueous Ag nanoparticles in PVP prepared by γ -irradiation for different absorption dose: (a) 1kGy, (b) 1.3kGy, (c) 1.6kGy; $[Ag^+]=2 \times 10^{-4} \text{ mol.dm}^{-3}$, $[PVP]=0.5\%$, $[Isopropanol]=2 \times 10^{-1} \text{ mol.dm}^{-3}$, dose rate= 4.0 kGy.h^{-1}

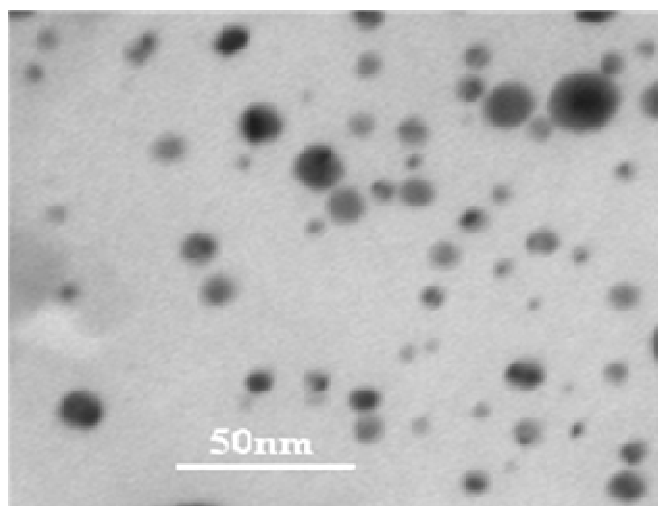


Fig. 4.4 TEM image of Ag nanoparticles in PVP prepared by γ -irradiation

4.2.2. Effect of variation of precursor ion concentration

Fig. 4.5, Fig. 4.6 and Fig. 4.7 present the UV-visible spectra of Ag NPs, synthesized by X-ray, γ -ray and EB irradiation methods respectively, for Ag^+ concentration variation within the range of $1 \times 10^{-4} \text{ mol.dm}^{-3}$ to $4 \times 10^{-4} \text{ mol.dm}^{-3}$. The concentrations of all other reactants were kept undisturbed. The λ_{max} was observed to be red shifted with increase in Ag^+ concentration in case of X-ray (Fig. 4.5) and γ -irradiation (Fig. 4.6) methods, whereas it underwent a blue shift in case of EB-irradiation method (Fig. 4.7). This implied that the Ag NPs size increased with increase in Ag^+ concentration in case of X-ray and γ -irradiation, whereas it decreased in the case of EB irradiation. The increase in particle size at higher precursor concentration has been reported earlier. However, decrease in size in case of EB-irradiation method can be explained on the basis of the very high dose rates delivered by E-beam. This results in the formation of a large number of nuclei within a short time span. With limited precursor ion concentration, the size of the clusters formed also gets restricted, resulting in the formation of smaller sized particles.

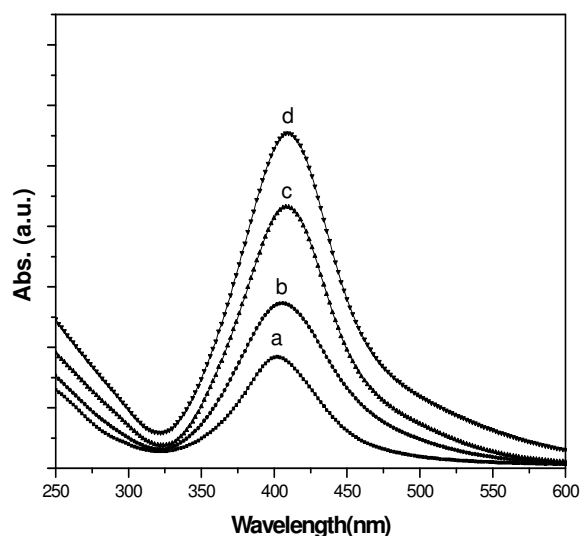


Fig. 4.5 Absorption spectra of aqueous Ag nanoparticles in PVP prepared by X-ray irradiation for different Ag^+ concentration: (a) $1 \times 10^{-4} \text{ mol.dm}^{-3}$, (b) $2 \times 10^{-4} \text{ mol.dm}^{-3}$, (c) $3 \times 10^{-4} \text{ mol.dm}^{-3}$, (d) $4 \times 10^{-4} \text{ mol.dm}^{-3}$; dose = 1.0kGy, 2.0kGy, 3.0kGy, 4.0kGy respectively; [PVP]= 0.5%, [Isopropanol]= $2 \times 10^{-1} \text{ mol.dm}^{-3}$, dose rate= 113.7 kGy.h^{-1}

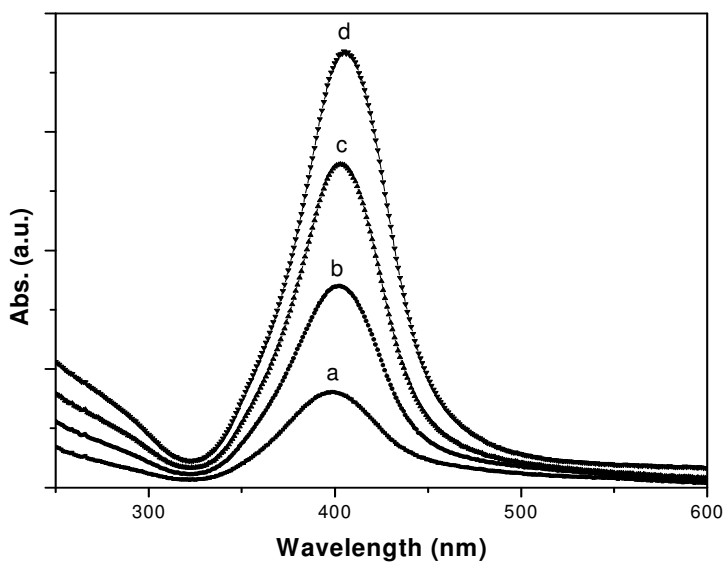


Fig. 4.6 Absorption spectra of aqueous Ag nanoparticles in PVP prepared by γ -irradiation for different Ag^+ concentration: (a) $1 \times 10^{-4} \text{ mol.dm}^{-3}$, (b) $2 \times 10^{-4} \text{ mol.dm}^{-3}$, (c) $3 \times 10^{-4} \text{ mol.dm}^{-3}$, (d) $4 \times 10^{-4} \text{ mol.dm}^{-3}$; dose=1.0kGy, 2.0kGy, 3.0kGy, 4.0kGy respectively; [PVP]= 0.5%, [Isopropanol]= $2 \times 10^{-1} \text{ mol.dm}^{-3}$, dose rate= 4.0 kGy.h^{-1}

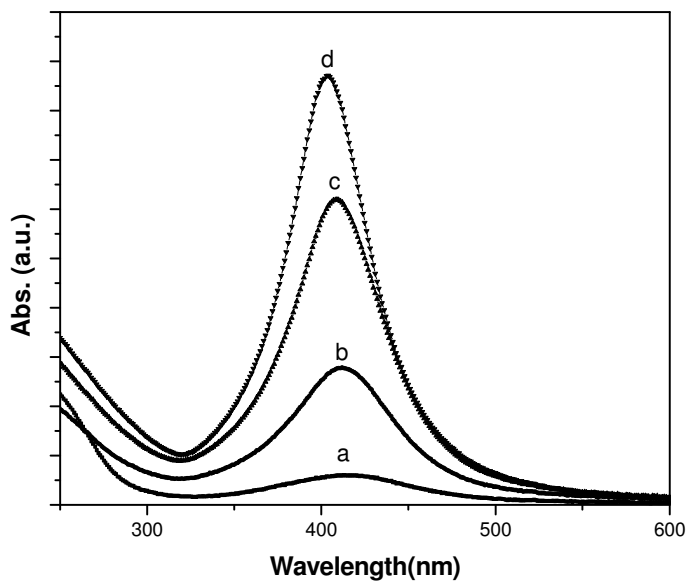


Fig. 4.7 Absorption spectra of aqueous Ag nanoparticles in PVP prepared by EB- irradiation for different Ag^+ concentration: (a) $1 \times 10^{-4} \text{ mol.dm}^{-3}$, (b) $2 \times 10^{-4} \text{ mol.dm}^{-3}$, (c) $3 \times 10^{-4} \text{ mol.dm}^{-3}$, (d) $4 \times 10^{-4} \text{ mol.dm}^{-3}$; dose=1.0kGy, 2.0kGy, 3.0kGy, 4.0kGy respectively; [PVP]= 0.5%, [Isopropanol]= $2 \times 10^{-1} \text{ mol.dm}^{-3}$, dose rate= 2.0 kGy/pass

4.2.3. Effect of PVP concentration

In order to investigate the role of PVP in stabilization of Ag NPs, the Ag NPs were synthesized with different concentrations of PVP as stabilizers. The PVP concentration was varied from 0.1% to 2% (w/v) in X-ray, γ -ray and EB irradiation methods, results are shown in Fig. 4.8, Fig. 4.9 and Fig. 4.10 respectively. The concentrations of all other reactants were kept identical. There was no appreciable shift observed in the λ_{\max} position with increase in PVP concentration in case of X-ray (Fig. 4.8) and γ -ray irradiation methods (Fig. 4.9), whereas it was red shifted in EB-irradiation method (Fig. 4.10). This inferred a marginal increase in average particle size at higher PVP concentrations in case of EB-irradiation method. However, in all the three cases, the FWHM decreased with increase in PVP concentration, which implied formation of Ag NPs with narrow size distribution at higher PVP concentrations in all three cases.

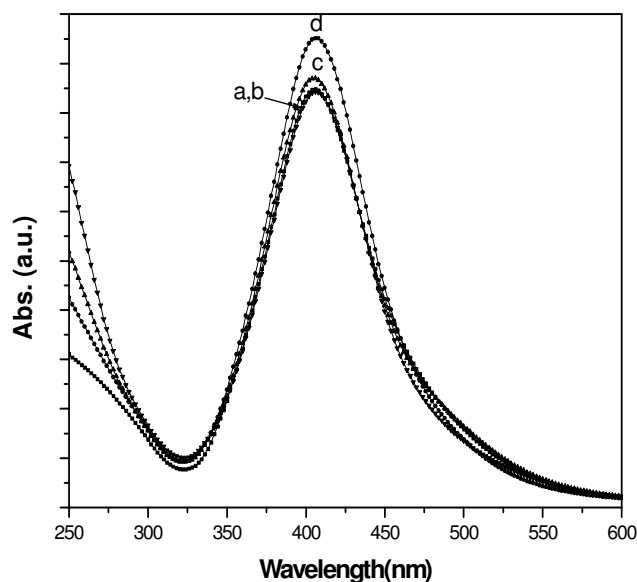


Fig. 4.8 Absorption spectra of aqueous Ag nanoparticles in PVP prepared by X-ray irradiation for different PVP concentration: (a) 0.1%, (b) 0.5%, (c) 1%, (d) 2% (w/v); $[Ag^+]=2 \times 10^{-4}$ mol. dm^{-3} , $[Isopropanol]= 2 \times 10^{-1}$ mol. dm^{-3} , dose= 2.0kGy, dose rate= 113.7kGy. h^{-1}

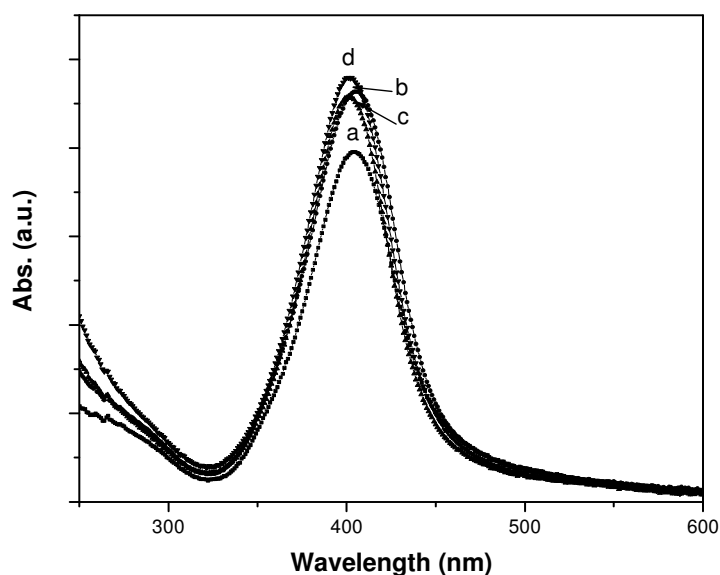


Fig. 4.9 Absorption spectra of aqueous Ag nanoparticles in PVP prepared by γ -irradiation for different PVP concentration: (a) 0.1%, (b) 0.5%, (c) 1%, (d) 2% (w/v); $[Ag^+]=2 \times 10^{-4}$ mol.dm $^{-3}$, [Isopropanol]= 2×10^{-1} mol.dm $^{-3}$, dose=2.0kGy, dose rate= 4.0kGy.h $^{-1}$

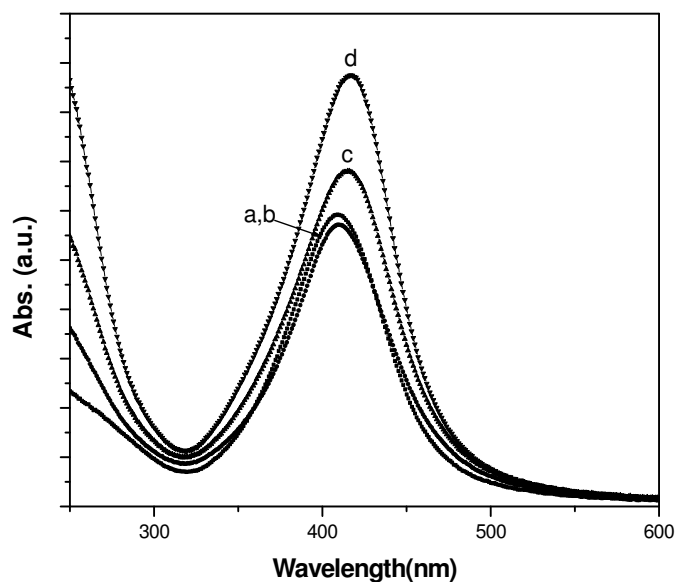


Fig. 4.10 Absorption spectra of aqueous Ag nanoparticles in PVP prepared by EB-irradiation for different PVP concentration: (a) 0.1%, (b) 0.5%, (c) 1%, (d) 2% (w/v); $[Ag^+]=2 \times 10^{-4}$ mol.dm $^{-3}$, [Isopropanol]= 2×10^{-1} mol.dm $^{-3}$, dose=2.0kGy, dose rate= 2.0 kGy/pass

4.2.4. Effect of dose rate on nanoparticle formation in EB-irradiation

The effect of variation of dose rate on the NPs morphology was studied in case of EB-irradiation method by irradiating the precursor solution under two dose rate conditions, i.e., 2.0 kGy/pass and 1.0 kGy/pass. The absorption spectra of Ag NPs solution at the two dose rates are shown in Fig. 4.11. There was no shift in peak position with change in dose rate. In other words, the size of NPs produced was independent of the dose rate in case of EB-irradiation method under high dose rate conditions.

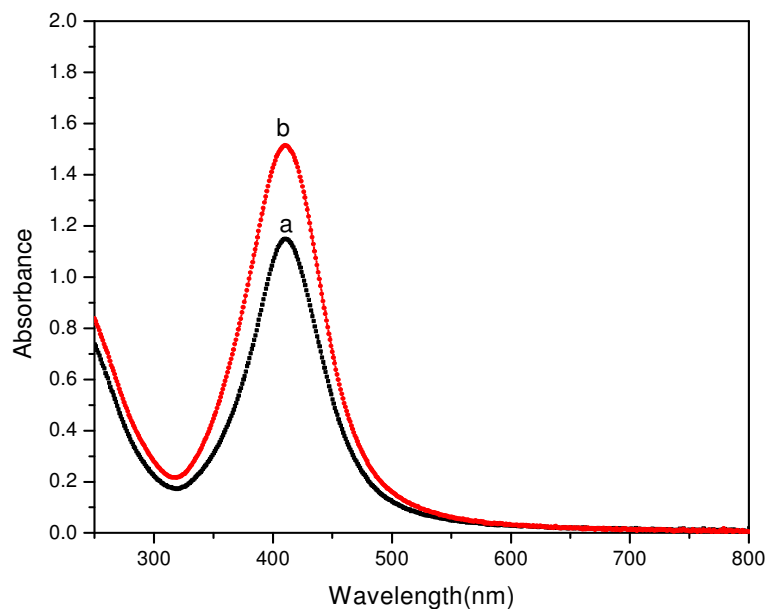


Fig. 4.11 Absorption spectra of aqueous Ag nanoparticles in PVP prepared by EB-irradiation for different absorption dose rates: (a) 2.0 kGy/pass, (b) 1.0 kGy/pass; $[Ag^+] = 2 \times 10^{-4} \text{ mol.dm}^{-3}$, $[PVP] = 0.5\%$, $[Isopropanol] = 2 \times 10^{-1} \text{ mol.dm}^{-3}$

4.2.5. Estimation of uric acid

Uric acid undergoes enzymatic degradation in presence of enzyme Uricase under optimum assay conditions of 37°C and pH 7.4 (Fig. 4.12). This pH is also relevant because it represents the physiological pH of biological fluids, i.e., urine or blood serum. Hydrogen

peroxide is generated as one of the reaction products, which is known to be a strong oxidizing agent. This, in turn, causes oxidation of silver nanoparticles resulting in a decrease in intensity of the LSPR band.

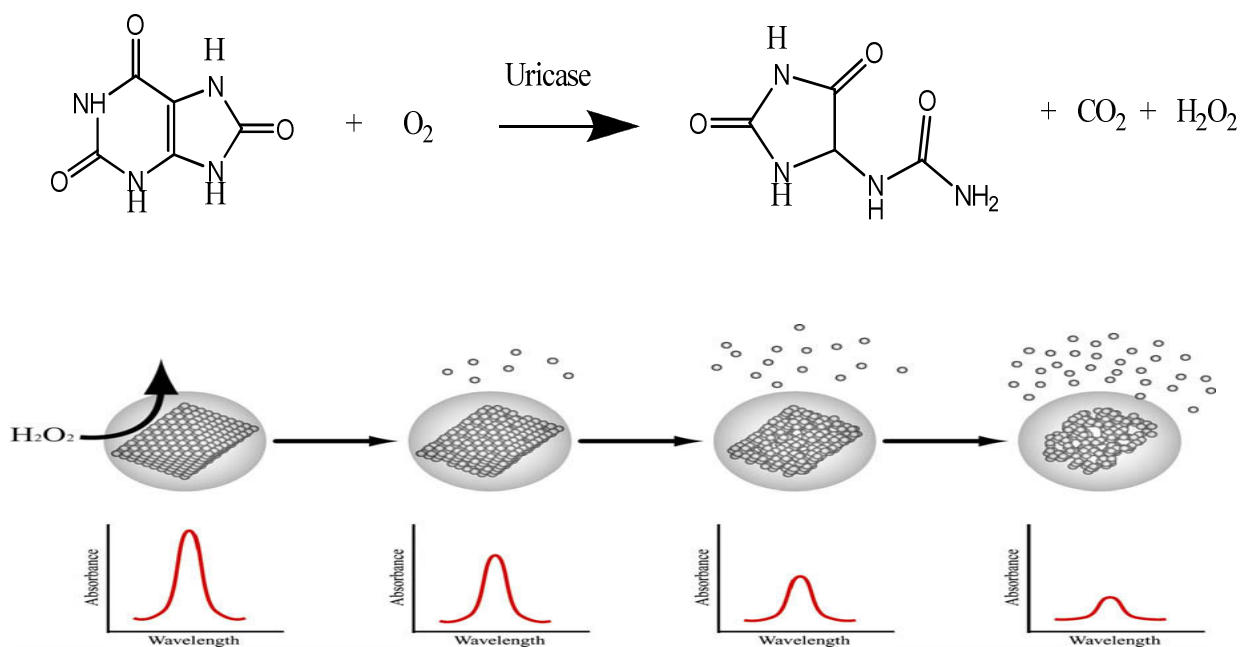


Fig. 4.12 Enzymatic degradation of uric acid in presence of Uricase.

Fig. 4.13 shows the changes in the LSPR optical characteristics of Silver nanoparticles with time due to introduction of uric acid and uricase into the system. It was observed that with increasing time, the bright yellow color of silver nanoparticles gradually faded and the solution turned almost transparent. The relationship between absorbance strength change and time is illustrated in fig. 4.13 inset. In order to confirm that the LSPR absorbance change was caused only in the presence of uric acid, phosphate buffer and deionized water alone were separately introduced into the nanoparticle solution and the spectra monitored with time; no spectral change was observed in either case.

For the evaluation of Ag-PVP solution as a uric acid biosensor, different concentrations of uric acid (10 to 100 μM) were taken in 25mL conical flasks and 0.2 mL of 0.137mg/mL Uricase stock solution was added to each of them. The resultant mixtures were diluted to 6.25mL with 20mM phosphate buffer and incubated at 37⁰C for 20 minutes. The course of the enzymatic reaction was followed by monitoring the absorbance peak of uric acid at 293nm, whose intensity decreases with time (Fig. 4.14). Subsequently, 3.75mL of 4×10^{-4} mol dm^{-3} Ag nanoparticle solution (final concentration being 1.5×10^{-4} mol dm^{-3}) was added to each of the flasks and the mixtures allowed to stand at room temperature for another 60 minutes. The UV-Visible spectra were recorded thereafter in the wavelength range 250-650nm.

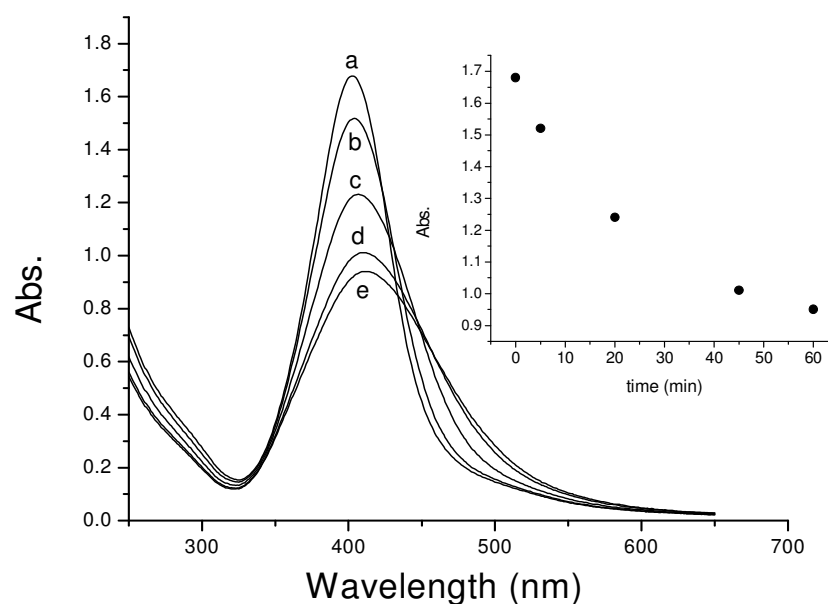


Fig. 4.13 Absorption spectra of 150 μM Ag nanoparticle solution in presence of 50 μM uric acid after (a) 0 min, (b) 5 min, (c) 20 min, (d) 45 min, (e) 60 min. Inset: absorbance strength of Ag nanoparticles solution containing uric acid as a function of time.

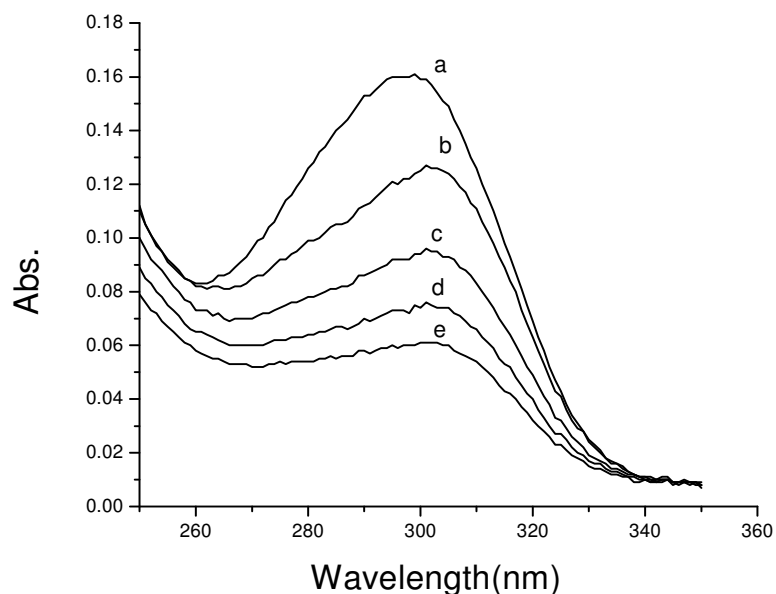


Fig. 4.14 Absorption spectra of uric acid solution in presence of Uricase after (a) 0 min, (b) 5 min, (c) 10 min, (d) 15 min, (e) 20 min

Fig. 4.15 shows the variation in UV-Visible spectra of the silver nanoparticles with increasing concentration of uric acid. It was observed that intensity of the LSPR band decreases gradually with increase in uric acid concentration. The decrease was accompanied by a slight red shift in the absorption maxima of the band, which is attributed to the partial oxidation of nano-Ag [183-186]. The shift in λ_{max} might also be due to the slight aggregation caused by the destruction of the PVP shell stabilizing the nanoparticles, followed by decrease in the distance between the nanoparticles [187]. This is evident from the TEM images of Ag-NPs recorded before and after addition of uric acid (fig. 4.16a and 4.16d). While the control (Ag-NPs) exhibited an average particle size of 5.1 ± 1.6 nm, those in presence of uric acid were found to have bigger particle size of 15.4 ± 4.6 nm. Particle size analyzer data also reveals an increase in average hydrodynamic diameter of the Ag nanoparticles after addition of $20\mu\text{M}$ uric acid in presence of uricase. AFM analysis was also carried out to study the effect of addition of uric acid-uricase system to the PVP-Ag-NPs. Fig. 4.17a and 4.17b present the AFM images of PVP-Ag-NPs before and after addition of uric acid-uricase

system. Introduction of uric acid and subsequent generation of hydrogen peroxide in the medium resulted in partial decomposition of the polymer layer leading to the aggregation of the Ag colloids, which is evident from bigger particle size and the blurring of the boundaries existing between the individual particles.

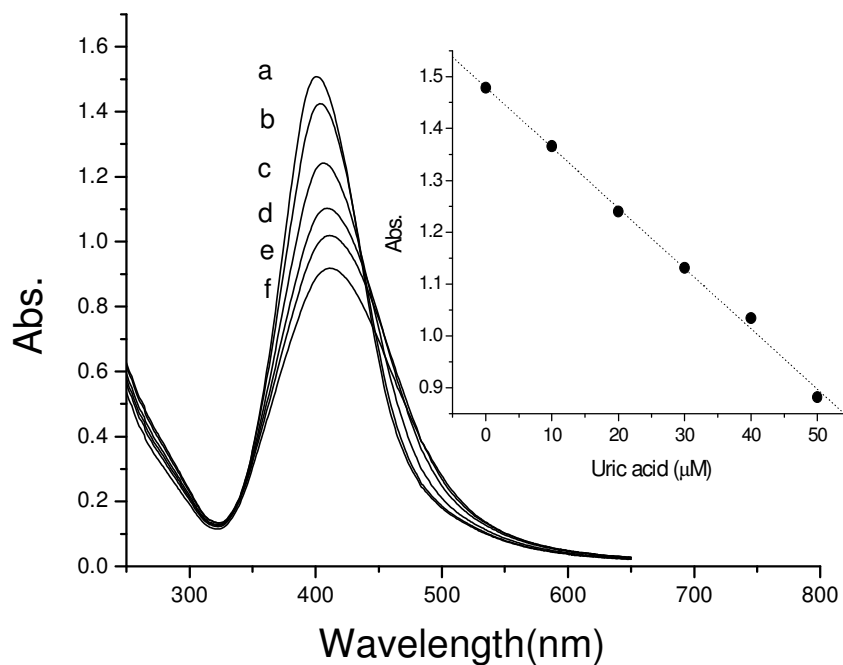


Fig. 4.15 Absorption spectra of Ag nanoparticle solution (PVP, Mol wt.= 40kD) in presence of different concentration of uric acid, after 60 min: (a) 0 μM, (b) 10 μM, (c) 20 μM, (d) 30 μM, (e) 40 μM, (f) 50 μM. Inset: Linear plot of absorbance of Ag nanoparticle vs uric acid concentration ($R^2=0.9964$), uric acid concentration range= 0 to 5×10^{-5} mol.dm⁻³.

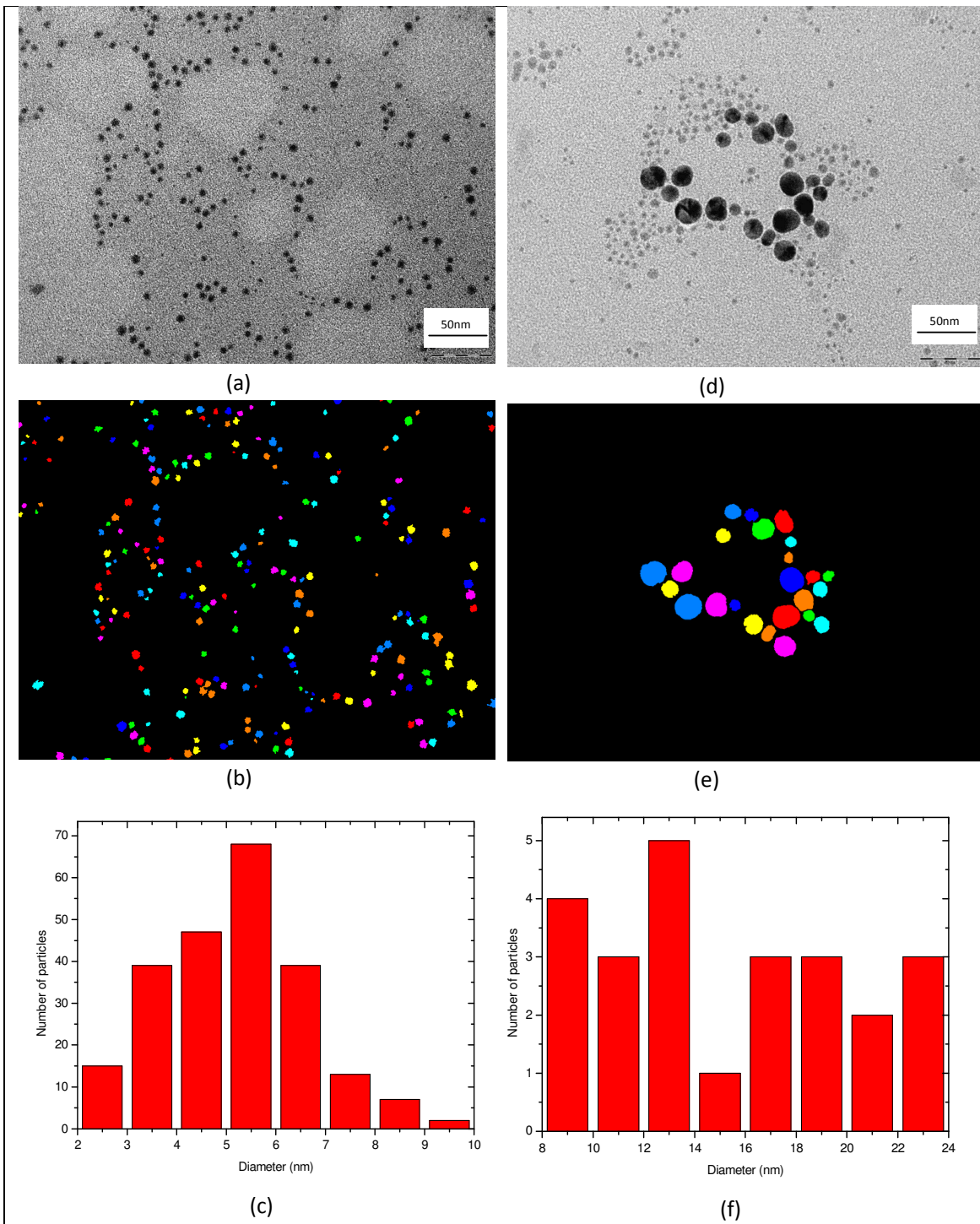


Fig. 4.16 TEM micrograph of Ag nanoparticles prepared using PVP of molecular weight 40kD (a) before addition of uric acid (b) after addition of uric acid

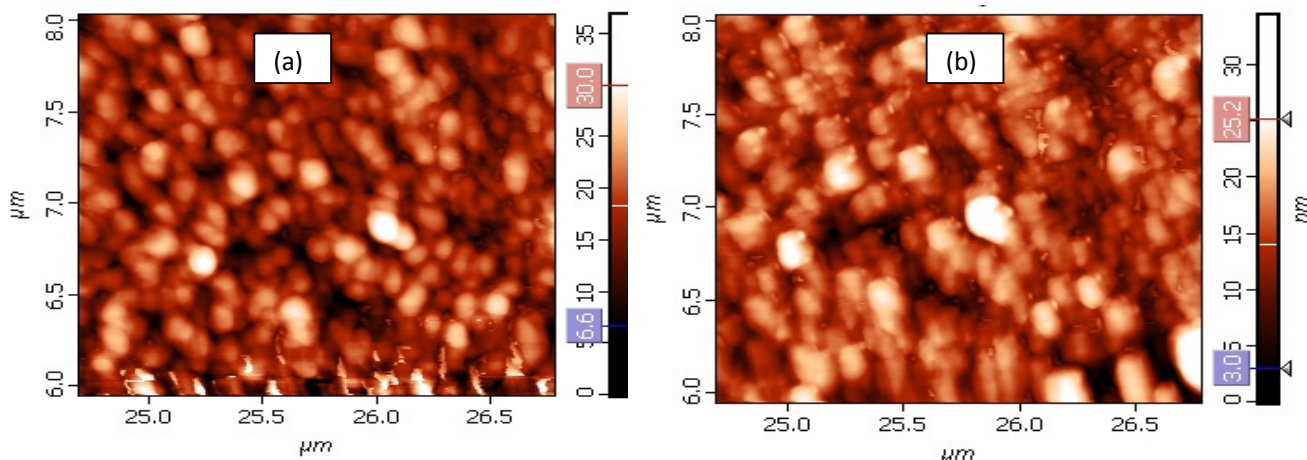


Fig. 4.17 AFM images of Ag nanoparticles prepared using PVP (Mol wt.= 40kD) (a) before addition of uric acid (b) after addition of uric acid

The PVP-Ag-NPs were further characterized by zeta potential measurement. The magnitude of the zeta potential gives an indication of the stability of the nanoparticle suspension system. If all the particles in suspension have a large negative or positive zeta potential, they tend to repel each other and there will be less tendency for the particles to come together to form agglomerates. Therefore, the decrease in the magnitude of zeta potential indicates the tendency of the particles to form agglomerates [188]. In addition, zeta potential also indicates the presence of an oxidized surface layer. Zeta potential measurements for the samples were therefore carried out to further confirm the partial oxidation of the silver nanoparticles by in situ generated hydrogen peroxide. The zeta potential for the control, i.e., PVP-Ag-NPs solution was found to be -29.6 mV at pH = 7.4 (Fig. 4.18 inset). However, with increase in uric acid concentration, the zeta potential values were found to become less negative. This is probably due to partial neutralization of the negative charge by Ag^+ ions generated via partial oxidation of Ag NP caused by H_2O_2 generated in situ in uric acid–uricase reaction system (Fig. 4.18). It has been well established that electrostatic stabilization of nanoparticles would typically require a zeta potential above

30 mV or below -30 mV [189]. Therefore, in the present study the values of zeta potentials suggested that the stability of the PVP-Ag-NPs suspension was based on steric stabilization by the PVP polymer. Unlike electrostatic stabilization, steric stabilization with nonionic polymers is independent of pH and electrolyte concentration. Accordingly, steric stabilization is useful for prevention of agglomeration of nanoparticles in physiological media.

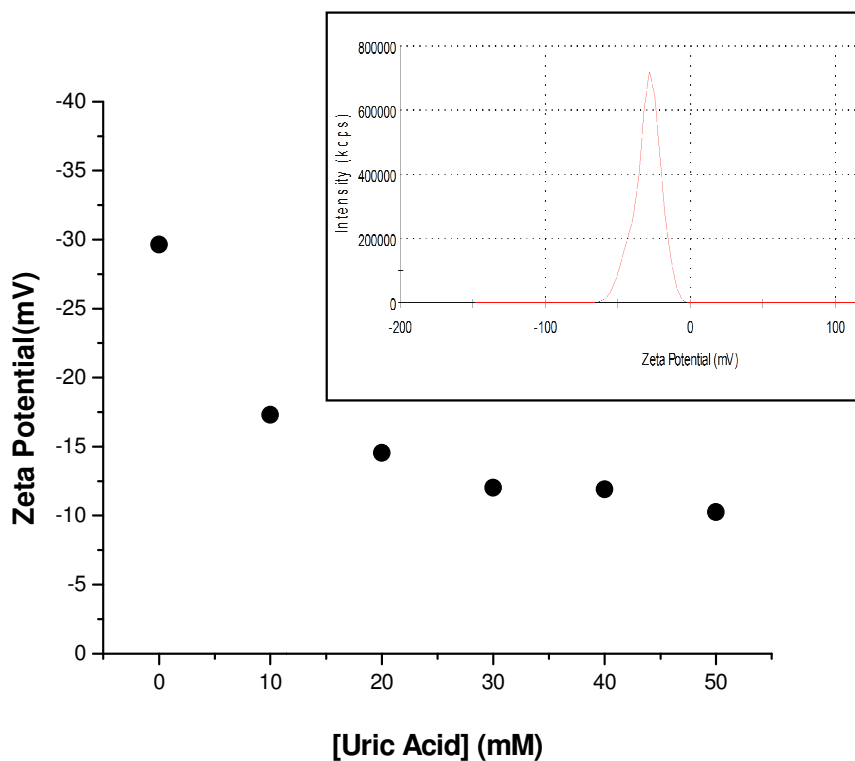


Fig. 4.18 Zeta potential of Ag nanoparticle as a function of uric acid. Inset: Zeta potential curve for Ag nanoparticle solution without uric acid.

4.2.6. Generation of calibration curve

The calibration curve for estimation of uric acid by PVP-Ag-NPs sensor system was established by plotting the absorbance (OD) of SPR band of Ag nanoparticles as a function of uric acid concentration (Fig. 4.15 inset). The response was found to be linear ($R^2 = 0.9964$) in the concentration range of 0 – $50\mu\text{M}$ uric acid and can be represented by Eq. (5)

$$\text{OD} = 1.480 - 0.012[\text{uric acid}] \quad (5)$$

The detection limit of the system was found to be 5 μ M of uric acid. The calibration curve was further used for the determination of unknown concentrations of uric acid in bovine and human serum samples.

4.2.7. Estimation of uric acid in bovine and human serum samples

The concentration of uric acid in serum samples is normally found in the micromolar range. Therefore, the method described earlier was effectively applied for determination of uric acid concentration in serum samples. To minimize interference from proteins present in the serum sample, 5mL of bovine serum sample was initially heated at 90⁰C to initiate denaturation of the proteins. After cooling down to room temperature, the resultant mixture was centrifuged at 4000rpm for 5 minutes to separate denatured proteins. The supernatant was removed and filtered using a 45micron syringe filter. The volume of the filtrate was made up to the original volume using 20mM phosphate buffer and divided in to two parts of 1 mL each. The first part of the filtrate was subjected to the uric acid estimation protocol using PVP-Ag biosensor system, as described earlier. The second part of the filtrate was diluted ten times and its UV-Visible spectrum was recorded for background correction of the SPR band of the sample. The same procedure was adopted in case of bovine serum sample. The concentrations of uric acid in both human and bovine serum samples were estimated from the calibration plot (Fig. 4.15 inset). The interference of ions, such as chlorides, sulphates, chlorides and sulphates in the uric acid estimation process may be ignored in this case where the silver nanoparticles have been sterically stabilized using PVP, as the effect of the ions on the LSPR band of Ag-NPs becomes prominent only in case of electrostatically stabilized systems, such as citrate stabilized Ag nanoparticles [190,191]. For comparison purpose, a commercial colorimetric uric acid assay kit (Quantichrom Uric Acid Assay Kit-DIUA-250) was used to estimate the uric acid in the samples under similar reaction

conditions. Table 4.1 presents the results obtained from the proposed PVP-Ag-NPs biosensor and those obtained from the comparison method for three different human serum samples (HS-1, HS-2 and HS-3). A one sample T-test was performed to test the null hypothesis and the results are presented in Table 4.1. The absolute values of the estimated t were lower than the critical t value ($\alpha= 0.05$, $df = 4$) of 2.776, which suggested that the results obtained using the pro-posed method, were not significantly different from those obtained by the comparison procedure at a 95% confidence level. A one-way ANOVA F-test was also performed on the results obtained from proposed method and comparison method for three human serum samples in order to check the null hypothesis (Table 4.1). In this case, $F_{crit}(1,4) = 7.71$ at $\alpha= 0.05$. The p and F values obtained from the ANOVA F-test were 0.97 and 0.001, respectively. Since $p > \alpha$ and $F < F_{crit}$, it can be concluded that the uric acid concentration estimated by our proposed method is not significantly different from that obtained with the comparison method at 95% level of significance. The concentration of uric acid in bovine serum sample was estimated to be $181 \pm 3.7\mu\text{M}$ (average \pm standard deviation) by using the proposed method. This was also found to be in reasonably good agreement with the measured value of $190\mu\text{M}$ determined using the commercial kit method.

Table 4.1 Determination of uric acid in human serum samples using proposed method and comparison method; results of one sample T-test and one way ANOVA F-test.

Sample (Human serum)	Uric acid concentration (μM)		One sample t-test $t(\alpha=0.05, n=5)$	One way ANOVA F-test	
	Other Method ^a	Proposed method ^b		p	F
HS-1	185	180 ± 4.4	-2.54	0.97	0.001
HS-2	153	149 ± 4.1	-2.18		
HS-3	243	248 ± 4.9	+2.28		

a. Other method: QuantiChrom Uric Acid Assay Kit (DIUA-250)

b. Average \pm standard deviation (for 5 determinations)

4.2.8. Effect of PVP molecular weight on sensor properties: Detection principle

The experiments discussed earlier had been carried out using silver nanoparticles synthesized using PVP of molecular weight 40kD as the capping agent. In order to study the effect of PVP molecular weight on the sensor properties of Ag nanoparticles, similar experiments were conducted using PVP of molecular weights 160kD and 360kD. For higher molecular weight PVPs, decrease in absorbance with increase in uric acid concentration was found to be very low for low uric acid concentrations, when the spectra were recorded after 60 min (Fig. 4.19). However, on recording the spectra again after 8 h, significant decrease in absorbance was observed for the system where PVP of molecular weight 160 kD was used as the capping agent (Fig. 4.20); though no change in spectral characteristics was observed after 8 h in case of PVP-Ag system with PVP of molecular weight 360 kD as the capping agent (data not shown). The calibration plots for PVP-Ag sensor systems with higher molecular weight PVP were found to exhibit poor linearity as compared to that with PVP of molecular weight 40 kD (Fig. 4.17 inset, Fig. 4.19 inset). R^2 values were found to be 0.9964, 0.8826 and 0.7730 for PVP with molecular weights 40 kD, 160 kD and 360 kD, respectively. This implies that the oxidation and degradation of silver nanoparticles became progressively slower when PVP of higher molecular weights was used as capping agents. High molecular weight PVPs (160 kD and 360 kD) have longer polymeric chains, which wrap around the Ag clusters and effectively shield them from external oxidizing agents. However, lower molecular weight PVP (40 kDa) has comparatively shorter polymeric chains and hence its ability to stabilize Ag clusters is also less. Therefore, Ag in such cases is more accessible to hydrogen peroxide, which causes significant oxidation of the Ag atoms present on the surface of the clusters, resulting in a decrease in the absorbance of the SPR band.

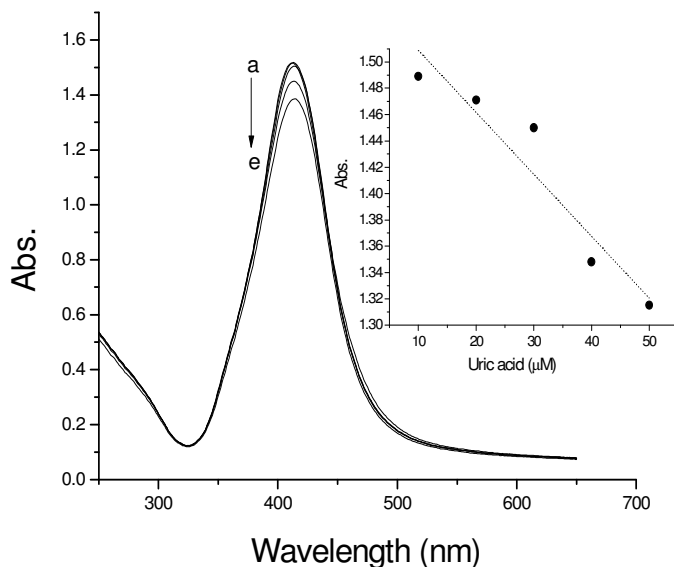


Fig. 4.19 Absorption spectra of Ag nanoparticle solution (PVP, Mol wt.= 160kD) in presence of different concentration of uric acid, after 60 min: (a) 0 μM , (b) 10 μM , (c) 20 μM , (d) 30 μM , (e) 40 μM , (f) 50 μM . Inset: Linear plot of absorbance of Ag nanoparticle vs uric acid concentration ($R^2=0.8826$), uric acid concentration range= 0 to 5×10^{-5} mol.dm $^{-3}$.

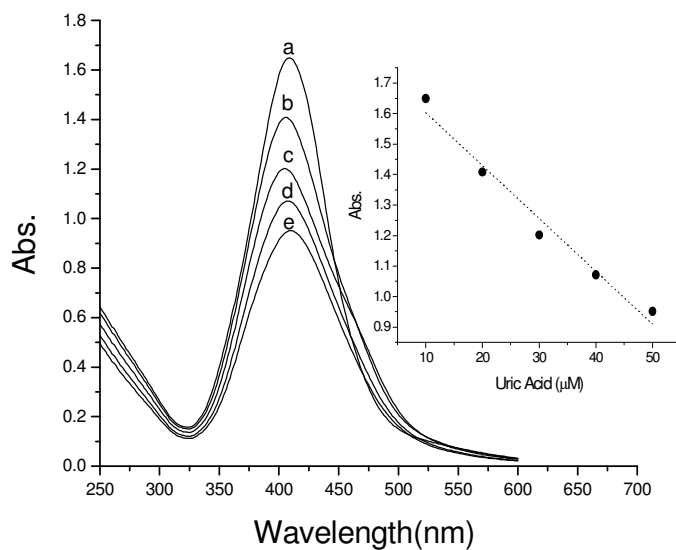


Fig. 4.20 Absorption spectra of Ag nanoparticle solution (PVP, Mol wt.= 160kD) in presence of different concentration of uric acid, after 8 hrs: (a) 0 μM , (b) 10 μM , (c) 20 μM , (d) 30 μM , (e) 40 μM , (f) 50 μM . Inset: Linear plot of absorbance of Ag nanoparticle vs uric acid concentration ($R^2=0.9679$), uric acid concentration range= 0 to 5×10^{-5} mol.dm $^{-3}$.

4.3. Conclusions

The application of X-ray irradiation induced reduction of aqueous metal ions was explored as a probable tool for fabrication of metal nanoparticles in addition to gamma and E-beam irradiation techniques. A comparative study of the three techniques revealed a more poly-dispersed particle size distribution for Ag NPs synthesized using X-ray irradiation compared to those obtained using gamma ray irradiation and EB-irradiation methods. Parameters such as precursor ion concentration, stabilizer molecular weight and concentration were found to play a crucial role in deciding the morphology of the particles formed. A novel biosensor was subsequently designed using PVP-Ag-NPs synthesized via gamma radiolytic method, and demonstrated for estimation of uric acid in biological samples. No external reducing agent has been used in this method. A colorimetric method based on oxidation of PVP stabilized Ag nanoparticles by in situ generated hydrogen peroxide has been developed for estimation of uric acid. Linear range of detection of uric acid by this technique was found to be 0 to 5×10^{-5} mol.dm⁻³ with minimum detection limit of 5×10^{-6} mol.dm⁻³. The molecular weight of the capping agent PVP was found to play a crucial role in the efficacy of the PVP-Ag-NPs system as a sensor for uric acid estimation; lower the molecular weight of PVP, faster and better the response towards sensing the uric acid. Further, this method was also effectively employed to determine concentration of uric acid in actual biological fluids, namely bovine and human serum samples. T-tests and F-test carried out on the analysis results demonstrated that the proposed method offers reasonably good accuracy and precision in case of real samples. The PVP-Ag-NPs system was also observed to possess a shelf life of more than six months when stored at 4⁰C. This novel detection method using nanomaterials has potential applications in medical and environmental monitoring as a simplified, low cost biosensor for uric acid estimation in the micro-molar range.

Chapter 5: Radiation induced fabrication of metal nanoparticles/inorganic fillers based polymer nanocomposite films for optical limiting and flame retardant applications

5.1. Introduction

Inorganic-Organic hybrid nanocomposite materials have received great attention from the industrial community because of their wide range of novel physical properties. Relative to virgin polymer or conventional composites, polymer nanocomposites show significant improvement in certain material properties, such as barrier property, enhanced mechanical properties, optical limiting properties etc. In particular, metal nanoparticles based nanocomposite materials have found wide application in recent years as optical limiting materials. The widespread use of high power lasers operating over a wide range of wavelengths and pulse durations and the increase in the applications of lasers has led to a surge in the need for optical limiters, which are indispensable in the context of protection of optical components and the human eye from laser-induced damages. An ideal optical limiter is defined as a device which exhibits appreciable linear transmission below a threshold input fluence and a constant transmission above it [192]. Although numerous materials have been discovered and developed over the years as optical limiters, including materials such as phthalocyanines, porphyrins, fullerenes, carbon nanotubes, organic dyes etc. [193-198], metal nanoclusters based nanocomposites stand out as one of the best options owing to their unique non linear optical properties, such as two-photon absorption (TPA), saturable absorption (SA), reverse saturable absorption (RSA), and self-focusing/defocusing arising from nonlinear refraction [199-205]. Metal nanoparticles (NPs) dispersed in polymer matrices combine the properties of both the inorganic and polymer components, thereby yielding significantly enhanced performances [206]. The polymer matrix provides the platform for

maintaining the size, shape and dispersion of the metal nanoparticles- parameters which play a vital role in deciding the properties exhibited by the particles. At the same time the polymer matrix also provides additional qualities, such as processability, solubility or thermal stability to the system.

Another important application of polymer nanocomposite materials is in the field of flame retardants. Early flame retardants included use of halogenated compounds. But these are currently being phased out because of environmental concerns [207,208]. Alternatively, metal hydroxides [209-211] and intumescent flame retardant (IFR) [212,213] additives, as main halogen-free flame retardants (HFFR), have also attracted considerable attention. However, large loadings of IFR additives and metal hydroxides are usually needed (>60 wt %) in the polymer matrix to get high flame retardancy, which leads to significant loss in the mechanical properties of the polymer. Hence, layered silicates (clay)-polymer nanocomposites containing modified organophilic clay as nano fillers have been the focus of research over the past few years owing to their unique flame retardant properties [214-217].

The addition of clay to organic polymers differs from conventional blending of non-swelling inorganic fillers into polymers, as the clay nanofiller interacts with the organic matrix at a nano-scale level, and the final structure depends largely on the extent of intermixing and compatibility between the organic and the inorganic phases. Clay is identified as an inexpensive, environmentally benign nanofiller material with unique, mechanical, barrier and rheological properties. On adding just a tiny amount of clay to the polymer matrix, these new-generation composite materials exhibit significant decrease in the peak heat release rate (PHRR), change in the char structure, and decrease in the mass loss rate during combustion in the cone calorimeter [218-225]. It does not have the usual drawbacks associated with other fire retardant additives. Moreover, these PCN materials exhibit increased physical, thermal and mechanical properties [226-230].

Polyurethanes are the most widely used polymers in the field of polymer nanocomposites. The overwhelming popularity of polyurethane as the base matrix is due to its unique properties such as excellent abrasion resistance, flexibility, hardness, chemical resistance, solvent resistance, light stability and weatherability, and wide range of applications, including in the field of adhesives, foams, textiles, membranes, elastomers and rubber adhesion promoters, besides in coatings [231,232]. Inclusion of nanofillers into these polyurethane matrices leads to further enhancement in their thermal and mechanical properties, thereby expanding the scope of their application into more diverse fields. Hence, for all our applications polyurethane based oligomers were used as the base matrix.

Mechanical noncovalent blending, including melt blending and solution blending, is usually used for the fabrication of polymer composites. In case of metal nanoparticles based polymer composites, fabrication is mostly done by mixing preformed nanoparticles with the polymer in solution and casting the composite films (ex-situ). However, these methods put severe limitations on the homogeneous dispersion and interaction of the fillers with the base matrix. Therefore, in recent years focus has been shifted to the use of high energy radiation sources for engineering polymer nanocomposite materials. Compared to conventional techniques, the major advantages of using high energy radiation, including electron beam or gamma irradiation, for curing, are that these are pollution-free, high efficiency techniques that impart long service life, uniform cross-linking degree, and excellent heat-resistance and cold-resistance properties to the materials [233,234]. Moreover, inorganic/organic nanocomposites containing inorganic nanofillers fabricated using radiation curing method were found to exhibit distinctly enhanced properties compared to conventionally prepared materials [235]. In the case of metal-polymer nanocomposites, this technique facilitates in situ generation of metal nanoparticles in the polymer matrices [236,237]. Variation of parameters such as the radiation dose, dose rate and metal/polymer ratio allows easy control

over the size and dispersion of the metal nanoparticles as well as the overall properties of the nanocomposite material.

In this chapter, fabrication of flexible silver nanoparticles-polyurethane acrylate based polymer nanocomposite films (PNCs), possessing optical limiting properties, via electron beam irradiation route has been discussed. Aliphatic urethane acrylate was used as the base matrix. A 2Mev Electron beam source was used to achieve curing of the coating formulations by subjecting the samples to an optimized radiation dose. The PNC samples were characterized in detail and tested for their optical limiting properties using a Nd-YAG Laser operated at third harmonic wavelength of 355nm with 25ns pulse and 10 Hz cycle. The chapter also discusses the synthesis of modified montmorillonite clay based nanocomposite films using the same polymer matrix and study of their various properties including flame retardant property. A ^{60}Co Gamma chamber was used to achieve curing of the coating formulations by subjecting the samples to an optimized radiation dose.

5.2. Fabrication of nanocomposite films

Radiation curing of polymers using ionizing radiation is an established technique for fabrication of polymer coatings and films. Therefore, this technique was adopted to fabricate uniform nanocomposite polymer films containing modified clay/ insitu generated metal nanoparticles as nanofillers. Aliphatic urethane acrylate (AUA) was chosen as the base matrix (fig. 5.1a). Trimethylolpropane triacrylate (TMPTA) (fig. 5.1b) was used as the reactive diluent, which not only regulates the viscosity of the oligomer but also serves as a crosslinker by virtue of its three functional acrylate groups that help form connecting bridges between the polymer chains during the process of radiation induced curing of the oligomer.

5.2.1. Synthesis of Ag NPs/polyurethane acrylate based films

The precursor ion stock solution of silver nitrate was prepared in methanol as the solvent because of its ready miscibility with the oligomer-diluent reaction mixture. The AUA-TMPTA ratio was maintained at 4:1 to achieve optimum viscosity and to ensure maximum crosslinking between the polymeric chains. Three different volumes of Ag⁺ ion solution were added to 5g AUA-TMPTA mixtures to arrive at final Ag⁺ ion concentrations of 8, 15 and 30mM. Radiation doses were optimized at 150kGy to achieve non tacky homogeneous polymeric films in which Ag NPs were generated in situ via radiolytic reduction of the precursor Ag⁺ ions.

5.2.2. Synthesis of organophilic clay/polyurethane acrylate based films

Cloisite 20A, a montmorillonite clay, modified with an organic modifier (fig 5.1c) and Cloisite 30B, a montmorillonite clay, modified with an organic modifier (fig 5.1d) were used as nanofillers to impart flame retardant properties to the polymer films. These modified montmorillonite clay samples in different concentrations (%w/w) were added to an optimized mixture (4:1) of AUA and TMPTA. To achieve uniform dispersion of the filler in the coating formulation, each of the samples was subjected to probe ultrasonication (Q700, Qsonica, USA) for 30 min. The formulations obtained were coated onto glass substrates and subjected to γ -radiation for a total absorbed dose of 150kGy to obtain non-tacky, homogeneous PCN thin films under aerated condition. The thickness of the EB cured coatings was found to be ~100 μ m as estimated by a thickness gauge ‘coat measure M12’ (Yuyutsu, JAPAN).

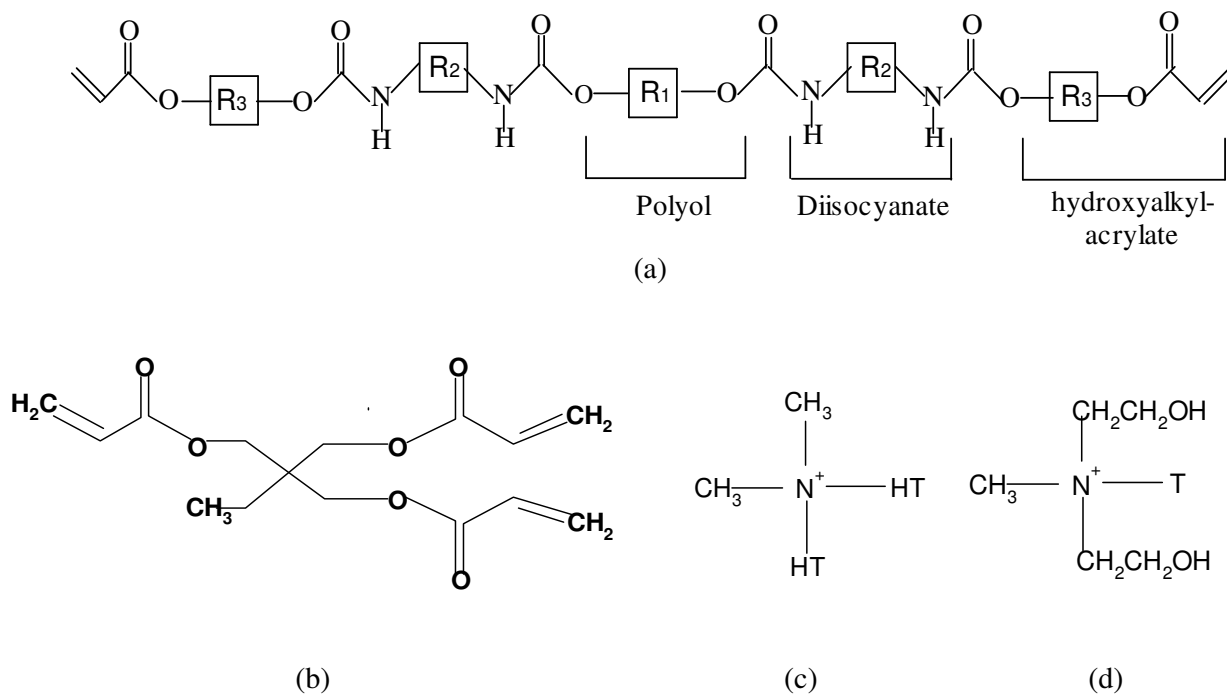


Fig. 5.1 Chemical structure of (a) Oligomer-Aliphatic urethane acrylate (AUA) (b) Reactive diluent-Trimethylolpropanetriacrylate (TMPTA) (c) Organic modifier for Cloisite 20A (where HT: hydrogenated Tallow) and (d) Organic modifier for Cloisite 30B (where T: Tallow)

5.2.3. Characterization of Ag based films

The formation of Ag NPs in the polymer matrix was confirmed by the bright yellow colour generated in the film as compared to the colorless control polymer film. UV-visible spectroscopy of the films were carried out [fig 5.2] which show characteristic narrow Surface Plasmon Resonance (SPR) band of Ag NPs at ~420nm, thereby confirming the formation of more or less uniform sized, spherical silver nanoparticles within the polymer matrix. The intensity of the SPR band increased proportionately with increase in the Ag concentration of the PNC film.

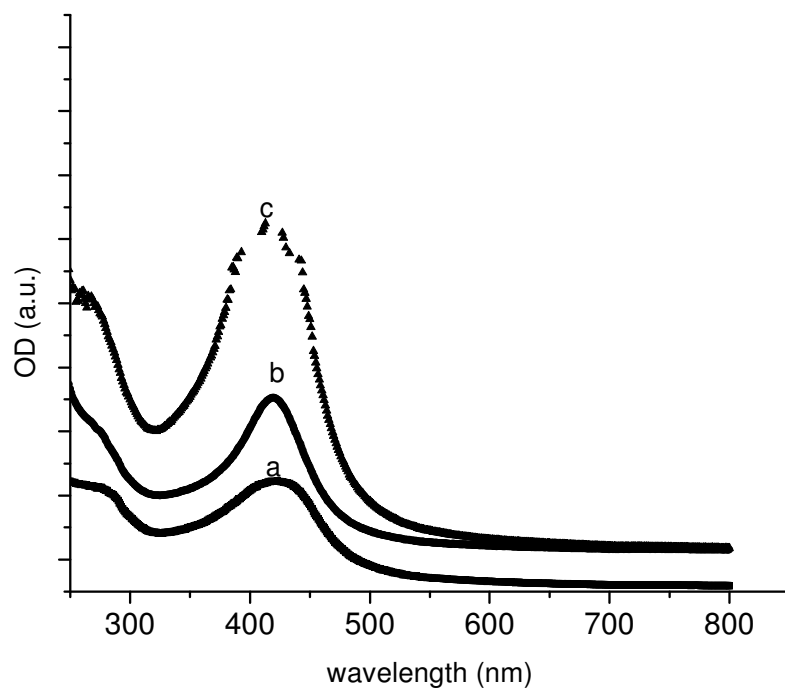


Fig 5.2 UV-Vis spectra of PNCs containing(a) 8mM (b) 16mM and (c) 30mM Ag NPs as fillers

Fig 5.3 presents the TEM image of the in situ generated Ag NPs. TEM analysis clearly indicated formation of uniformly dispersed spherical nanoparticles with average particle size of 6-8nm

FE-SEM image shown in fig 5.4 also confirms the formation of uniform sized spherical Ag NPs embedded in the polymer matrix.

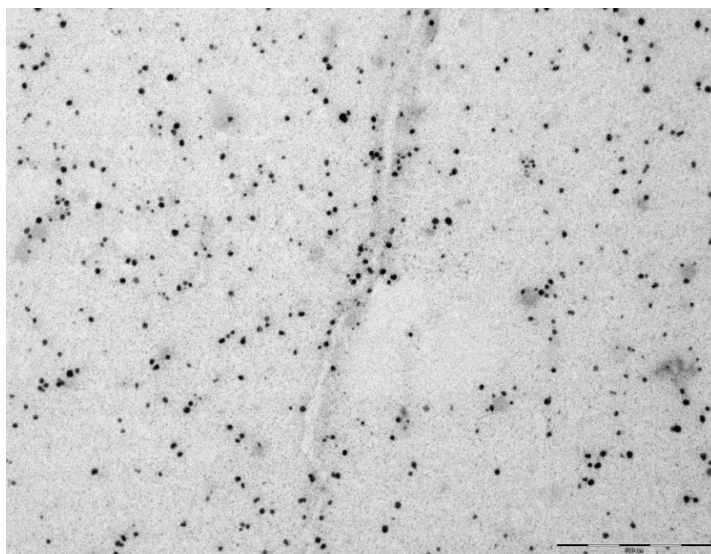


Fig. 5.3 TEM image of Ag NPs embedded in AUA-TMPTA PNC film

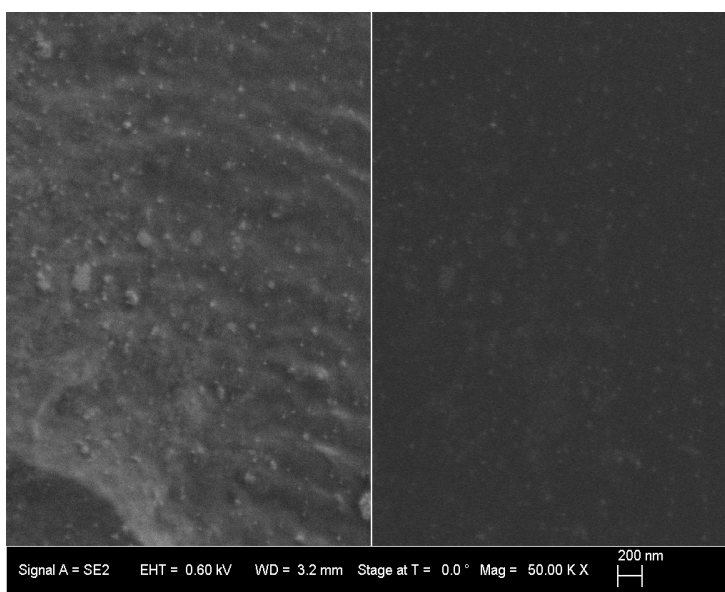


Fig. 5.4 FE-SEM image of Ag NPs embedded in AUA-TMPTA PNC film

5.2.4. Evaluation of Optical limiting property: proposed mechanism

The optical-limiting behaviors of the composites with different Ag NPs concentrations were measured using Nd:YAG laser with 25 ns pulse duration and 355 nm wavelength. The sample was mounted on a metal frame and the laser beam focused on the sample surface with a spot size of 1.0 mm diameter. The incident and transmitted energy were detected simultaneously by two power meters. The film was exposed to the laser beam for a duration of 10 seconds. The incident laser power was increased after every 10 second exposure till complete burnout of the samples was observed. The result is shown in Fig5.5, which distinctly highlights the optical-limiting effect of PNC containing 30mM Ag NPs as the nanofiller. At very low output energy, the response of the composite was linear to the input energy. The linear transmittance was found to be approximately 82% while the limiting or threshold input fluence beyond which the sample stopped transmitting the laser beam was calculated to be 3.8 J/dm². Similar trends were observed for composites containing 8 and 16mM Ag NPs as filler. This clearly indicates that the transmittance and threshold fluence of the films was independent of the concentration of the nanofillers in the range under study; with the common base polymer matrix acting as the deciding factor in determining the extent of transmittance.

Although different processes such as transient absorption, two-photon or multi-photon absorptions, interband and intraband transitions and nonlinear scattering are known to lead to optical limiting behavior in metal nanoparticles, the predominant mechanism responsible for optical limiting behaviour in polymer films containing metal nanoparticles is Reverse Saturable Absorption (RSA). The RSA may be attributed to excitations from the plasmon band to the free carrier band of metal nanoparticles (eg. Ag NPs). At higher input fluences, fast decay of the free carriers to the plasmon band can also lead to optical limiting through Saturable Absorption (SA).

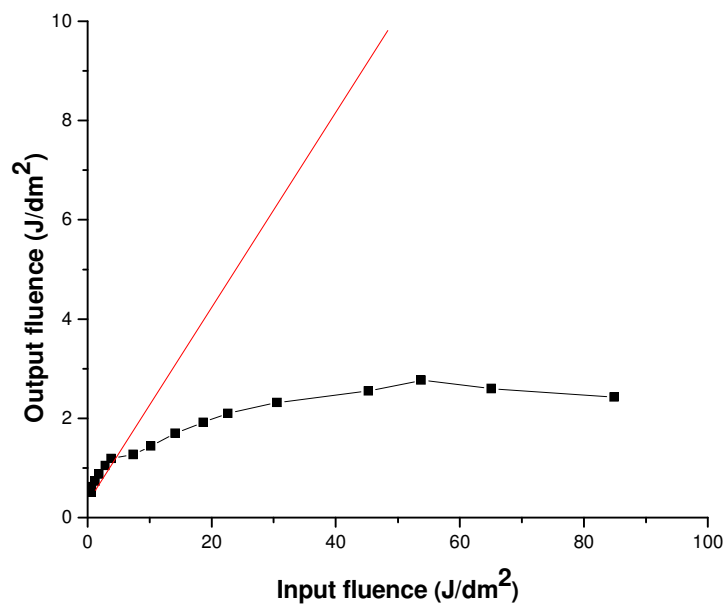


Fig. 5.5 Plot of output fluence as a function of input fluence for 10 sec exposure duration

In order to study the effect of the exposure duration on the optical limiting effect of the PNC film, similar experiments were carried out by limiting the time of exposure to 1 second. Fig. 5.6 shows the variation in optical limiting characteristics for PNC containing 30mM Ag NPs with change in the time of exposure. Exposure for 1 second led to significant improvement in the optical limiting property of the material, which was manifested in the decrease in threshold fluence from 3.8 J/dm² to 1.2 J/dm². The dynamic range, which is defined as the ratio of the maximum input fluence till which material displays optical limiting behavior to the threshold fluence, was also found to increase from 22.34 to 80.10. In other words, exposure for lesser durations not only led to an early cut off for the laser transmission but also increased the overall lifetime of the material. This can be explained on the basis of the fact that continuous exposure for long durations led to accumulation of laser power within

a small area (determined by the beam diameter) thereby culminating in rapid degradation of the product.

In addition to Ag NPs as fillers, the effect of addition of fillers such as thiophene and modified montmorillonite clay (Cloisite 30B) in conjunction with Ag NPs, on the optical limiting behavior, was also studied. The results are highlighted in fig 5.7. It was observed that for an exposure duration of 1 second, change in the filler concentration or nature did not lead to any change in the threshold fluence of the materials. However, the presence of cloisite 30B as additional filler led to a slight increase in the initial output fluence of the materials. On the other hand Thiophene/Ag based films exhibited increased output fluence at higher input fluencies. At the same time, composites containing Cloisite 30B/ Ag NPs as fillers showed early damage resulting in a narrower dynamic range compared to the other two composite films. Thus by simply adding an additional filler along with Ag NPs the optical limiting properties of the PNC films could be effectively tuned to get the desired output fluence or dynamic range without comprising on the threshold fluence of the material.

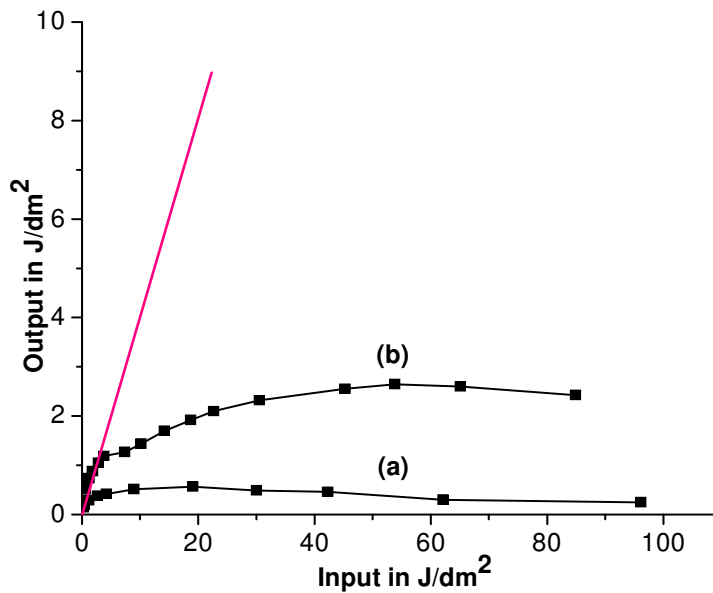


Figure 5.6 Variation of optical limiting property with exposure duration [(a) 1 sec vs (b) 1sec exposure duration]

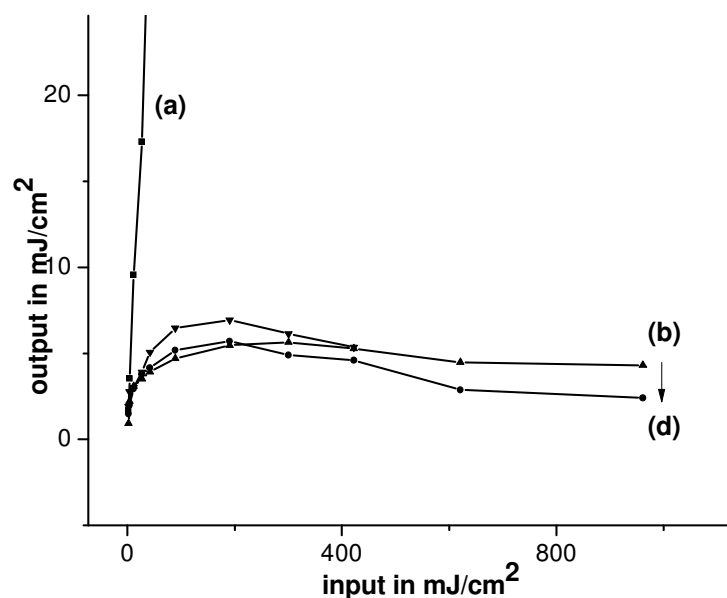


Figure 5.7 Optical Limiting property of (a) control film and films with (b) Ag NPs (c) Thiophene/Ag NPs and (d) Cloisite 30B/Ag NPs as nanofillers

5.2.5. Characterization of clay based films

The characterization of Polymer Clay Nanocomposite (PCN) films was carried out by the following techniques

UV-visible spectroscopy

UV-visible spectrophotometry was employed to examine the transparency of the PCN films. Fig. 5.8 shows the UV-Visible spectra of the PCN films containing Cloisite 20A with ~100nm thickness. It was observed that the transparency of AUA-TMPTA films was slightly decreased with the incorporation of nanoclay filler. The transmittance of the PCN decreased marginally with the increase in the clay loading, particularly in higher range of visible light. The significant transparency of the PCN films supports the uniform dispersion of the clay in the polymer matrix. Similar trend was observed in case of films containing Cloisite30B nanoclay (data not shown).

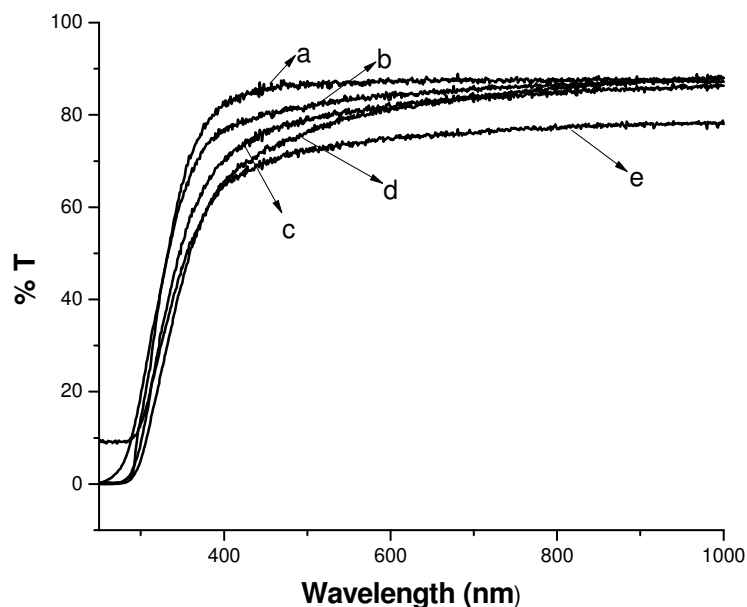


Fig. 5.8 UV-visible transmittance spectra of PCN films containing Cloisite 20A as nanofiller (a) 0% (b) 2% (c) 5% (d) 10%.

FTIR analysis

The FTIR spectrum of control polyurethane acrylate film (Fig. 5.9a) exhibits the characteristic peaks of typical polyurethane acrylate: broad band at 3380 cm^{-1} (H-bonded NH stretching), 1735 cm^{-1} (C=O stretching), doublet at $2860\text{--}2930\text{ cm}^{-1}$ (stretching mode of -CH_2), 1462 cm^{-1} (bending mode of -CH_2), 1340 cm^{-1} (Stretching mode of CN), 1525 cm^{-1} for amide II (NH bending and CN stretching), 1242 cm^{-1} for amide III and 1033 cm^{-1} (C-O-C stretching). Fig. 5.9b presents the FTIR spectra of PCN films containing cloisite 20A nanoclay. Signature of clay was clearly evident from the following IR peaks observed in the spectrum: a high intensity peak at 1042 cm^{-1} corresponding to Si-O-Si stretching modes and 890 cm^{-1} Al-OH-Al deformation of aluminates stretching modes associated with tetrahedral polyhedra [238].

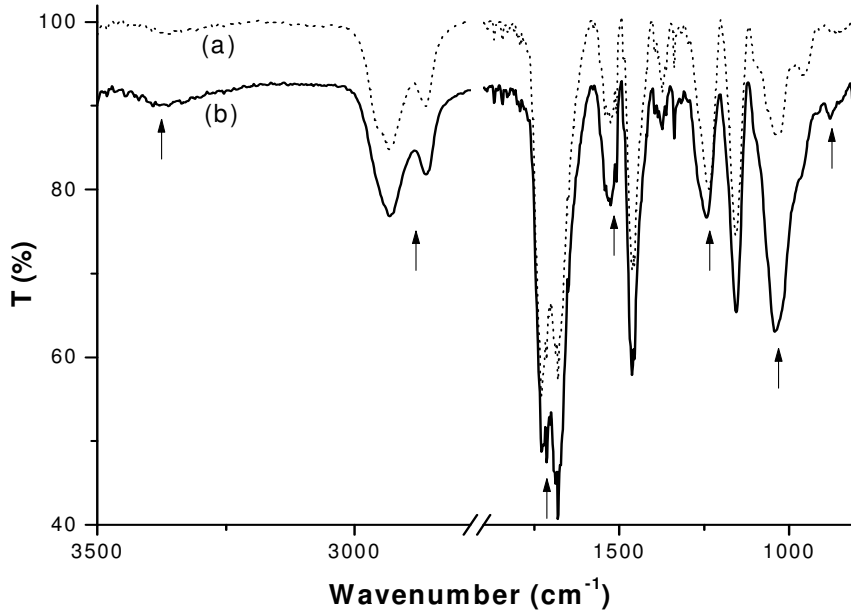


Figure 5.9 FTIR spectra of PCN films (a) without nanoclay, (b) with 10% nanoclay (cloisite 20A)

XRD and SAXS analysis

XRD and SAXS analysis of the PCN films was performed in order to find out the dispersion of the nano-clay in the polymer matrix. Fig. 5.10(a) and 5.10(b) present the XRD data for PCNs with Cloisite 20A and Cloisite 30B, respectively. XRD data showed a significant shift in peaks position towards lower 2θ values in PCN films as compared to that of pure clay. Pristine Cloisite 20A and Cloisite 30B powder clay samples were found to have $2\theta=3.36^\circ$ (interlayer spacing=2.65nm) and $2\theta=4.74^\circ$ (interlayer spacing=1.88nm), respectively. The interlayer spacing between the silicate layers of clay increased when incorporated in the PCN matrices. The 2θ peak position of PCN-20A and PCN-30B nanocomposite samples shifted to 2.50° (interlayer spacing=3.5nm) and 2.92° (interlayer spacing=3.08nm), respectively. It was found that the PCN sample containing clay showed lower intensity peak as compared to pure clay sample. Moreover, the peak intensity was

found to decrease with the decrease in the clay concentration in the PCN films, suggesting the formation of mixed exfoliated/intercalated silicate nanolayers of the clay particles at lower clay loading. However, the decrease in 2θ and corresponding increase in the interlayer spacing value for higher clay loading in PCN matrix also indicated significant intercalation of the layered structure of clay.

To determine the effect of temperature on the composite morphology, *in-situ* high temperature SAXS experiment was also carried out using PCN-20A-5% sample. In the first set of experiment, PCN sample was heated and scattering data was collected at different temperatures. It was observed that elevation in temperature above 100°C resulted in a shift of the peak towards higher 2θ values, indicating a gradual decrease in the interlayer spacing of the silicate (Fig. 5.11a). This may be attributed to the elimination of water molecules trapped within the interlayer spacing of clay platelets, thereby causing a reverse delamination effect and restacking of the silicate layers.

In the second set of experiment, the PCN sample was subjected to an isothermal heating at 150°C for 50 min. The SAXS scattering data is shown in Fig. 5.11b. It was evident that no significant shift of the peaks occurs at 150°C till 50 min. Therefore, we subjected the PCN sample to a still higher temperature of 200°C for longer time period up to 315 min to see whether there is time and high temperature induced change in the intercalated/exfoliated structure of clay in PCN. However, in this case also, there was no significant shift in peak position observed (data not shown), which suggested that PCN is quite stable at higher temperature as far as intercalation/exfoliation of the clay in the PCN matrix is concerned.

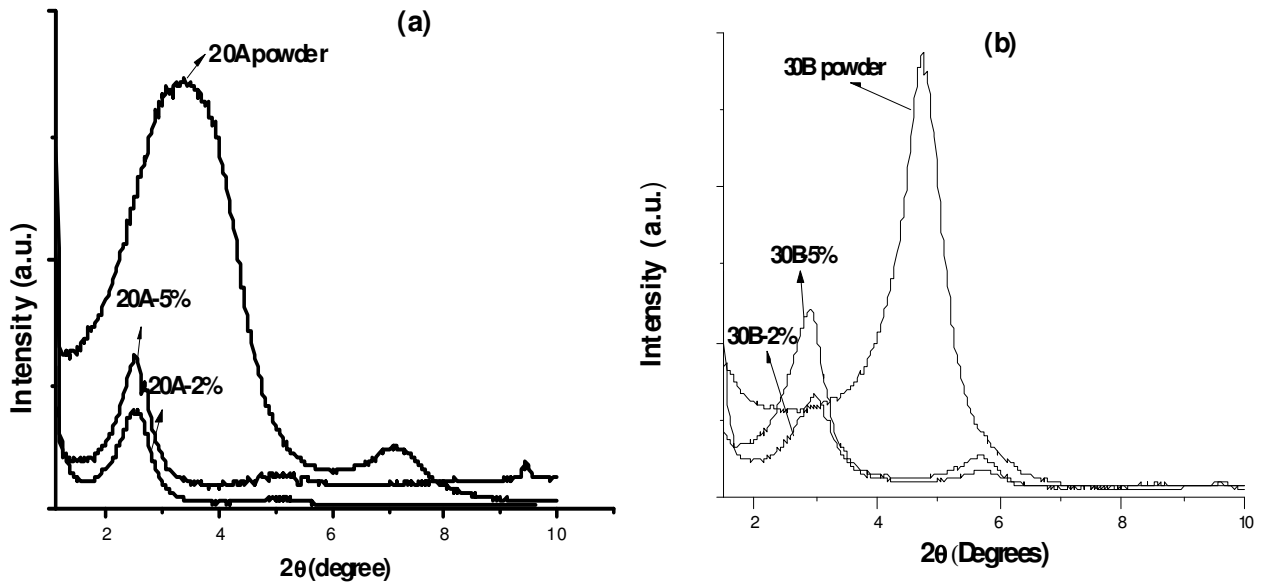


Fig. 5.10 X-ray diffraction patterns of (a) nanoclay powder-Cloisite 20A and PCNs containing 2% and 5% Cloisite 20A, (b) nanoclay powder-Cloisite 30B and PCNs containing 2% and 5% Cloisite 30B.

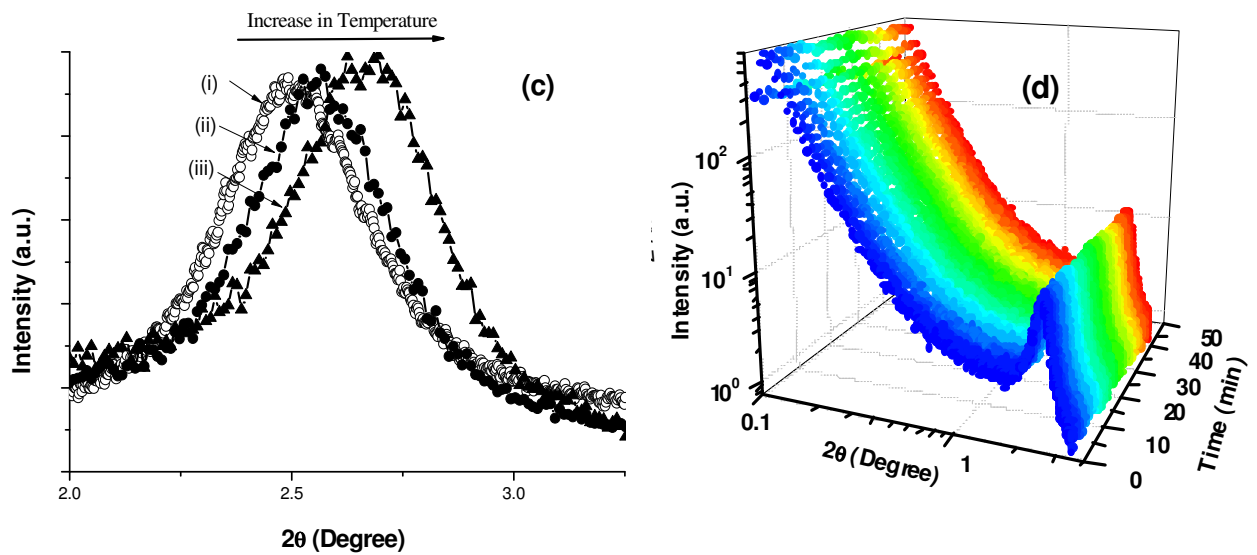


Fig. 5.11 (a) SAXS diffraction patterns of PCNs containing 5% Cloisite 20A at temperatures (i) 25°C, (ii) 150°C and (iii) 200°C and (b) In-situ isothermal scattering data at 150°C as a function of time.

TEM analysis

Fig. 5.12a and 5.12b present the TEM images of PCN films containing 2% cloisite 20A and cloisite 30B nanoclays, respectively. The microstructure represents a well-ordered multilayer morphology consisting of alternate polymer and inorganic layers, although their interlayer spacing turns out to be much higher in the composite in comparison to the nanoclay powder samples. TEM micrographs highlight regions with uniform distribution and good dispersion of nanoclay particles in addition to the intercalated/exfoliated regions in the PCN matrix. This was also supported by XRD results showing higher interlayer spacing and lower intensity of the XRD peaks for PCNs compared to the neat nanoclay powder samples.

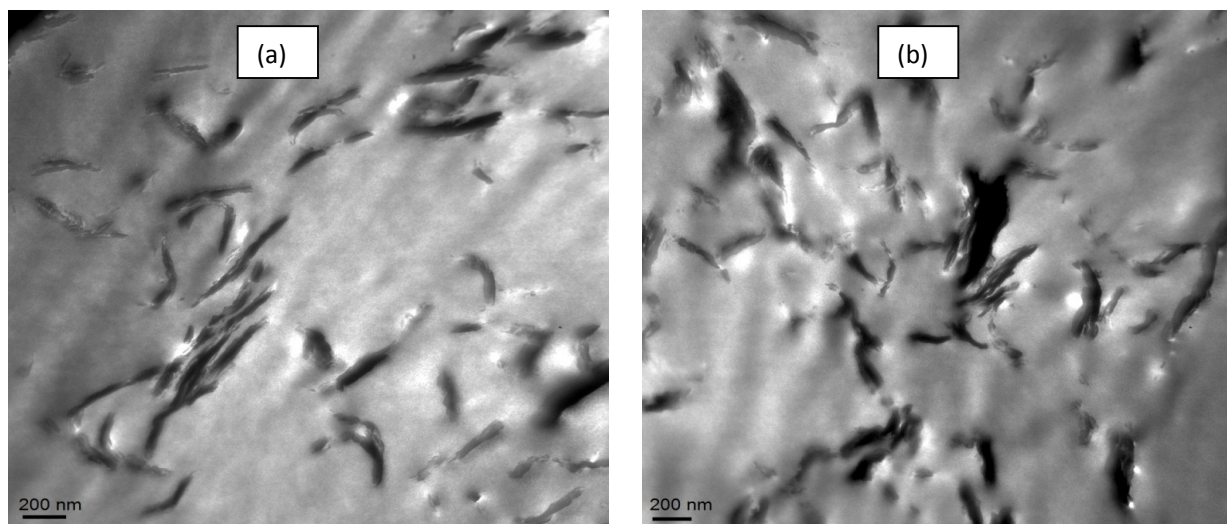


Fig. 5.12 TEM images of PCN films containing 2% nanoclay (a) Cloisite 20A and (b) Cloisite 30B

SEM analysis

Fig. 5.13 presents the SEM images of the fractured surfaces of control polymer film and PCNs containing modified montmorillonite clay (cloisite 20A as representative clay nanofiller). Fig. 5.13a presents the SEM image of polymer film without nanoclay filler, and shows fairly homogenous bulk morphology which is smooth and dense and bears no evidence of pores or channels. This indicates a typical fractography feature of brittle fracture behavior, thus accounting for the low fracture toughness of the neat coating. In fig. 5.13b-5.13e, the grey colored regions indicate the bulk of the polymer matrix and the brighter regions indicate the distribution of clay particles. However, the phenomenon of exfoliation, intercalation and aggregation is difficult to study from SEM conclusively, which gets distinctly reflected in TEM micrographs and XRD studies. For clay loadings up to 5%, uniform dispersion of the silicate layers in the polymer matrix can be clearly observed. However, clay loadings of 10% and 15% were found to affect the overall morphology of the polymer matrix, manifested as an increase in the fracture surface roughness (Fig. 5.13d and 5.13e). An increase in fracture surface roughness is an indicator of crack deflection mechanism, which increases the absorbed energy of fracture by increasing the crack length during deformation [239].

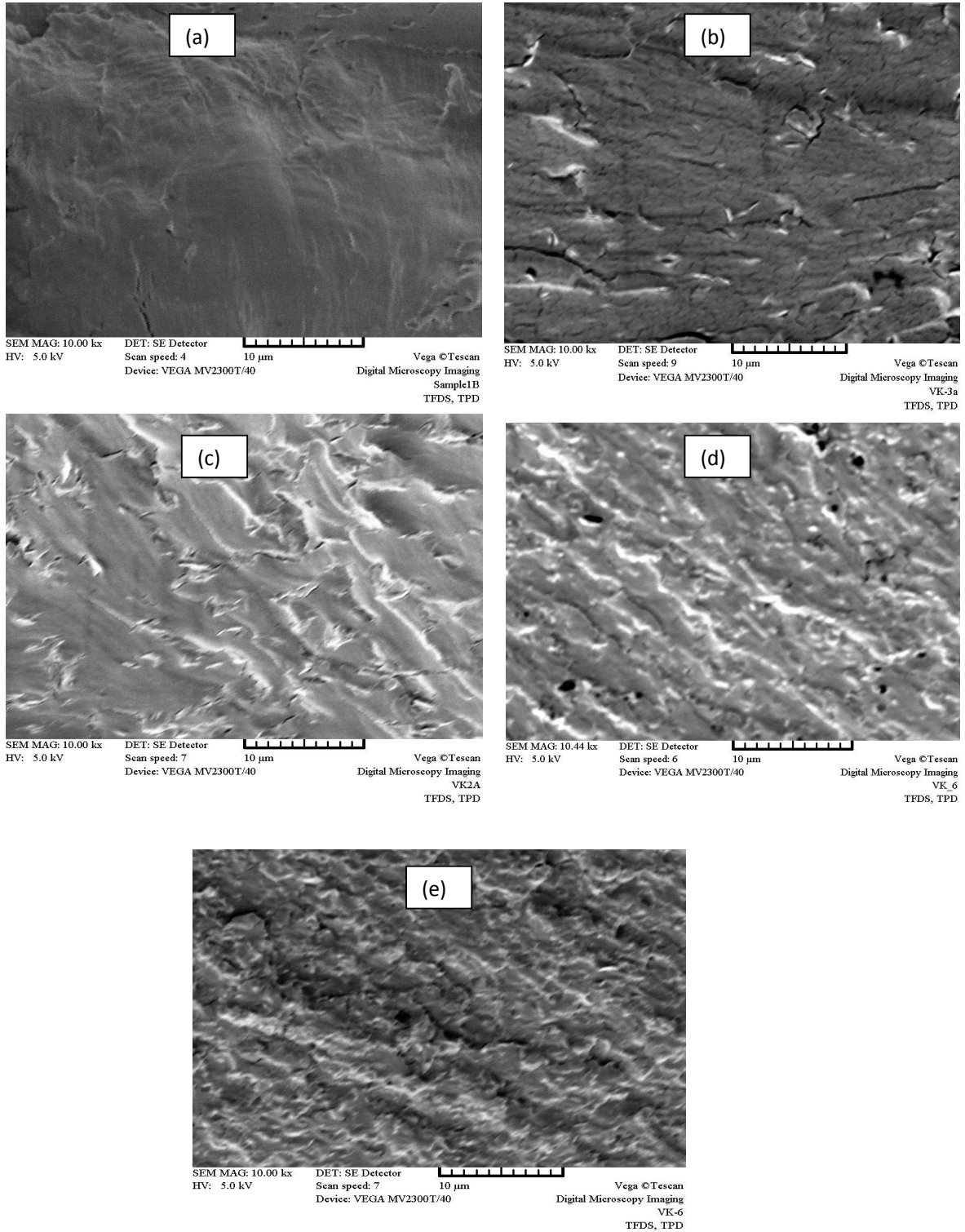


Fig. 5.13 SEM images of PCN films containing Cloisite 20A nanoclay (a) 0% (b) 2% (c) 5% (d) 10% and (e) 15%

DSC analysis

The glass transition temperature T_g of a polymer is an important indicator of its temperature/time dependent viscoelastic behavior, which is often an important factor in determining the usefulness of a given polymer. T_g also provides information about inter/intra-molecular interaction between components of a polymer composite. In case of polyurethane-clay nanocomposites, changes in the glass transition temperature can be interpreted as a result of effective interaction between polymeric chains and the silicate surface. Fig. 5.14a, 5.14b and 5.14c present the DSC thermograms of AUA-TMPTA, PCNs containing 5% cloisite 20A and cloisite 30B nanoclays, respectively. Incorporation of the nano-clay was found to result in a minute shift in T_g values of the composites towards higher temperatures. While T_g for control film was found to be -2.76° , that for PCNs containing 5% 20A and 30B nanoclay were recorded to be 0.12° and -0.93° respectively, indicating reduced chain segment mobility induced by the modified clay [240]. This is probably due to the fact that the restricted relaxation behavior for the polymer nanocomposites with intercalated or exfoliated silicates primarily depends on the extent to which the layered silicates interact with the polymer matrix. Exfoliation would result in enhanced interaction culminating in a large shift in T_g value. However, intercalation would lead to a relatively lesser degree of interaction, which gets manifested as only a marginal shift in T_g values. This corroborates with the results obtained from SAXS analysis.

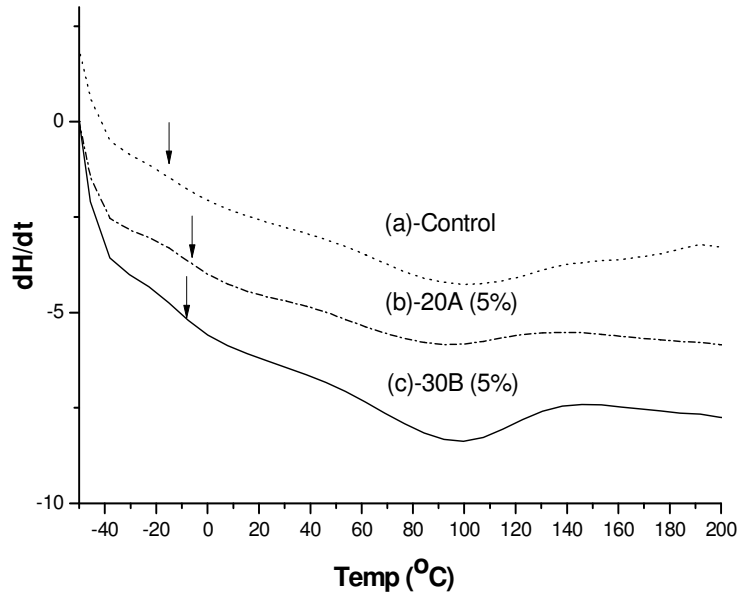


Fig. 5.14 DSC profiles of PCN films (a) without nanoclay (b) with 5% Cloisite 20A and (c) 5% Cloisite 30B

5.2.6. Property evaluation of PCN films

Pendulum hardness

Pendulum hardness is a qualitative test frequently used in coating in order to compare the surface hardness property of different coatings. As per standard test method (ASTM: D 4366-95) for pendulum hardness test of organic coatings, the ‘pendulum hardness’ of coatings is reported in terms of damping time (in seconds) of pendulum rested on the coating surface for a swing amplitude of pendulum to decrease from 12^0 to 4^0 . This test method is based on the principle that amplitude of oscillation of the pendulum touching the coating surface decreases more rapidly on the softer coating because of higher degree of damping of oscillation. For a smooth surface, softer coating will exhibit lower damping time, whereas, harder coating will exhibit higher damping time. Results of pendulum hardness test performed on PCNs with varying concentrations of nanoclays, are presented in Fig. 5.15. It

was observed that the incorporation of nano clay into AUA-TMPTA coating increased its pendulum hardness (i.e., damping time) up to 5% clay loading (cloisite 20A as well as clisite 30B), beyond which, the pendulum hardness was found to decrease. Higher clay content (>5%) may have interfered with the crosslinking reaction between different polymer chains of the PCN matrix, resulting in a relatively softer surface, and thereby decreased pendulum hardness. It can be seen that as compared to Coisite 20A, Cloisite 30B yielded better hardness in PCN film, which may be attributed to the better compatibility between AUA-TMPTA matrix and Cloisite 30B due to more polar modifier used in Cloisite 30B.

Gloss at 60⁰

Specular gloss of the cured samples was measured at 60⁰ angle of reflectance using Novo triple angle Gloss meter (J402-268, Elcometer, UK) and the results are reported in gloss unit (GU). Specular gloss at 60° is a measure of the ability of coating surface to reflect a beam of light in a particular angle (i.e. 60°) without scattering. This is an important property of coating specially used for aesthetic and decorative purposes. The gloss values of gamma radiation cured PCN coatings with different loading of nanoclay cloisite 20A are presented in inset Figure 8. It was found that incorporation of nanoclay led to a decrease in the specular gloss with increasing nanoclay loading. Decrease in gloss of nanocomposites coating was attributed to matting effect caused by increase of surface roughness upon addition of the nanoclay.

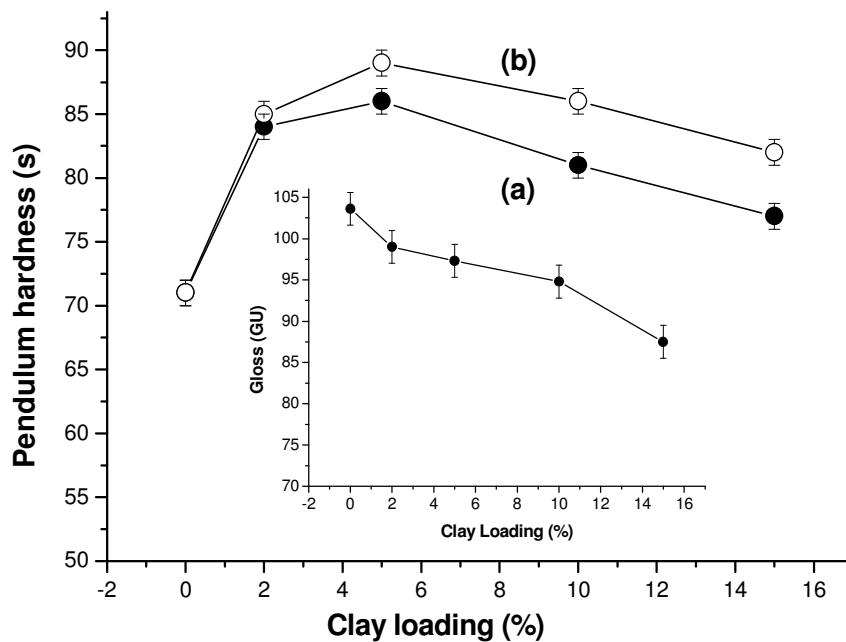


Figure 5.15 Pendulum hardness analysis of PCN films with different loadings of nanoclay (a) Cloisite 20A, (b) Cloisite 30B. (Inset: Gloss at 60° data for PCNs with different loadings of Cloisite 20A).

Solvent resistance

The PCN coatings prepared were also tested for their solvent resistance properties using acetone as a solvent. Lower the weight loss in acetone, better the solvent resistance property of the PCN film. For PCNs with both cloisite 20A and 30B as filler, clay loadings up to 5% showed increase in gel fraction compared to the neat polymer coating, above which the gel fraction was found to decrease gradually with the increase in filler loading (Table 5.1). Clay loading of 2% was observed to be the optimum value to achieve maximum extent of crosslinking in both cases. Expectedly, similar trend was found for the solvent resistance property of the PCNs in acetone (Table 5.1). This suggested that the presence of nanoclay influences the curing extent of the AUA-TMPTA polymer matrix; clay loadings up to 5%

facilitated the crosslinking of the polymer matrix, while filler loadings higher than 5% hindered the crosslinking process. These results were found to be in line with the hardness analysis results; higher crosslinking extent (gel fraction) of PCN films up to 5% clay loading led to harder coatings.

Water uptake study

One of the important factors affecting the acceptability of novel coating in engineering applications is the degradation of the coating in presence of moisture that will affect the physical and mechanical performances, thereby, leading to its failure. In case of PCNs with cloisite 20A as the filler, the % water uptake was found to be lesser than that in the control film for samples with clay loading up to 5%, whereas for clay loadings of 10% and 15%, the water uptake was found to be higher than that for the control (Table 5.1). The decrease in crosslinking of the polymer chains with increase in clay loading, as evident from the solvent resistance and gel fraction analysis data, is probably responsible for the increased water uptake shown at higher loadings. On the other hand, the decrease in water uptake at 2% and 5% loadings indicates that clay nano fillers at low concentrations can actually enhance the crosslinking extent of the polymer chains. However, in case of PCNs containing cloisite 30B as the filler, the water uptake was found to be higher than that for the control as well as PCNs with cloisite 20A for all filler loadings, which is attributed to the more hydrophilic nature of the modifier used in cloisite 30B.

Table 5.1 Water uptake (%), weight loss (%) in Acetone and Gel fraction of PCNs with different filler loadings

Sample	Water uptake (%)	Weight loss in acetone (%)	Gel fraction (%)
Control	2.23	11.83	88.17
PCN-20A-2%	1.68	9.34	90.65
PCN-20A-5%	2.10	10.51	89.94
PCN-20A-10%	3.70	13.10	86.90
PCN-20A-15%	10.13	25.90	74.10
PCN-30B-2%	2.36	9.83	90.16
PCN-30B-5%	2.78	10.63	89.37
PCN-30B-10%	6.22	14.49	85.51
PCN-30B-15%	11.12	23.07	76.93

TGA analysis: determination of flame retardancy

Several mechanisms have been proposed to describe the flame retardant properties of PCNs. The general view of the flame retardant mechanism is that a carbonaceous silicate char builds up on the surface during burning, which creates a protective barrier to heat and mass transfer. The accumulation of layered silicates on the burning/gasifying sample surface is considered to be due to two possible modes. One is that the layered silicates are left on the sample surface as a result of the decomposition of the polymer matrix by pyrolysis. The other probable mode is the transportation of the layered silicates, pushed by numerous rising bubbles of degradation products and the associated convection flow in the melt, from the interior of the sample towards the surface. The nano-dispersed silicate layers thus slow down the decomposition rate and increase the temperature of degradation by acting as an excellent thermal insulator and mass transport barrier [241]. The flame retardancy of a material is

generally described in terms of its Limiting Oxygen Index (LOI), a parameter calculated from the char yield of the material using the Van Krevelen's equation

$$\text{LOI} = 17.5 + 0.4\sigma \quad \sigma = \text{char yield in \% at } 850^{\circ}\text{C} \quad (1) \text{ [242]}$$

An LOI value of 21 is normally considered as the threshold and materials exhibiting LOI values of 26 and higher are described as flame retardant materials [242]. In order to determine the thermal behavior and flame retardant properties of the polymer films, thermogravimetric analysis of the films was carried out. Fig. 5.16 presents the thermograms of PCN-30B and PCN-20A with clay loading of 2% (w/w) and 5% (w/w). The AUA-TMPTA coatings showed good thermal stability up to $\sim 250^{\circ}\text{C}$. The thermal stability of the coatings showed marginal improvement upon incorporation of nanoclay [243,244]. However, the char yields of the films were found to increase significantly with increasing concentration of the clay nano-filler in the PCN film. The char yield values were correlated to the LOI values of the polymer coatings using equation 1. It was observed that an increase in clay loading resulted in a simultaneous increase in the LOI values of the samples (Table 5.2). The LOI values recorded were found to be higher than 21 for all the PCN samples, with those containing 15% of modified clay cloisite 20A and cloisite 30B showing LOI values higher than 26, suggesting their potential application as effective flame retardant materials.

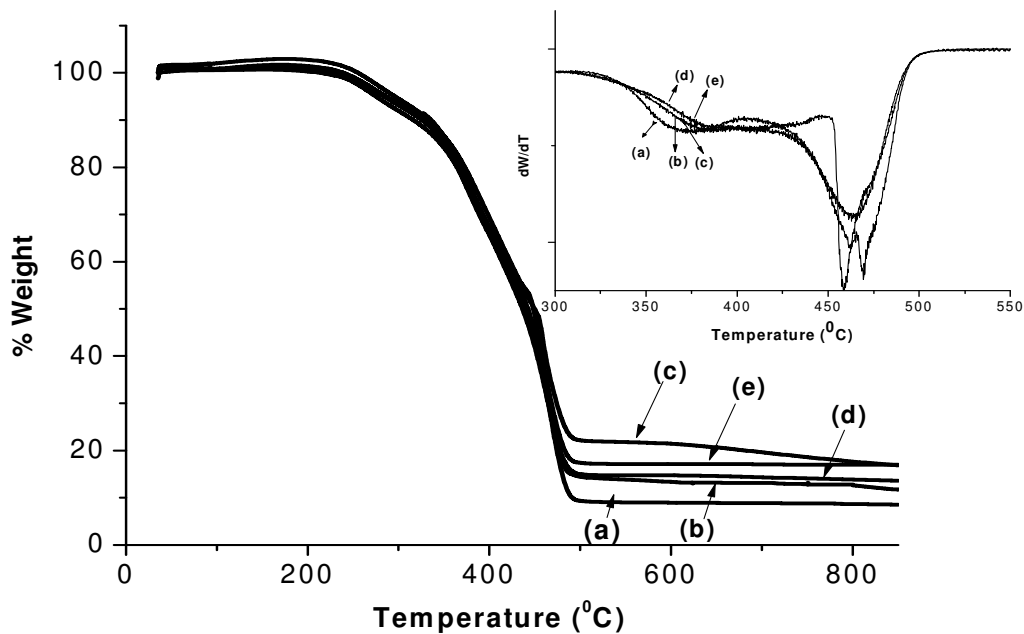


Figure 5.16 TGA analysis of PCN films containing (a) 0% filler (b) 2% Cloisite 20A (c) 5% Cloisite 20A (d) 2% Cloisite 30B and (e) 5% Cloisite 30B. (Inset: Differential Thermogravimetric plots for PCN films containing (a) 0% filler (b) 2% Cloisite 20A (c) 5% Cloisite 20A (d) 2% Cloisite 30B and (e) 5% Cloisite 30B.)

Table 5.2 Limiting Oxygen Indices (LOI) of PCNs with different filler loadings

Clay Sample	LOI
20A-2%	22.3
20A-5%	24.8
20A-10%	25.0
20A-15%	26.3
30B-2%	23.0
30B-5%	24.7
30B-10%	24.8
30B-15%	26.8

5.3. Conclusions

Polymer nanocomposite films containing predominantly in situ generated Ag nanoparticles and other nanofillers in trace quantities were successfully fabricated using E beam irradiation technique. TEM and FE-SEM analysis of the Ag nanoparticles based PNC films revealed formation of well dispersed, spherical nanoparticles in the polymer matrix. The optical limiting studies of the Ag containing PCN films yielded a threshold fluence of 3.8 J/dm² and a dynamic range of 22.34 for an exposure duration of 10 seconds, thereby indicating potential optical limiting applications. Similarly, transparent polymer nanocomposites reinforced with layered silicate inorganic fillers (modified montmorillonite clay) were successfully fabricated via environment benign-gamma radiation curing process. TEM and SEM analyses of the nanocomposites indicated well-dispersed organically modified nanoclay particles with a mixed intercalated/exfoliated structure, which was further supported by the XRD analysis data. *In-situ* high temperature SAXS study indicated that PCN films showed good stability up to 200°C as far as the intercalation/exfoliation of the nanoclay is concerned. The presence of nanoclay in the AUA-TMPTA matrix was found to influence the crosslinking extent of PCNs. The addition of nanoclay did not significantly change the thermal stability of the polymer matrix but was observed to hinder the burning process of the films. Also, it was found to alter the other properties of the PCN films, such as pendulum hardness, specular gloss at 60 degrees, water uptake and solvent resistance. The flame retardant property of the PCN coatings was evaluated in terms of Limiting Oxygen Index (LOI), which was found to increase with increasing clay loading and attained a maximum value of over 26 for 15% (w/w) clay loadings, thereby offering themselves as suitable candidates for potential flame retardant applications.

Refereces

1. T. Hanemann, D.V. Szabó. *Materials*, 2010, 3, 3468
2. M. Krummenacker, J. Lewis. Eds. *Prospects in Nanotechnology toward Molecular Manufacturing*; John Wiley & Sons: New York, NY, USA, 1995.
3. B Bhushan,. Ed. *Springer Handbook of Nanotechnology*; Springer: Berlin, Germany, 2004.
4. P.K. Jain, X. Huang, I.H. El-Sayed, M.A. El-Sayed. *Acc. Chem. Res.*, 2008, 41, 1578.
5. C.J. Murphy, A.M. Gole, S.E. Hunyadi, J.W. Stone, P.N. Sisco, A. Alkilany, B.E Kinard, P. Hankins. *Chem. Commun.*, 2008, 5, 544.
6. J.H. Fendler, Ed. *Nanoparticles and Nanostructured Films: Preparation, Characterization and Applications*; Wiley-VCH: Weinheim, Germany, 1998.
7. G. Schmid, V. Maihack, F. Lantermann, S. Peschel, *J. Chem. Soc. Dalton Trans.*, 1996, 589.
8. Y. Lin, R.G. Finke. *J. Am. Chem. Soc.*, 1994, 116, 8335.
9. H. Bonnemann, G.A. Braun. *Angew. Chem., Int. Ed. Engl.*, 1996, 35, 1992.
10. H. Bonnemann, R.M. Richards. *Eur. J. Inorg. Chem.*, 2001, 2001, 2455.
11. *Nanoscience and Nanotechnologies: opportunities and uncertainties*, The Royal Society & the Royal Academy of Engineering, 2004
12. F. Hussain, M. Hojjati, M. Okamoto, R.E. Gorga. *J. Comp. Mater.*, 2006, 40, No. 1
13. M. A. Gattoo, S. Naseem, M. Y. Arfat, A. M. Dar, K. Qasim, S. Zubair. *Bio. Med Res. Internat.*, 2014, 2014, 498420, 8 pages
14. E. Roduner. *Chem. Soc. Rev.*, 2006, 35, 583.
15. E. Roduner, *Nanoscopic Materials: Size-Dependent Phenomena*, The Royal Society of Chemistry, Cambridge, 2006.
16. J. Jortner, *Z. Phys. D: At., Mol. Clusters*, 1992, 24, 247.

17. S.P. Davtyan, A. Berlin, V. Agabekov, N. Lekishvili. *J. Nanomater.*, 2012 Article ID 215094, 3 pages.
18. S. Srivastava, M Haridas, J. K Basu. *Bull. Mater. Sci.*, 2008, 31, 213.
19. M.S. Dresselhaus, G. Dresselhaus, P.C. Eklund. *Science of Fullerenes and Carbon nanotubes: Their Properties and Applications*, Academic Press, 1996
20. X. Hao. *J. Adv. Dielect.*, 2013, 03, 14 pages
21. A.I. Moreno-Vega, T. Gómez-Quintero, R.E. Nuñez-Anita, L.S. Acosta-Torres, V. Castaño. *J. Nanotechnol.*, 2012, 2012, Article ID 936041, 10 pages
22. S.A. Jamal. *Chem. Sci. J.*, 2013, 1.
23. T. Jamieson, R. Bakhshi, D. Petrova, R. Pocock, M. Imani, A.M. Seifalian. *Biomater.*, 2007, 28, 4717.
24. D. Bera, L. Qian, T.K. Tseng, P.H. Holloway, *Materials*, 2010, 3, 2260.
25. *Nanotechnology and Nanomaterials: Quantum Dots - A Variety of New Applications*, Edited by Ameenah Al-Ahmadi , Publisher: InTech, 2012.
26. S. Mishra, B. Panda, S.S. Rout., *Internat. J. Adv. Engineering Technol.*, 2012, 5,141.
27. L. Cismaru, M. Popa. *ACADEMIA ROMÂNĂ Revue Roumaine de Chimie*, 2010, 55, 433.
28. M. Elsbahy, K.L. Wooley, *Chem. Soc. Rev.*, 2012 , 41, :2545.
29. A. Tavakoli, M. Sohrabi, A. Kargari, *Chem. Papers*, 2007, 61, 151.
30. P. Iqbal, J.A. Preece, P.M. Mendes. *Nanotechnol.*, 2012, DOI: 10.1002/9780470661345.smc195
31. P. Holister, C. Roman, T. Harper. *Bottom up production techniques*, *Technology White Papers* nr. 15, 2003, Cientifica Ltd.
32. G. Cao, *Nanostructures and nanomaterials: synthesis, properties and applications*, World scientific publishing Co. Pt. Ltd., 2004.

33. G. Schmid. Clusters and Colloids : From Theory to Application, Weinheim, VCH., 1994.
34. J. Shan, H. Tenhu, Chem. Commun.,2007, 44, 4580.
35. P.K. Khanna, R. Gokhale, V.V.V.S. Subbarao. J. Mater. Sci., 2004, 39, 3773.
36. N.R. Jana. Small, 2005, 1, 875.
37. H.Yazid, , R. Adnan, , S.A. Hamid, M.A. Farrukh. Turk. J. Chem., 2010, 34, 639.
38. T. Yonezawa, T. Kunitake. Colloid. Surface. A, 1999, 149, 193.
39. B. Derjaguin, L. Landau., Acta. Phys. Chem., 1941, 14, 633.
40. E. Petryayeva, U.J. Krull. Analytica Chimica Acta., 2011, 706, 8
41. E. Hutter, J.H. Fendler. Adv. Mater., 2004,16, 1685.
42. G. Mie. Ann. Phys., 1908, 330, 377.
43. S. Link, M.A. El-Sayed. Annu. Rev. Phys. Chem., 2003, 54, 331.
44. G. C. Papavassiliou. Prog. Solid St. Chem., 1980, 12, 185.
45. M. Kerker. The Scattering of Light and Other Electromagnetic Radiation (New York: Academic Press), 1969
46. C.F. Bohren, D.R. Huffman. Absorption and Scattering of Light by Small Particles (New York: Wiley), 1983
47. K.M. Giannoulis, D.L. Giokas, G.Z. Tsogas, A.G. Vlessidis. Talanta, 2014, 119, 276.
48. A.N. Berlina, A.K. Sharma, A.V. Zherdev, M.S. Gaur, B.B. Dzantiev. Anal. Lett., 2015, 48, 766
49. S. Rastegarzadeh, F. Hashemi. Anal. Methods, 2015, 7, 1478.
50. F. Xia, X. Zuo, R. Yang, Y. Xiao, D. Kang, A. Vallée-Bélisle, X. Gong, J.D. Yuen, B.B.Y. Hsu, A.J. Heeger, K.W. Plaxco. PNAS, 2010, 107, 10837
51. A.R.M. Salcedo, F.B. Sevilla III, Phil. Sci. Lett., 2013, 6, 90.
52. A.J. Haes, R.P Van Duyne. Expert Rev. Mol. Diagn., 2004, 4, 527
53. X. Huang, P.K. Jain, I.H. El-Sayed, M.A. El-Sayed. Nanomedicine, 2007, 2, 681

54. K. Sokolov, M. Follen, J. Aaron, I. Pavlova, A. Malpica, R. Lotan, R.R. Kortum. *Cancer Res.*, 2003, 63, 199.
55. A. Mooradian. *Phs. Rev. Lett.*, 1969, 22, 185.
56. G.T. Boyd, Z.H. Yu, Y.R. Shen. *Phys. Rev. B: Condens. Mater.* 1986, 33, 7923.
57. I.R. Nabiev, H. Morjani, M. Manfait, *Eur. Biophys. J.*, 1991, 19, 311
58. M. Manfait, I. Nabiev, H. Morjani. *J. Cell. Pharm.* 1992, 3, 120.
59. K. Kneipp, A.S. Haka, H. Kneipp, K. Badizadegan, N. Yoshizawa, C. Boone, K.E. Shafer-Peltier, J.T. Motz, R.R. Dasari, M.S. Feld. *Appl. Spectrosc.*, 2002, 56, 150.
60. J.J.Luo, I.M. Daniel. *Compos. Sci. Technol.*, 2003, 63, 1607.
61. C. Park, O. Park, J. Lim, H. Kim. *Polymer*, 2001, 42, 7465.
62. R.E. Gorga, R.E. Cohen. *J. Polym. Sci., Part B: Polym. Phys.*, 2004, 42, 2690.
63. E. Thostenson, C. Li, T. Chou. *J. Compos. Sci. Technol.*, 2005, 65, 491.
64. D. Schmidt, D. Shah, E.P. Giannelis. *Curr. Opin. Solid State Mater. Sci.*, 2002, 6, 205.
65. M. Alexandre, P. Dubois. *Mater. Sci. Eng. Rep.*, 200, 28, 1.
66. S.K. Mazumder, (ed.). *Composites Manufacturing, Materials, Product and Process Engineering*, CRC Taylor & Francis, ISBN 0-8493-0585-3, 2002
67. V. Mittal. *Materials*, 2009, 2, 992.
68. L.L. Beecroft, C.K. Ober. *Chem. Mater.*, 1997, 9, 1302.
69. T. Pereira, Z. Guo, S. Nieh, J. Arias, H.T. Hahn. *J. Compos. Mater.*, 2009, 43, No. 05/2009
70. R. Ramachandran, V. Mani, S.M. Chen, R. Saraswathi, B.S. Lou. *Int. J. Electrochem. Sci.*, 2013, 8, 11680.
71. S. Anandhan, S. Bandyopadhyay. Chapter 1, *Nanocomposites and Polymers with Analytical Methods*, Edited by Dr. John Cuppoletti, 2011.

72. T. Hanemann, J. Böhm, K. Honnef, R. Heldele, B. Schumacher. Properties and application of polymer-ceramic-composites in microsystem technologies. In *Ceramics Processing in Microtechnology*; Ritzhaupt-Kleissl, H.J., Johander, P., Eds.; Whittles Publishing: Dunbeath, Scotland, UK, 2009.
73. S.K. Bhattacharya, R.R. Tummala. *J. Mater. Sci.: Mater. Electron*, 2000, 11, 253.
74. J.P. Dougherty. *Circuits Assembly* 2003, 09, 18.
75. J Njuguna, I. Peña, H. Zhu, S.A. Rocks, M. Blázquez, S.A. Desai, Opportunities and environmental health challenges facing integration of polymer nanoComposites technologies for automotive applications, 2008
76. R.V. Kurahatti, A.O. Surendranathan, S.A. Kori, N. Singh, A.V. Ramesh Kumar, S. Srivastava. *Def. Sci. J.*, 2010, 60, 551.
77. Farhataziz, M.A.J. Rodgers. *Radiation Chemistry*”, VCH Pub. Inc., New York, 1987.
78. A. Mozumder. *Fundamentals of radiation chemistry*, Academic press, San Diego, 1999.
79. J.W.T. Spinks, R.J. Woods. *An introduction to radiation chemistry*, 3rd Ed. Wiley interscience publication, 1990.
80. A.O. Allen. *The radiation chemistry of water and aqueous solutions*, Van Nostrand, New York, 1961.
81. G.V. Buxton. *Radiat. Res. Rev.* 1968, 1, 209.
82. E.J. Hart, M. Anbar. *The hydrated electron*, Wiley Interscience, New York, 1970.
83. R.J. Woods, A.K. Pikaev. *Applied Radiation Chemistry, Radiation Processing*”, New York: John Wiley and Sons, Inc. 113, 1994.
84. J.S. Laughlin, S. Gennes. *Radiation Dosimetry*, 2nd Ed., (Eds. F.H. Attix, W.C. Roesch, T. Tochilin), Academic Press, New York, Vol.2, Chapter 16, 1966.
85. S.R. Domen. *The dosimetry of Ionizing Radiation* (Eds. K.R Kase, B.E. Bjarngard, F. H. Attix,), Academic Press, New York, Vol 2, Chapter 4, 1987.

86. N.W. Holm, R.J. Berry. Manual on Radiatio Dosimetry, Marcel Dekker, New York, 1970.
87. H. Fricke, S. Morse, Am. J. Roentgenol., 1927, 18, 430.
88. H. Fricke, S. Morse. Philos. Mag., 1929, 7, 129.
89. H. Fricke, E.J. Hart. J. Chem. Phys., 1935, 3, 60.
90. W.L. McLaughlin, A. Miller, S. Fidan, K. Pejtersen. Radiat. Phys. Chem., 1977, 29, 119.
91. J.A. Creighton, D.G. Eadon. J. Chem. Soc., Faraday Trans., 1991, 87, 3881.
92. H. Hovel, S. Fritz, A. Hilger, U. Kreibig, M. Vollmer. Phys Rev B, 1993, 48, 18178.
93. S. Underwood, P. Mulvaney. Langmuir, 1994, 10, 3427.
94. U. Kreibig, M. Vollmer. Optical Properties of Metal Clusters, in “Springer Series in Materials Science” (Ed. Paul, M.), Springer-Verlag, Berlin.
95. U. Kreibig, C.V. Fragstein. Z. Phys. A, 1969, 224, 307.
96. S. Link, M.A. El-Sayed. Int. Rev. Phys. Chem. 19, 409. 111. Recent Advances in Polymer Nanocomposites: Synthesis and Characterisation, By S. Thomas, G. Zaikov, V. Meera. 2000.
97. C.E. Corcione, M. Frigione. Materials, 2012, 5, 2960.
98. P. Gill, T. T. Moghadam, B. Ranjbar. J Biomol Tech, 2010, 21, 167.
99. D.B. Williams, C.B. Carter, Transmission Electron Microscopy: A Text Book for Materials Science, 2nd ed Springer; New York, 2009.
100. J.I. Goldstein, D.E. Newbury, D.C. Joy, C.E. Lyman, P. Echlin, E. Lifshin, L.J. Sawyer, J.R. Michael. Scanning Electron Microscopy and X-ray Microanalysis, 3rd Ed., Kluwer Academic Publishers, New York, 2003.
101. R.M. Crooks, M. Zhao, L. Sun, V. Chechik. L.K. Yeung. Acc. Chem. Res., 2001, 34, 181.
102. J. Liu, Y. Lu. J. Am. Chem. Soc., 2003, 125, 6642.

103. K. Kerman, M. Saito, S. Yamamura, Y. Takamura, E. Tamiya. Trends Anal. Chem., 2008, 27, 585.
104. Y. Zhao, Y. Tian, Y. Cui, W. Liu, W. Ma, X. J Am Chem Soc., 2010, 132, 12349.
105. S.D. Brown, P. Nativo, J. Smith, D. Stirling, P.R. Edwards, B. Venugopal, D.J. Flint, J.A. Plumb, D. Graham, N.J. Wheate, J. Am. Chem. Soc., 2010, 132, 4678.
106. J.A. Creighton, D.G. Eadont. J. Chem. Soc. Faraday Trans., 1991, 87, 3881.
107. N. Misra, V. Kumar, L. Borde, L. Varshney. Sens. Actuat. B, 2013, 178, 371.
108. N. Misra, J. Biswal, A. Gupta, J. K. Sainis, S. Sabharwal. Radiat. Phys. Chem., 2012, 81, 195.
109. R. Fenger, E. Fertitta, H. Kirmse, A.F. Thü`nemann, K. Rademann. Phys. Chem. Chem. Phys., 2012, 14, 9343
110. R. Seoudi, D.A. Said. World J. Nanosc. Engin. 2011, 1, 51.
111. B. Hvolbæk, T.V.W. Janssens, B.S. Clausen, H. Falsig, C.H. Christensen, J.K. Nørskov. Nano Today, 2007, 2, 14.
112. S. Choi, S. Lee, Y. Hwang, K. Lee, H. Kang. Rad. Phys. Chem., 2003, 67, 517.
113. S. Choi, H.G. Park. Appl. Surf. Sci., 2005, 243, 76.
114. S.S. Gasaymeh, S. Radiman, L.Y. Heng, E. Saion, G.H.M. Saeed. Am. J. App. Sci. 2010, 7, 892.
115. J. Biswal, N. Misra, L. Borde, S. Sabharwal. Radiat. Phys. Chem., 2013, 83, 67.
116. Y. Li. Food Chem. Toxicol., 1996, 34, 887.
117. E.C. Hurdis, H. Romeyn. Anal. Chem., 1954, 26, 320.
118. V.M. Amin, N.F. Olson. J. Dairy Sci., 1967, 50, 461.
119. N. Maeuchihara, S. Nakano, T. Kawashima. Anal Sci., 2001, 17, 255.
120. M. Onoda, T. Uchiyama, K. Mawatari, K. Kaneko, K. Nakagomi. Anal Sci., 2006, 2815.
121. J. Meyer, U. Karst. Anal. Chim. Acta, 1999, 401, 191.

122. A. Takahashi, K. Hashimoto, S. Kumazawa, T. Nakayama. *Anal. Sci.*, 1999, 15, 481.
123. A. Brestovisky, E. KirowaEisner. *Anal. Chem.*, 1983, 55, 2063.
124. Z.S. Wu, S.B. Zhang, M.M. Guo, C.R. Chen, G.L. Shen, R.Q. Yu. *Anal. Chim. Acta.* 2007, 584, 122.
125. C.J. Yu, W.L. Tseng, *Langmuir*, 2008, 24, 12717.
126. I. Onyido, A.R. Norris, E. Buncel, *Chem. Rev.* 2004, 104, 5911.
127. Y. Guo, Z. Wang, W. Qu, H. Shao, X. Jiang, *Biosens. Bioelectron.*, 2011, 26, 4064.
128. O. Brummer, J.J. La Clair, K.D. Janda, *Bioorg. Med. Chem.*, 2001, 9, 1067
129. O.T. Butler, J.M. Cook, C.F. Harrington, S.J. Hill, J. Rieuwerts, D.L. Miles, *J. Anal. At. Spectrom.*, 2006, 21, 217.
130. Y. Li, C. Chen, B. Li, J. Sun, J. Wang, Y. Gao, Y. Zhao, Z. Chai, *J. Anal. At. Spectrom.* 2006, 21, 94.
131. M. Leermakers, W. Baeyens, P. Quevauviller, M. Horvat, *Trends Anal.Chem.* 2005, 24, 383.
132. X.J. Zhu, S.T. Fu, W.K. Wong, J.P. Guo, W.Y. Wong, *Angew. Chem.* 2006, 118, 3222.
133. X. Guo, X. Qian, L. Jia, *J. Am. Chem. Soc.* 2004, 126, 2272.
134. E. Coronado, J.R. Galan-Mascaros, C. Marti-Gastaldo, E. Palomares, J.R. Durrant, R. Vilar, M. Gratzel, M.K. Nazeeruddin, *J. Am. Chem. Soc.* 2005, 127, 12 351.
135. M.K. Nazeeruddin, D.D. Censo, R. Humphry-Baker, M. Gratzel, *Adv. Funct. Mater.*, 2006, 16, 189.
136. B. Chen, Y. Yu, Z. Zhou, P. Zhong, *Chem. Lett.* 2004, 33, 1608.
137. C. Zhu, L. Li, F. Fang, J. Chen, Y. Wu, *Chem. Lett.*, 2005, 34, 898.
138. M.A. Nolan, S.P. Kounaves, *Anal. Chem.* 1999, 71, 3567.
139. H.J. Kim, D.S. Park, M.H. Hyun, Y.B. Shim. *Electroanal.*, 1998, 10, 303.
140. G. Oster, E.H. Immergut. *J. Am. Chem. Soc.*, 1954, 76, 1393.

141. J. Biswal, S.P. Ramnani, S. Sabharwal. *Int. J. Nanotechnol.*, 2010, 7, 907.
142. S. Pal, G. De. *J Nanosci Nanotechnol.*, 2007, 7, 1994.
143. J. Biswal, S.P. Ramnani, S. Shirolkar, S. Sabharwal. *J. Appl. Pol. Sci.*, 2009, 114, 2348.
144. S. Boopathi, S. Senthilkumar, K. L. Phani. *J. Anal. Methods Chem.*, 2012, 1, Article ID: 348965.
145. A. Guner, A.U. Sevil, O. Guven. *J. Appl. Polym. Sci.*, 1998, 68, 891.
146. J. Belloni, M. Mostafavi, H. Remita, J.L. Marignier, M.O. Delcourt. *New J. Chem.* 1998, 22, 1239.
147. E. Gachard, H. Remita, J. Khatouri, B. Keita, L. Nadjo, J. Belloni. *J. New J. Chem.*, 1998, 22, 1257.
148. A. Imanishi, M. Tamura, S. Kuwabata. *Chem. Commun.* 2009, 1775.
149. A. Imanishi, S. Gonsui, T. Tsuda, S. Kuwabata, K. Fukui. *Phys. Chem. Chem. Phys.* 2011, 13, 14823.
150. Q. Ma, N. Moldovan, D.C. Mancini, R.A. Rosenberg. *Appl. Phys. Lett.*, 2000, 76, 2014.
151. F. Karadas, G. Ertas, E. Ozkaraoglu, S. Suzer, *Langmuir*, 2005, 21, 437.
152. H.J. Lee, J.H. Je, Y. Hwu, W.L. Tsai. *Nucl. Instrum. Meth. B*, 2003, 199, 342.
153. S. Remita, P. Fontaine, E. Lacaze, Y. Borensztein, H. Sellame, R. Farha, C. Rochas, C., M. Goldmann. *Nucl. Instrum. Meth. B.*, 2007, 263, 436.
154. C.H. Wang, C.J. Liu, C.L. Wang, C.C. Chien, Y. Hwu, R.S. Liu, C.S. Yang, J.H. Je, H.M. Lin, G. Margaritondo. *Appl. Phys. A.*, 2009, 97, 295.
155. E. Ozkaraoglu, I. Tunc, S. Suzer. *Polymer*, 2009, 50, 462.
156. H. Liou, W. Liou, H. Lin, Y. Hwu, W. Chen. *Particuology*, 2010, 8, 234.
157. Y.C. Yang, C.H. Wang, Y.K. Hwu, J.H. Je. *Mater. Chem. Phys.* 2006, 100, 72.
158. R.A. Rosenberg, Q. Ma, B. Lai, D.C.J Mancini. *Vac. Sci. Technol. B*, 1998, 16, 3535.
159. S. Schultz, D. Smith, J. Mock, D. Schultz. *Proc. Natl. Acad. Sci. U.S.A.* , 2000, 97, 996.

160. T. Taton, C. Mirkin, R. Letsinger., 2000, 289, 1757.
161. J. Yguerabide, E. Yguerabide. *Anal. Biochem.* 1998, 262, 157.
162. S.S. Gasaymeh, S. Radiman, L.Y. Heng, E. Saion, G.H.M. Saeed. *Afr. Phys. Rev.*, 2010, 4, 31.
163. Y. Borodko, S.E. Habas, M. Koebel, P. Yang, H. Frei, G.A. Somorjai. *J. Phys. Chem. B*, 2006, 110, 23052.
164. H. Wang, X. Qiao, J. Chen, X. Wang, S. Ding. *Mater. Chem. Phys.*, 2005, 94, 449.
165. E. Filippo, A. Serra, D. Manno. *Sensor. Actuat. B-Chem.*, 2009, 138, 625.
166. E. Miller, J. Kędziora. *Int. Rev. Allergol. Clin. Immunol.*, 2011, 17, 20.
167. G. Wurzner, J.C. Gerster, A. Chiolero, M. Maillard, C.L. Fallab-Stubi, H.R. Brunner, M. Burnier. *J. Hypertens.* 2001, 19, 1855.
168. L. Tan, G.M. Yang, P. Wang, Z.Y. Xie, H.P. Bai, X.X. Lu, Y.H. Yang. *Anal. Lett.*, 2008, 41, 2860.
169. R.N. Goyal, V.K. Gupta, A. Sangal, N. Bachheti. *Electroanal.*, 2005, 17, 2217.
170. Y.N. Ni, D.X. Cao, S. Kukt. *Anal. Chim. Acta.*, 2007, 588, 131.
171. H. Dubois, B. Delvoux, V. Ehrhardt, H. Greiling. *J. Clin. Chem Clin. Biochem.*, 1989, 27, 151.
172. T. Yamaguchi, K. Hasegawa, S. Kamino, K. Iyachi, H. Tominaga, Y. Fujita. *Anal. Sci.*, 2007, 23, 223.
173. R.T. Kachoosangi, C.E. Banks, R.G. Compton. *Electroanal.*, 2006, 18, 741.
174. N. Cooper, R. Khosravan, C. Erdmann, J. Fiene, J.W. Lee. *J. Chromatogr. B*, 2006, 837, 1.
175. D. M. Amunson, M. Zhou. *J. Biochem. Biophys. Methods*, 10999, 38, 43.
176. J. Galbán, Y. Andreu, M.J. Almenara, S. de Marcos, J.R. Castillo. *Talanta*, 2001, 54, 847.

177. D. Yao, A.G. Vlessidis, N.P. Evmiridis. *Anal. Chim. Acta.* 2003, 478, 23.
178. T. Pal, D.S. Maity, A. Ganguly. *Talanta*, 1988, 35, 658.
179. Y. Zhao, X. Yang, W. Lu, H. Liao, F. Liao. *Microchim. Acta.*, 2009, 164, 1.
180. G.T. Sanders, A.J. Pasman, F.J. Hoek. *Clin. Chim. Acta.*, 1980, 101, 299.
181. D.W. Moss. *Clin. Chim. Acta.*, 1980, 105, 351.
182. S.M.U. Ali, N.H. Alvi, Z. Ibupoto, O. Nur, M. Willander, B. Danielsson. *Sensor. Actuat. B- Chem.*, 2011, 152, 241.
183. C. Lok, C. Ho, R. Chen, Q. He, W. Yu, H. Sun, P. Tam, J. Chiu, C. Che. *J. Biol. Inorg. Chem.*, 2007, 12, 527.
184. A. Henglein. *Chem. Mater.*, 1998, 10, 444.
185. A. Henglein. *J. Phys. Chem.*, 1993, 97, 5457.
186. X. Li, J.J. Lenhart, H.W. Walker. *Langmuir*, 2010, 26, 16690.
187. P. Vasileva, B. Donkova, I. Karadjova, C. Dushkin. *Colloids Surf. A*, 2011, 382, 203.
188. G.M. Dougherty, K.A. Rose, J.B.H. Tok, S.S. Pannu, F.Y.S. Chuang, M.Y. Sha, G. Chakarova, S.G. Penn. *Electrophoresis*, 2007, 29, 1131.
189. P. Bihari, M. Vippola, S. Schultes, M. Praetner, A.G. Khandoga, C.A. Reichel, C. Coester, T. Tuomi, M. Rehberg, F. Krombach. *Part. Fibre Toxicol.*, 2008, 5, 1.
190. M. Tejamaya, I. Romer, R.C. Merrifield, J.R. Lead. *Environ. Sci. Technol.*, 2012, 46, 7011.
191. A.M.E. Badawy, T.P. Luxton, R.G. Silva, K.G. Scheckel, M.T. Suidan, T.M. Tolaymat, *Environ. Sci. technol.*, 2010, 44, 1260.
192. S. Porel, N. Venkatram, D. Narayana Rao, T.P. Radhakrishnan, J. Nanosci. *Nanotechnol.*, 2007, 7, 1.

193. J. Wang, K.S. Liao, D. Früchtl, Y. Tian, A. Gilchrist, N.J. Alley, E. Andreoli, B. Aitchison, A. G. Nasibulin, H.J. Byrne, E.I. Kauppinen, L. Zhang, W.J. Blau, S.A. Curran. *Mater. Chem. Phys.*, 2012, 133, 992.
194. Y.P. Sun, J.E. Riggs, *Int. Rev. Phys. Chem.*, 1999, 18, 43.
195. Y. Chen, Y. Lin, Y. Liu, J. Doyle, N. He, X.D. Zhuang, J.R. Bai, W.J. Blau. *J. Nanosci. Nanotechnol.*, 2007, 7, 1268.
196. J. Wang, W.J. Blau. *J. Opt. A: Pure and Applied Optics*, 2009, 11, 024001.
197. J. Wang, Y. Chen, W.J. Blau. *J. Mater. Chem.*, 2009, 19, 7425.
198. W. Blau, H. Byrne, W.M. Dennis, J.M. Kelly. *Opt. Commun.*, 1985, 56, 25.
199. C. Flytzanis, F. Hache, M.C. Klein, D. Richard, and P. Roussignol, *Prog. Opt.*, 1991, 29, 321.
200. L. Yang, D.H. Osborne, R.F. Haglund, R.H. Magruder, C.W. White, R.A. Zuhr, H. Hosono, *Appl. Phys. A: Mater. Sci. Process.*, 1996, 62, 403.
201. S.C. Mehendale, S.R. Mishra, K.S. Bindra, M. Laghate, T.S. Dhimi, and K.C. Rustagi. *Opt. Commun.*, 1997, 133, 273.
202. Y. Hamanaka, K. Fukuta, A. Nakamura. *Appl. Phys. Lett.*, 2004, 84, 4938.
203. R.A. Ganeev, A.I. Ryasnyansky, *Appl. Phys. B: Lasers Opt.*, 2006, 84, 295.
204. R. A. Ganeev, M. Suzuki, M. Baba, M. Ichihara, and H. Kuroda, *J. Appl. Phys.* 103, 063102, 2008.
205. H.I. Elim, J. Yang, J. Lee, *Appl. Phys. Lett.*, 2006, 88, 083107.
206. O.M. Folarin, E.R. Sadiku, A. Maity. *Int. J. Phys. Sci.*, 2011, 6, 4869.
207. B. Wang, Q. Tai, S. Nie, K. Zhou, Q. Tang, Y. Hu, L. Song. *Ind. Eng. Chem. Res.*, 2011, 50, 5596.
208. A.K.Sen, B. Mukherjee, A.S. Bhattacharya, L. Sanghi, P.P. De, K. Bhowmick. *J. Appl. Polym. Sci.*, 1991,43,1673.

209. F. Carpentier, S. Bourbigot, M.L. Bras, R. Delobel, M. Foulon. *Polym. Degrad. Stab.*, 2000, 69, 83.
210. H.H. Huang, M. Tian, L. Liu, W.L. Liang, L.Q. Zhang. *J. Appl. Polym. Sci.*, 2006, 100, 4461.
211. L. Zhang, C.Z. Li, Q.L. Zhou, W.J. Shao. *Mater. Sci.*, 2007, 42, 4227.
212. D.Y. Wang, X.X. Cai, M.H. Qu, Y. Liu, J.S. Wang, Y.Z. Wang. *Polym. Degrad. Stab.*, 2008, 93, 2186.
213. B.Li, H.Jia, L.M. Guan, B.C. Bing, J.F.J Dai. *J. Appl. Polym. Sci.*, 2009, 114, 3626.
214. G. Das, N. Karak. *Polym. Degrad. Stab.*, 2009, 94, 1948.
215. L. Wang, M.S. Soto, M.L. MasPOCH. *Mater Design.*, 2013, 52, 609.
216. K. Apaydin, A. Laachachi, V. Ball, M. Jimenez, S. Bourbigot, V. Toniazzo, D. Ruch. *Polym. Degrad. Stab.*, 2013, 98, 627.
217. M. Galimberti, V.R. Cipolletti, M. Coombs. *Dev. Clay Sci.*, 2013, 5, 539.
218. H. Qin, S. Zhang, C. Zhao, G.H.M. Yang. *Polymer*, 2005, 46, 8386.
219. P. Kiliaris, C.D. Papaspyrides. *Prog Polym Sci.*, 2010, 35, 902.
220. Q.Tai, R.K.K. Yuen, L. Song, Y. Hu. *Chem Eng J.* 2012, 183, 542.
221. F. Laoutid, L. Bonnaud, M. Alexandre, J.M. Lopez-Cuesta, P. Dubois. *Mat Sci Eng. R.*, 2009, 63, 100.
222. J.W. Gilman, C.L. Jackson, A.B. Morgan, R. Harris, E. Manias, E.P. Gannelis, M. Wuthenow, D. Hilton, S.H. Phillips. *Chem Mater.*, 2000, 12, 1866.
223. J. Zhu, A.B. Morgan, F.J. Lamelas, C.A. Wilkie. *Chem Mater.*, 2001, 13, 3774.
224. J. Zhu, F.M. Uhl, A.B. Morgan, C.A. Wilkie. *Chem. Mater.*, 2001, 13, 4649.
225. M. Zanetti, T. Kashiwagi, L. Falqui, G. Camino. *Chem Mater.*, 2002, 14, 881.
226. S.S. Ray, M. Okamoto. *Prog Polym Sci.*, 2003, 28, 1539.

227. Y. Kojima, A. Usuki, M. Kawasumi, A. Okada, Y. Fukushima, T. Kurauchi, O.J. Kamigaito. *Mater Res.*, 1993, 8, 1185.
228. L.M. Liu, Z.N. Qi, X.G. Zhu. *J Appl Polym Sci.*, 1999, 71, 1133.
229. S.D. Burnside, E.P. Giannelis. *Chem Mater.* 1995, 7, 1597.
230. M. Zanetti, G. Camino, P. Reichert, R. Mulhaupt. *Macromol Rapid Commun*, 2001, 22, 176.
231. T.C. Canak, I.E. Serhat. *Prog. Org. Coat.*, 2013, 76, 388.
232. X. Wang, W. Xing, L. Song, B.Y.Y. Hu, G.H. Yeoh. *React Funct Polym.* 2013, 73, 854.
233. V. Kumar, Y.K. Bhardwaj, N.K. Goel, S. Francis, K.S.S. Sarma, K.A. Dubey, C.V. Chaudhari, S. Sabharwal. *Surf Coat Tech.*, 2008, 202, 5202.
234. V. Kumar V, Y.K. Bhardwaj, S. Sabharwal. *Prog. Org. Coat.*, 2006, 55, 316.
235. V. Kumar, N. Misra, J. Paul, Y.K. Bhardwaj, N.K. Goel, S. Francis, K.S.S. Sarma, L. Varshney. *Prog. Org. Coat.*, 2013, 76, 1119.
236. Z. Zhang, M. Han. *J. Mater. Chem.*, 2003, 13, 641.
237. S. Porel, S. Singh, S.S. Harcha, D.N. Rao, T.P. Radhakrishnan. *Chem. Mater.*, 2005, 17, 9.
238. V.C. Farmer (Ed.). *The Mineralogical Society Monograph 4*. London. 1974, 331.
239. H. Alamri, I.M. Low. *Polym. Compos.*, 2012, 33, 589.
240. C.E. Corcione, M. Frigione. *Materials*, 2012, 5, 2960.
241. R. Zong, Y. Hu, S. Wang, L. Song. *Polym Degrad Stab.*, 2004, 80, 423.
242. D.W. Van Krevelen. *Polymer*, 1975, 16, 615.
243. J. Feng, J. Hao, J. Du, R. Yang. *Polym Degrad Stab.*, 2010, 95, 2041.
244. J.M. Yeh, C.L. Chen, C.C. Huang, F.C. Chang, S.C. Chen, P.L. Su, C.C. Kuo, J.T. Hsu, B. Chen, Y.H. Yu. *J. Appl. Polym. Sci.*, 2006, 99, 1576.